EXPLORING THE SEASONALITY OF RAPID ARCTIC CHANGES FROM SPACE

MONITORING OF PERMAFROST DISTURBANCE, SNOW COVER AND VEGETATION IN TUNDRA ENVIRONMENTS WITH TERRASAR-X

Samuel Stettner

Univ.-Diss.
zur Erlangung des akademischen Grades
"doctor rerum naturalium"
(Dr. rer. nat.)
in der Wissenschaftsdisziplin „Geomorphologie“

eingereicht in Form einer kumulativen Arbeit an der

Mathematisch-Naturwissenschaftlichen Fakultät

der Universität Potsdam
angefertigt
am Alfred-Wegener Institut

Helmholtz Zentrum für Polar- und Meeresforschung

Published online at the
Institutional Repository of the University of Potsdam:
https://doi.org/10.25932/publishup-42578
https://nbn-resolving.org/urn:nbn:de:kobv:517-opus4-425783

EXPLORING THE SEASONALITY OF RAPID ARCTIC CHANGES FROM SPACE

MONITORING OF PERMAFROST DISTURBANCE, SNOW COVER AND VEGETATION IN TUNDRA ENVIRONMENTS WITH TERRASAR-X

Samuel Stettner

Univ.-Diss.

Zur Erlangung des akademischen Grades

„doctor rerum naturalium“

(Dr.rer.nat.)

In der Wissenschaftsdisziplin „Geomorphologie“

Eingereicht in Form einer kumulativen Arbeit an der

Mathematisch-Naturwissenschaftlichen Fakultät

Der Universität Potsdam

angefertigt

am Alfred Wegener Institut

Helmholtz-Zentrum für Polar- und Meeresforschung

Erstgutachter: Prof. Dr. Hugues Lantuit

Zweitgutachterin: PD Annett Bartsch

Drittgutachter: Prof. Dr. Ralf Ludwig

Ort und Tag der Disputation: Potsdam, 04. Februar 2019

Für meine Familie

ABSTRACT

Arctic warming has implications for the functioning of terrestrial Arctic ecosystems, global climate and socioeconomic systems of northern communities. A research gap exists in high spatial resolution monitoring and understanding of the seasonality of permafrost degradation, spring snowmelt and vegetation phenology. This thesis explores the diversity and utility of dense TerraSAR-X (TSX) X-Band time series for monitoring ice-rich riverbank erosion, snowmelt, and phenology of Arctic vegetation at long-term study sites in the central Lena Delta, Russia and on Qikiqtaruk (Herschel Island), Canada. In the thesis the following three research questions are addressed:

- Is TSX time series capable of monitoring the dynamics of rapid permafrost degradation in ice-rich permafrost on an intra-seasonal scale and can these datasets in combination with climate data identify the climatic drivers of permafrost degradation?
- Can multi-pass and multi-polarized TSX time series adequately monitor seasonal snow cover and snowmelt in small Arctic catchments and how does it perform compared to optical satellite data and field-based measurements?
- Do TSX time series reflect the phenology of Arctic vegetation and how does the recorded signal compare to in-situ greenness data from RGB time-lapse camera data and vegetation height from field surveys?

To answer the research questions three years of TSX backscatter data from 2013 to 2015 for the Lena Delta study site and from 2015 to 2017 for the Qikiqtaruk study site were used in quantitative and qualitative analysis complimentary with optical satellite data and in-situ time-lapse imagery.

The dynamics of intra-seasonal ice-rich riverbank erosion in the central Lena Delta, Russia were quantified using TSX backscatter data at 2.4 m spatial resolution in HH polarization and validated with 0.5 m spatial resolution optical satellite data and field-based time-lapse camera data. Cliff top lines were automatically extracted from TSX intensity images using threshold-based segmentation and vectorization and combined in a geoinformation system with manually digitized cliff top lines from the optical satellite data and rates of erosion extracted from time-lapse cameras. The results suggest that the cliff top eroded at a constant rate throughout the entire erosional season. Linear mixed models confirmed that erosion was coupled with air temperature and precipitation at an annual scale,

seasonal fluctuations did not influence 22-day erosion rates. The results highlight the potential of HH polarized X-Band backscatter data for high temporal resolution monitoring of rapid permafrost degradation.

The distinct signature of wet snow in backscatter intensity images of TSX data was exploited to generate wet snow cover extent (SCE) maps on Qikiqtaruk at high temporal resolution. TSX SCE showed high similarity to Landsat 8-derived SCE when using cross-polarized VH data. Fractional snow cover (FSC) time series were extracted from TSX and optical SCE and compared to FSC estimations from in-situ time-lapse imagery. The TSX products showed strong agreement with the in-situ data and significantly improved the temporal resolution compared to the Landsat 8 time series. The final combined FSC time series revealed two topography-dependent snowmelt patterns that corresponded to in-situ measurements. Additionally TSX was able to detect snow patches longer in the season than Landsat 8, underlining the advantage of TSX for detection of old snow. The TSX-derived snow information provided valuable insights into snowmelt dynamics on Qikiqtaruk previously not available.

The sensitivity of TSX to vegetation structure associated with phenological changes was explored on Qikiqtaruk. Backscatter and coherence time series were compared to greenness data extracted from in-situ digital time-lapse cameras and detailed vegetation parameters on 30 areas of interest. Supporting previous results, vegetation height corresponded to backscatter intensity in co-polarized HH/VV at an incidence angle of 31°. The dry, tall shrub dominated ecological class showed increasing backscatter with increasing greenness when using the cross polarized VH/HH channel at 32° incidence angle. This is likely driven by volume scattering of emerging and expanding leaves. Ecological classes with more prostrate vegetation and higher bare ground contributions showed decreasing backscatter trends over the growing season in the co-polarized VV/HH channels likely a result of surface drying instead of a vegetation structure signal. The results from shrub dominated areas are promising and provide a complementary data source for high temporal monitoring of vegetation phenology.

Overall this thesis demonstrates that dense time series of TSX with optical remote sensing and in-situ time-lapse data are complementary and can be used to monitor rapid and seasonal processes in Arctic landscapes at high spatial and temporal resolution.

ZUSAMMENFASSUNG

Die Erwärmung der Arktis hat Auswirkungen auf die Funktion terrestrischer arktischer Ökosysteme, das globale Klima sowie auf die sozioökonomischen Systeme nördlicher Gemeinden. Es besteht eine Forschungslücke bei der räumlich hoch aufgelösten Überwachung der Saisonalität von Permafrost-degradation, Schneebedeckung und Vegetationsphänologie. Diese Dissertation untersucht die Anwendbarkeit von TerraSAR-X X-Band Daten für die Überwachung eisreicher Ufererosion, Schneeschmelze und Phänologie arktischer Vegetation an Langzeit-Untersuchungsstandorten des zentralen Lena Deltas, Russland und auf Qikiqtaruk (Herschel Island), Kanada. In der Arbeit werden die folgenden drei Forschungsfragen behandelt:

- Sind TSX-Zeitreihen in der Lage, die Dynamik schneller Permafrostdegradation in eisreichem Permafrost auf intra-saisonaler Skala zu überwachen und können diese Datensätze in Kombination mit Klimadaten die klimatischen Treiber dieser Prozesse identifizieren?
- Können TSX-Zeitreihen die Einschränkungen optischer hochaufgelöster Fernerkundung überwinden, um die saisonale Schneedecke und Schneeschmelze in kleinen arktischen Einzugsgebieten adäquat zu überwachen und wie sind die Ergebnisse in Bezug feldbasierten Messungen einzuordnen?
- Können TSX-Zeitreihen die Phänologie arktischer Vegetation abbilden und ist das aufgezeichnete Signal mit in-situ Messungen von Pflanzenvitalität aus Zeitrafferkameradaten und Vegetationshöhen aus Felddaten vergleichbar?

Zur Beantwortung der Forschungsfragen wurden Zeitserien von TSX Rückstreuung aus den Jahren 2013 bis 2015 im Lena-Delta und 2015 bis 2017 auf Qikiqtaruk in quantitativen und qualitativen Analysen komplementär mit hochauflösenden optischen Satellitenbildern und zeitlich hoch aufgelösten Zeitrafferkameradaten genutzt.

Die Dynamik intrasaisonaler Erosion eisreicher Flussufer im zentralen Lena-Delta wurde mit Rückstreuintensitätsbildern von TSX mit 2,4 m räumlicher Auflösung in HH-Polarisation quantifiziert und mit optischen Satelliten-Daten und Feldmessungen mit einer Auflösung von 0,5 m validiert. Kliff Kanten wurden automatisch aus TSX-Intensitätsbildern unter Verwendung einer schwellenwertbasierten Segmentierung und Vektorisierung extrahiert und in einem Geoinformationssystem mit manuell digitalisierten

Zusammenfassung

Kliff Kanten aus optischen Satellitendaten und Erosionsraten, die aus Zeitrafferkameras extrahiert wurden, kombiniert. Die Ergebnisse deuten darauf hin, dass sich die Kliff Kante während der gesamten Auftauzeit mit konstanter Geschwindigkeit zurückzog. Die Verwendung von linearen Mischmodellen bestätigte, dass die Erosion mit der Lufttemperatur und dem Niederschlag gekoppelt war, allerdings nur auf dem jährlichen Maßstab, saisonale Schwankungen beeinflussten die Erosionsrate nicht. Die Ergebnisse zeigen das Potential von HH-polarisierten TSX X-Band Rückstreu Daten zur Überwachung der schnellen Permafrostdegradation mit hoher zeitlicher Auflösung auf.

Die eindeutige Signatur von nassem Schnee in TSX Rückstreuintensitätsbildern wurde genutzt, um Schneeverteilungskarten (SCE) auf Qikiqtaruk in hoher zeitlicher Auflösung zu erzeugen. Aus kreuzpolarisierten VH-TSX Daten abgeleitete SCE zeigten eine große Ähnlichkeit mit aus Landsat 8 abgeleiteten SCE. Zeitreihen von prozentualer Schneebedeckung (FSC) wurden aus TSX und optischen SCE extrahiert und mit FSC-Schätzungen aus in-situ Zeitrafferkamera Daten verglichen. Auch hier zeigte TSX eine starke Übereinstimmung mit den in-situ-Daten und verbesserte die zeitliche Auflösung im Vergleich zur Landsat 8 Zeitreihe erheblich. Aus einer aus allen Datensätzen kombinierten FSC-Zeitreihe konnten zwei Muster von Schneeschmelzen in ausgewählten Einzugsgebieten abgeleitet werden, die sich mit den in-situ Messungen deckten. Zusätzlich konnte TSX später in der Saison Schnee länger erkennen als Landsat 8, was den Vorteil von TSX zur Erkennung von Altschnee unterstreicht. Die TSX-abgeleiteten Schnee-Informationen lieferten wertvolle Einblicke in die Schneeschmelz-Dynamik auf Qikiqtaruk, die zuvor nicht verfügbar war.

Die Empfindlichkeit von TSX für Vegetationsstruktur, die mit phänologischen Veränderungen einhergeht, wurde auf Qikiqtaruk untersucht. Rückstreu- und Kohärenzzeitreihen wurden mit Daten zur Pflanzenvitalität aus in-situ-Zeitrafferkamera Zeitreihen und detaillierten Vegetationsaufnahmen an 30 Standorten verglichen. Die Ergebnisse deckten sich mit vorherigen Ergebnissen anderer Studien und zeigten einen Zusammenhang zwischen Vegetationshöhe und der Rückstreuintensität in gleich polarisierten HH / VV Daten bei einem Einfallswinkel von 31 °. Ferner zeigte die ökologische Klasse mit einer Kombination von hohen Sträuchern und trockenen Oberflächenbedingungen eine zunehmende Rückstreuung mit zunehmende Pflanzenvitalität, wenn der kreuzpolarisierte VH / HH-Kanal bei 32 ° Einfallswinkel verwendet wurde. Dies könnte durch Volumenstreuung von Blattaustrieb und

Blattentfaltung verursacht werden. Ökologische Klassen mit flach wachsender Vegetation und höheren Anteilen von offenem Boden zeigten abnehmende Rückstreutrends über die Vegetationsperiode in den gleich polarisierten VV / HH-Kanälen. Dies ist vermutlich eher auf abnehmende Oberflächenfeuchte zurückzuführen anstatt auf ein verändertes Vegetationsstruktursignal. Die Ergebnisse aus strauchdominierten Klassen sind vielversprechend und liefern eine ergänzende Datenquelle für zeitlich hochaufgelöste Beobachtung der Vegetationsphänologie.

Insgesamt zeigt diese Arbeit, dass die komplementäre Verwendung von dichten Zeitreihen von TSX mit optischer Fernerkundung und in-situ-Zeitrafferdaten verwendet werden können, um schnelle und saisonale Prozesse in arktischen Landschaften mit hoher räumlicher und zeitlicher Auflösung zu überwachen. Die trägt dazu bei, das Verständnis für eine Vielzahl von Komponenten in sich schnell verändernden arktischen Umgebungen zu verbessern.

TABLE OF CONTENTS

Abstract ..... **I**

Zusammenfassung ..... **III**

Table of contents ..... **VI**

List of figures ..... **IX**

List of tables ..... **XI**

List of abbreviations ..... **XII**

1 Introduction **1**

1.1 Scientific background and motivation 1

1.1.1 Permafrost degradation 1

1.1.2 Snow cover 3

1.1.3 Vegetation phenology 5

1.2 Remote sensing of rapid changes 5

1.2.1 SAR remote sensing 6

1.2.2 TerraSar-X 9

1.3 Data and methods 10

1.4 Aims and objectives 13

1.5 Study areas and data 15

1.6 Thesis structure and author contributions 17

1.6.1 Chapter 2 - Monitoring inter- and intra-seasonal dynamics of rapidly degrading ice-rich permafrost riverbanks in the Lena Delta with TerraSAR-X time series 17

1.6.2 Chapter 3 – TerraSAR-X time series fill a gap in spaceborne snowmelt monitoring of small Arctic catchments 17

1.6.3 Chapter 4 – Estimation of Arctic tundra vegetation phenology with TerraSAR-X 18

2 Monitoring inter- and intra-seasonal dynamics of rapidly degrading ice-rich permafrost riverbanks in the Lena Delta with TerraSAR-X time series 19

2.1 Abstract 19

2.2 Introduction 20

2.3 Study area 22

2.4 Data and methods 24

2.4.1 SAR data and processing 24

2.4.2 Automated cliff-top line extraction from SAR data 27

2.4.3 Quantification of cliff-top erosion with the Digital Shoreline Analysis System 28

2.4.4 Cliff top mapping from optical satellite data 29

2.4.5 In-situ observations of cliff top erosion 30
2.4.6 Climate data 31
2.4.7 Statistical data analysis 32
2.5 Results 33
2.5.1 TSX erosion versus in-situ and optical datasets 33
2.5.2 Inter- and intra-annual cliff-top erosion and climate data 35
2.5.3 Backscatter time series 38
2.6 Discussion 40
2.6.1 Inter-annual dynamics of cliff-top erosion 40
2.6.2 Intra-annual dynamics of cliff-top erosion 41
2.6.3 Backscatter dynamics of tundra and cliff surfaces 41
2.7 Conclusions 43
2.8 Acknowledgments 44

3 TerraSAR-X time series fill a gap in spaceborne snowmelt monitoring of small Arctic catchments 45

3.1 Abstract 45
3.2 Introduction 45
3.3 Study area 50
3.4 Data and methods 52
3.4.1 SAR satellite data 52
3.4.2 Optical satellite data 53
3.4.3 In-situ time-lapse camera data 53
3.4.4 Snow Cover Extent from TerraSAR-X 54
3.4.5 Snow Cover Extent from Landsat 8 56
3.4.6 Accuracy assessment of TerraSAR-X Snow Cover Extent 56
3.4.7 Fractional Snow Cover time series analysis 56
3.5 Results 57
3.5.1 Evaluation of TSX Snow Cover Extent 57
3.5.2 Time series of Fractional Snow Cover in all catchments 62
3.5.3 Time series of Fractional Snow Cover in small catchments 63
3.6 Discussion 67
3.6.1 Spatiotemporal monitoring of snowmelt dynamics using TSX 67
3.6.2 Technical considerations for using TSX for wet snow detection 68
3.7 Conclusions 70
3.8 Acknowledgements 71
3.9 Appendix 72

Table of contents

4 Relationships between X-Band SAR and vegetation phenology in a low Arctic ecosystem 77

4.1 Abstract 77

4.2 Introduction 78

4.3 Study area 80

4.4 Data and methods 84

4.4.1 In-situ time-lapse phenological cameras 84

4.4.2 Time-lapse image analysis 84

4.4.3 SAR satellite data 85

4.4.4 Backscatter and coherence time series 85

4.4.5 In-situ vegetation and climate data 86

4.5 Results 87

4.5.1 Phenocams 87

4.5.2 Backscatter dynamics 88

4.5.3 Coherence dynamics 93

4.6 Climate data 97

4.7 Backscatter and vegetation height 98

4.8 Discussion 98

4.9 Conclusion 101

4.10 Acknowledgments 101

5 Synthesis 103

5.1 Rapid permafrost disturbance 104

5.2 Snowmelt dynamics 105

5.3 Arctic tundra vegetation phenology 106

5.4 Seasonality and complementarity of TSX 107

5.5 Limitations and technical considerations 108

5.6 Key findings and outlook 110

References 111

Acknowledgements 129

Eidesstattliche Erklärung 131

LIST OF FIGURES

Figure 1-1: Anomalies of surface temperatures 1
Figure 1-2: Rapid permafrost degradation in the Lena Delta and along the Yukon Coast, Canada. 2
Figure 1-3: Evolution of snowmelt on Qikiqtaruk (Herschel Island) 4
Figure 1-4: Principles of TSX SAR imaging 8
Figure 1-5: Scattering mechanism in SAR imaging 8
Figure 1-6: Schematic of the research focus 13
Figure 1-7: Location of the Lena Delta and Qikiqtaruk (Herschel Island) 15
Figure 2-1: Regional overview of the Lena Delta study site. 24
Figure 2-2: Selected spatial subsets of TSX X-Band backscatter intensity images 26
Figure 2-3: Schematic of automated cliff-top line extraction from TerraSAR-X (TSX) data. 28
Figure 2-4: Optical satellite data and digitized cliff-top lines. 30
Figure 2-5: In-situ monitoring of cliff-top erosion on Kurungnakh Island. 31
Figure 2-6: Selected climate parameters during the observation period. 32
Figure 2-7: Spatial subset of TerraSAR-X cliff-top lines. 34
Figure 2-8: Comparison of annual optical and TerraSAR-X measurements of Cliff-top erosion. 35
Figure 2-9: Intra-seasonal median cliff-top erosion (CTE) from TerraSAR-X (TSX) 38
Figure 2-10: Median sigma nought backscatter of TSX acquisitions. 39
Figure 3-1: Location of Qikiqtaruk in the Southwestern Beaufort Sea 50
Figure 3-2: Data processing schematic for the optical Landsat 8 and TSX data. 52
Figure 3-3: Comparison of filter methods for SCE generation. 55
Figure 3-4: Comparison of Landsat 8 SCE (left panels) and corresponding TSX SCE derived from the VH (middle panels) and VV (right panels) polarized channels of orbit 61 60
Figure 3-5: Comparison of Landsat 8 SCE (left panels) and corresponding TSX SCE derived from the VH (middle panels) and VV (right panels) polarized channels of orbit 115 61
Figure 3-6: Time series of fractional snow cover (FSC) extent and air temperature of Qikiqtaruk 63
Figure 3-7: Top graph: Fractional snow cover from time lapse (in-situ), Landsat 8 and TerraSAR-X (TSX) imagery in 2016 64
Figure 3-8: Top graph: Fractional snow cover from time lapse (in-situ), Landsat 8 (L8) and TerraSAR-X (TSX) imagery in 2017 66
Figure 3-9: SCE from TerraSAR-X VH from the 29th of April 2016 (left) and from the 9th of May 2016 (right) for the Ice Creek catchment and surroundings. 68
Figure 3-10: Comparison of Landsat 8 SCE and corresponding TSX SCE derived from the HH and VV polarized channels of orbit 24 72
Figure 3-11: Comparison of Landsat 8 SCE and corresponding TSX SCE derived from the HH and VV polarized channels of orbit 137. 73

List of figures

Figure 3-12: Comparison of Landsat 8 SCE (left panels) and corresponding TSX SCE derived from the HH (centre panels) and VV (left panels) polarized channels of orbit 152 74
Figure 4-1: Overview of the Qikiqtaruk study site. 81
Figure 4-2: Greenness Excess Index (GEI) from the phenological cameras. 88
Figure 4-3: Backscatter intensity time series at the regional scale by TSX orbit and polarization. ... 89
Figure 4-4: Backscatter intensity of ecological classes in the growing season of 2015 to 2017 as observed by TSX orbit 152 (HH/VV). 90
Figure 4-5: Backscatter intensity of ecological classes in the green-up season of 2015 to 2017 as observed by TSX orbit 24 (HH/VV) 91
Figure 4-6: Backscatter intensity of ecological classes in the green-up season of 2015 to 2017 as observed by TSX orbit 61 (VH/VV). 92
Figure 4-7: Coherence time series at the regional scale by TSX orbit and polarization. 93
Figure 4-8: Coherence time series of ecological classes in the green-up season of 2015 to 2017 as observed by TSX orbit 152 (HH/VV). 94
Figure 4-9: Coherence time series of ecological classes in the green-up season of 2015 to 2017 as observed by TSX orbit 24 (HH/VV). 95
Figure 4-10: coherence time series of ecological classes in the green-up season of 2015 to 2017 as observed by TSX orbit 61 (VH/VV). 96
Figure 4-11: Mean daily temperature (Mean Temp ° C) in 2015, 2016 and 2017 and total daily precipitation (Total Precip mm) in 2016 and 2017. 97
Figure 4-12: Backscatter intensity by mean canopy height class by TSX orbit and polarization..... 98
Figure 5-1: Schematic of Arctic seasonality illustrating selected ecosystem components and monitoring instruments 108

LIST OF TABLES

Table 1-1: Common frequency bands used in microwave remote sensing.....7
Table 1-2: Overview of datasets, methods as well as developed data products and data sources.....12
Table 2-1: Comparison of in situ and TerraSAR-X derived cliff-top erosion (CTE).....34
Table 2-2: Comparison of optical and TSX-based cliff-top erosion (CTE) measurements.....35
Table 2-3: Annual characteristics of erosion and climate at the study site.....37
Table 2-4: Results of the linear mixed models.....38
Table 2-5: Mean backscatter over Areas of interest (AOI) by year.....39
Table 3-1: Information on TSX orbits.....53
Table 3-2: Confusion matrix results from the comparison of TerraSAR-X and Landsat 8 derived.....58
Table 3-3: List of TSX scenes used for the averaged dry snow reference.....74
Table 3-4: Fractional snow cover from visual estimations of in-situ time lapse imagery.....75
Table 4-1: Overview of selected ecological units on Qikiqtaruk.....83
Table 4-2: Overview on TSX orbits.....85

LIST OF ABBREVIATIONS

Abbreviation	Meaning
DLR	German Aerospace Agency
AIC	Akaike Information Criteria
ALOS PRISM	Advanced Land Observing Satellite Panchromatic Remote-sensing Instrument for Stereo Mapping
ANOVA	analysis of variance
AOI	Area of Interest
AVHRR	Advanced Very High Resolution Radiometer
AZ	Azimuth
BIC	Bayesian Information Criterion
CA	Canada
CTE	Cliff-top erosion
dB	Decibel
DEM	Digital elevation model
DLR	German Aerospace Centre
DSAS	Digital Shoreline Analysis System
AVHRR	Advanced High Resolution Radiometer
ALOS-2	Advanced Land Observing Satellite
GHz	Gigahertz
InSAR	SAR interferometry
ETM	Enhanced Thematic Mapper
FSC	Fractional snow cover
HH	Polarization Channel Horizontal-Horizontal
HST	Honest Significance Differences
HV	Polarization Channel Horizontal-Vertical
L1TP	Standard Terrain Correction processing Level of the Landsat program
MD	Mid-date
MODIS	Moderate Resolution Imaging Spectroradiometer
NDSI	Normalized Difference Snow Index
OLI	Operational Land Imager
P	Precipitation
PC	Phenological Cameras
PSTG	Polar Space Task Group
RA	Range
RGB	Red-Green-Blue
RS	RADARSAT
RU	Russia
SAR	Synthetic Aperture Radar
SCE	Snow cover extent
SNAP	Sentinel Application Platform
SSC	Single-Look Slant Range Complex

Table continues on next page

List of abbreviations

Abbreviation	Meaning
SWE	Snow water equivalent
SWIN	Incoming Shortwave Infrared
TDD	Thawing Degree Days
TDX	Tandem-X satellite Mission
TDX-IDEM	Intermediate DEM from Tandem-X satellite mission
TID	Transect ID
TSX	TerraSAR-X
USGS	United States Geological Survey
UTC	Universal Transversal Time
UTM	Universal Transverse Mercator
VH	Polarization Channel Vertical-Horizontal
VV	Polarization Channel Vertical-Vertical
WGS	World Geodetic System
WMO	World Meteorological Organization

Chapter 1

1 INTRODUCTION

1.1 SCIENTIFIC BACKGROUND AND MOTIVATION

The anthropogenic impact on Earth's climate has led to an increase in mean global air temperatures since the beginning of the industrial age (IPCC, 2014b). The Arctic biome, roughly encompassing areas north of 60° N, is experiencing an increase of mean annual air temperature twice the global average with the strongest warming trends attributed to warming winter temperatures (Figure 1-1). This warming puts pressure on the temperature sensitive cryosphere which includes areas of snow, freshwater ice, sea ice, glaciers, ice caps, ice sheets, and permafrost. A disruption of the cold mean state of the cryosphere impacts the stability and functioning of terrestrial Arctic ecosystems with implications for global climate and associated feedbacks as well as socioeconomic systems of northern communities (AMAP, 2018).

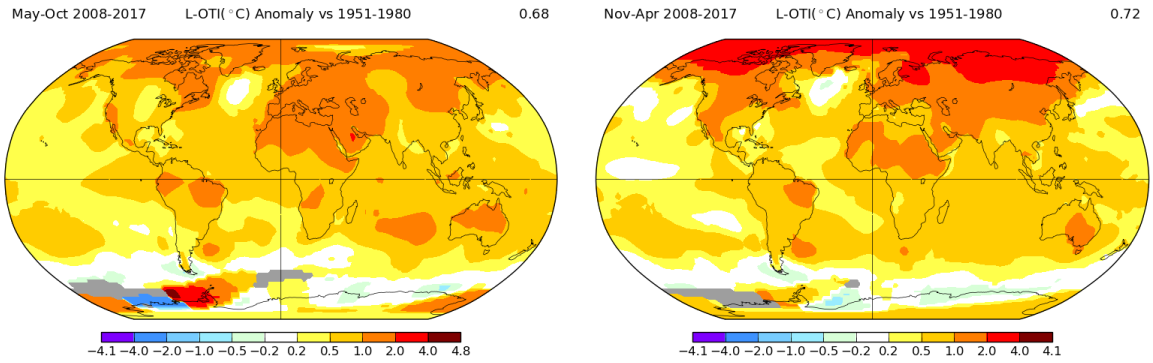

Figure 1-1: Anomalies of surface temperatures between 2008 to 2017 compared to 1951 to 1980 for the warm season (left) and the cold season(right). (GISTEMP Team, 2018; Hansen et al., 2010)

1.1.1 PERMAFROST DEGRADATION

Permafrost is ubiquitous in terrestrial Arctic ecosystems. It is defined as ground that remains below 0°C for at least two consecutive years (van Everdingen, 2005). Long-term borehole measurements show that permafrost temperatures in the Arctic have increased in the last decades and this change in thermal equilibrium is leading to permafrost degradation (Kokelj and Burn, 2005; Romanovsky et al., 2010; Vaughan et al., 2013) (Figure 1-2).

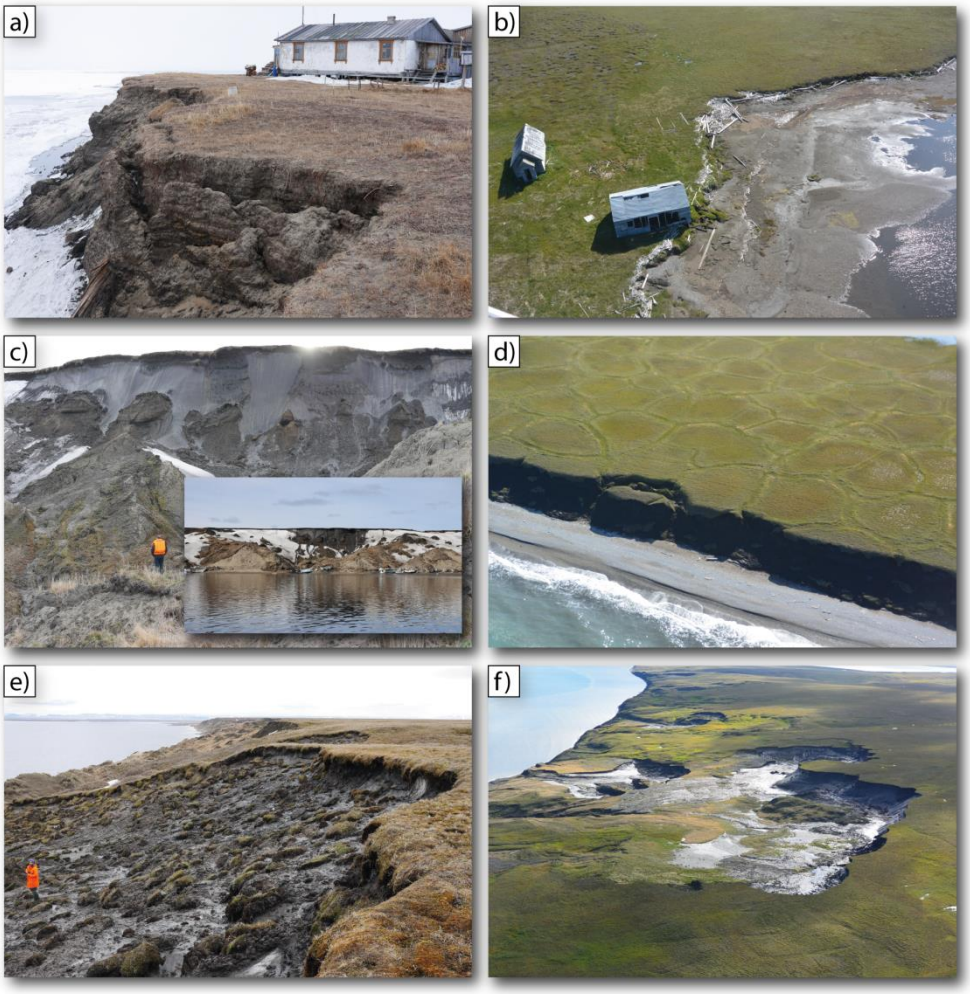

Figure 1-2: Rapid permafrost degradation in the Lena Delta, Russia, and along the Yukon Coast, Canada. The photographs show a) Riverbank erosion in the Lena Delta threatens research infrastructure at the research station Samoylov, June 2015 b) Coastal erosion endangeres an historically important site at the Yukon Coast in August 2015 (Photo: Anna Irrgang); c) Massive ice wedge exposure at a permafrost riverbank of Kurungnakh Island in the central Lena Delta, June 2015 with inset showing the same location with compacted snow deposits the same day; d) Coastal erosion of polygonal tundra at Komakuk Beach along the Yukon Coast in August 2015 (Photo: George Tanski); e) Permafrost thaw and cliff top erosion at a permafrost riverbank of Kurungnakh Island in the central Lena Delta; f) Thawing of massive ground ice leads to retrogressive thaw slumps and sediment plumes in the ocean on Qikiqtaruk (Herschel Island) along the Yukon Coast.

Thermokarst and thermal erosion are the main driving processes of permafrost degradation causing rapid changes of Arctic landscapes (van Everdingen, 2005). Thermokarst is a process by which characteristic landforms result from thawing of ice-rich permafrost or melting of massive ice (van Everdingen, 2005). Climate change, disturbance of vegetation cover, fire, changes in drainage channels and human activities can initiate thermokarst activity (French, 2007; Washburn, 1979). Thermal erosion is the erosion of

ice-bearing permafrost by the combined thermal and mechanical action of moving water (van Everdingen, 2005). Thermo-erosional processes play a major role in the erosion of ice-bearing coastlines (Günther et al., 2013; Lantuit and Pollard, 2008), lake shores with significant wave activity (Jones et al., 2011; Morgenstern et al., 2011a), valleys and hydrological flow networks (Godin et al., 2014; Morgenstern, 2012) as well as riverbanks (Costard et al., 2007; Dupeyrat et al., 2011; Kanevskiy et al., 2016). Rates of thermal erosion can exceed those of thermokarst by two orders of magnitude, making it the most effective process of permafrost degradation (Kanevskiy et al., 2016). Permafrost coastal zones are expected to experience increased permafrost degradation because of ongoing sea ice reduction (Lawrence et al., 2008). The degradation of permafrost is both a social and environmental hazard threatening local infrastructure and facilitating the release of ancient carbon (Grosse et al., 2011; Kääb, 2008).

1.1.2 Snow cover

Snow is a crucial parameter in Arctic ecosystems underlain by permafrost as it controls the exchange of heat between the atmosphere and the frozen ground surface. The duration, timing and extent of snow cover determines if permafrost is insulated from cold winter or warm spring air temperatures (Ling and Zhang, 2003; Zhang et al., 1996; Zhang and Stamnes, 1998). Deeper and prolonged winter snow packs can lead to temperature increases in permafrost and over time increase the active layer thickness (Johansson et al., 2013). This in turn can lead to changes in soil nutrient availability and shifts in the composition of vegetation communities (Johansson et al., 2013; Krab et al., 2017; Schimel et al., 2004; Semenchuk et al., 2015). In addition, late-lying and perennial snow patches create unique ecological conditions as a result of thermal regulation and soil moisture content and play an important role in the biodiversity of Arctic tundra vegetation (Ballantyne, 1978).

Snowmelt initiates the hydrological year, marks an increase in soil biogeochemical activity and dictates the onset of vegetation phenology (Johansson et al., 2013; Krab et al., 2017; Schimel et al., 2004; Semenchuk et al., 2015). Hydrologically, snowmelt is often the most important input in small Arctic catchments producing a large percentage of annual discharge (Pohl and Marsh, 2006). Unlike in temperate biomes where spring temperatures determine the onset of phenology, Arctic vegetation phenology begins when areas are snow free or even partially snow free (Billings and Bliss, 1959; Bjorkman et al., 2015a) (Figure 1-3).

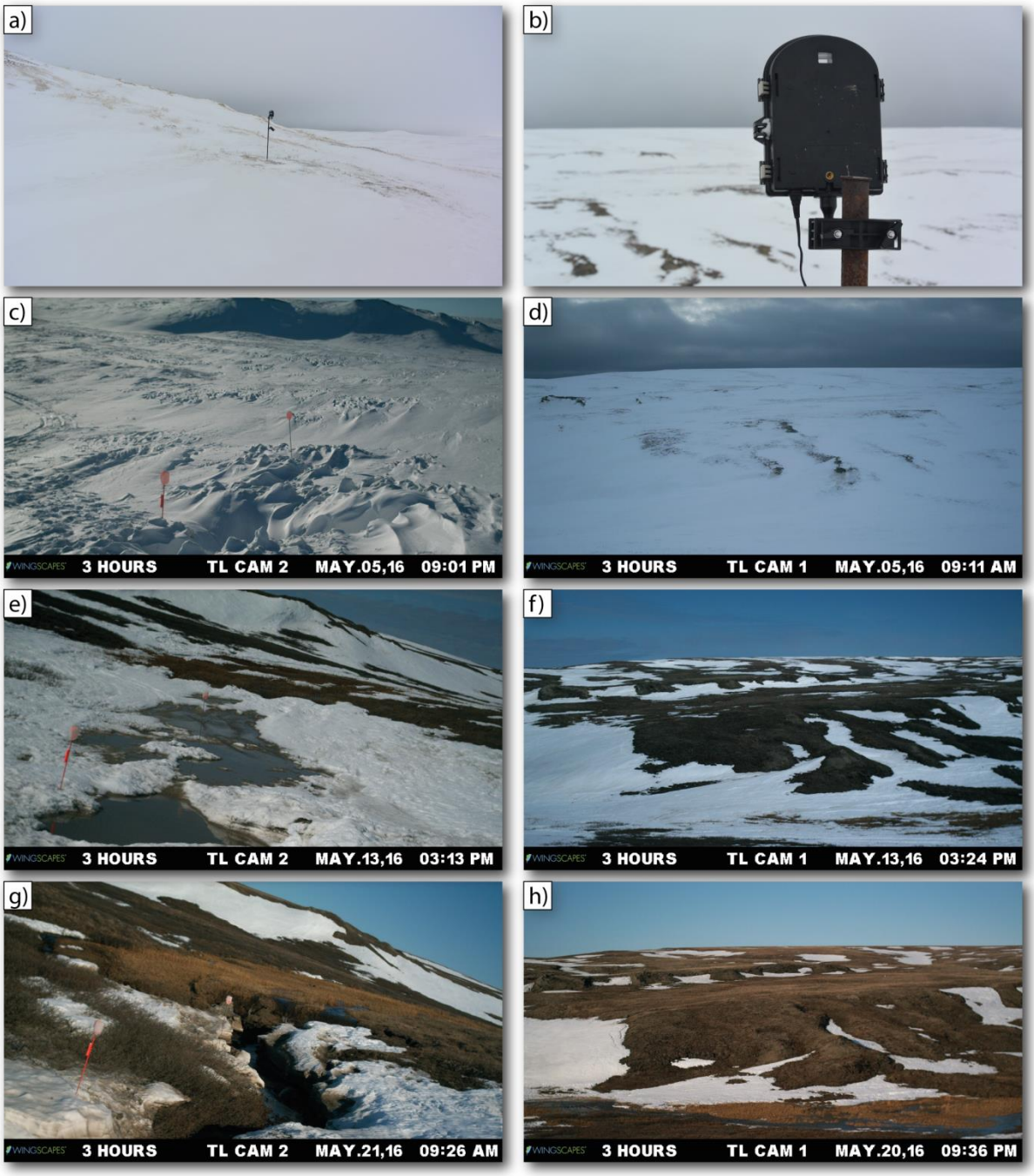

Figure 1-3: Evolution of snowmelt on Qikiqtaruk (Herschel Island) as observed from time-lapse imagery. The photos show a) Position of camera TL CAM 2 on 5th May 2016; b) Position of cameras TL CAM 1 on 2nd of May 2016; c) and d) full snow cover before snowmelt on 5th of May; e) and f) peak snow melt with high discharge and standing water in e) and already snow free upland areas in f) At this point of snowmelt vegetation will start to emerge; g) and h) late phase of snow melt with compacted snow banks in protected and incised areas of the slopes.

Spring snow cover in Arctic environments has undergone a rapid decrease in past decades concurrent with increasing air temperatures and declining sea ice (Brown and Robinson, 2011). However, changes in winter precipitation and resulting snow cover depth extent is

predicted to be highly variable over space and time resulting in high uncertainties in future spring snowmelt dynamics (Weller et al., 2005).

1.1.3 VEGETATION PHENOLOGY

Vegetation phenology can be used as an indicator of productivity, reproduction and overall fitness (Iler et al., 2013; Wheeler et al., 2015). Arctic vegetation phenology is a sensitive indicator of climate change as it is dictated by climatic conditions, particularly snow cover and snowmelt dynamics. This makes it a valuable parameter in the study of Arctic change. For example, more than thirty percent of the Arctic landmass showed a greening trend between 1982 and 2012 with the strongest signal observed in the North American High Arctic suggesting increased vegetation productivity (IPCC, 2014a). More recently, this greening trend has shown a decrease in some areas linked to large scale climate circulation illustrating the sensitivity of vegetation to climate changes and associated feedbacks (Bhatt et al., 2013). In addition, shifting winter precipitation coupled with observed decreases in spring snow cover in the past decades has had direct impacts on the phenology of Arctic vegetation (Bjorkman et al., 2015b). An earlier start of the growing season has been detected over North America in the past decade (Zeng et al., 2011). This advanced spring phenology due to decreased spring snow cover can lead to a de-synchronization of vegetation-climate interactions resulting in the vulnerability of species to damage from frost and soil saturation (Cook et al., 2012; Høye et al., 2013; Inouye and McGuire, 1991; Wheeler et al., 2015; Yu et al., 2010).

1.2 REMOTE SENSING OF RAPID CHANGES

Many different remote sensing systems have been used to study and monitor the cryosphere and resulting land cover changes in Arctic regions (Kääb, 2008; Stow et al., 2004). Operational satellite products are available at spatial scales and resolutions that provide the potential to monitor rapid changes in permafrost, snow cover and vegetation phenology of terrestrial Arctic ecosystems (Stow et al., 2004). Remote sensing of terrestrial Arctic ecosystems is dominated by the use of freely available data archives from optical sensors such as Landsat (30 m), Sentinel-2 (10-20 m), and the Moderate Resolution Imaging Spectroradiometer (MODIS) (250–500 m). However, optical satellite sensors are often affected by complete or fragmented cloud cover which introduces gaps or errors into the data. This spatiotemporal limitations of optical time series present challenges for

analysis and mapping of rapid and spatially variable phenomena with strong seasonality like permafrost disturbance, snowmelt, and vegetation phenology.

Many previous remote sensing studies of rapid permafrost degradation have focused on the annual or decadal erosion of ice-rich permafrost bluffs at Arctic coastlines, lakes and riverbanks (Günther et al., 2013; Jones et al., 2011; Kanevskiy et al., 2016; Lantuit et al., 2011). To date, few intra-annual studies on permafrost degradation exist at landscape scales. Attempts to monitor permafrost degradation at a regional scale have been established through inventories and databases of thermokarst landforms and coastal erosion using optical satellite imagery and DEMs (Grosse et al., 2006; Lantuit et al., 2012a; Nitze and Grosse, 2016).

Snow cover extent can be analysed at intra-annual scales using MODIS which delivers a daily snow cover product at spatial resolutions of 250 or 500 m (Hall et al., 2002). While the daily MODIS product is highly valuable for regional scale studies, monitoring local scale heterogeneity, which is of particular importance in Arctic ecosystems, is not possible. Data from the Landsat archive has been used to monitor impacts of snow cover on watershed hydrology dynamics at landscape scales in permafrost environments (Pohl and Marsh, 2006; Woo and Marsh, 2005). However, the aforementioned challenges of persistent cloud cover limit the availability of high quality time series data.

Long-term monitoring of the response of vegetation to climate change has been widely studied using time series of high temporal resolution optical sensors such as MODIS or the Advanced High Resolution Radiometer (AVHRR) (Zeng et al., 2011). Decadal trends of greening and browning from the Landsat archive over Alaskan tundra have recently been shown to be the result of connections between local permafrost-driven landscape heterogeneity and regional climate change (Lara et al., 2018). As with snow cover, these records are a valuable indication of regional scale changes but cannot resolve the small-scale heterogeneity of Arctic vegetation change (Elmendorf et al., 2012).

1.2.1 SAR REMOTE SENSING

A new generation of active microwave satellite missions that use synthetic aperture radars (SAR) in high spatial resolution can address some of the limitations associated with optical remote sensing (Moreira et al., 2013). SAR satellite systems are independent of atmospheric distortions from water vapour and clouds as well as solar illumination allowing data acquisition under all conditions and the creation of dense time series. Newly

operational high spatial resolution SAR satellites include the European Space Agency's Sentinel-1, Japan Aerospace Exploration Agency's Advanced Land Observing Satellite (ALOS-2), and the German Aerospace Center's TerraSAR-X (TSX) as well as the Canadian RADARSAT-2.

The frequency and corresponding wavelengths of SAR systems range from 0.3 GHz to 300 GHz and 1 m to 1 mm, respectively. The most commonly used frequency bands in SAR remote sensing are Ku, X, C and L-Band (Table 1-1). Longer wavelength penetrate can penetrate deeper into the target while shorter wavelengths can provide information on small above ground targets. The portion of transmitted energy that is received by antennas is referred to as backscatter. Information stored in a SAR image is complex and contains data on the amplitude and phase of the microwave signal. The amplitude is defined as the intensity of the backscatter and is affected by two main components of the target, surface roughness and the dielectric properties.

Table 1-1: Common frequency bands used in microwave remote sensing with corresponding frequency and wavelength ranges.

Frequency Band	Ku	X	C	L
Frequency [GHz]	17.6-12	12-7.5	7.5-3.75	2-1
Wavelength [cm]	1.7-2.5	2.5-4	4-8	15-30

Microwave remote sensing is divided into passive and active microwave systems. Passive sensors detect the natural microwave emissions of the Earth's surface while active sensors transmit pulses of energy and receive the echo after it has been attenuated through the atmosphere, interacted with the target and travelled back to the antenna. Passive microwave systems operate at high temporal (daily coverage) and coarse spatial (km) resolutions, making it less suitable for applications of fine-scale processes. The spatial resolution of active systems depends on the size of the transmitting and receiving antenna. SAR are side looking active microwave systems where the motion in azimuth direction of the antenna during time between transmitting and receiving is used to synthetically enlarge the antenna as illustrated in Figure 1-4**Fehler! Verweisquelle konnte nicht gefunden werden.**.

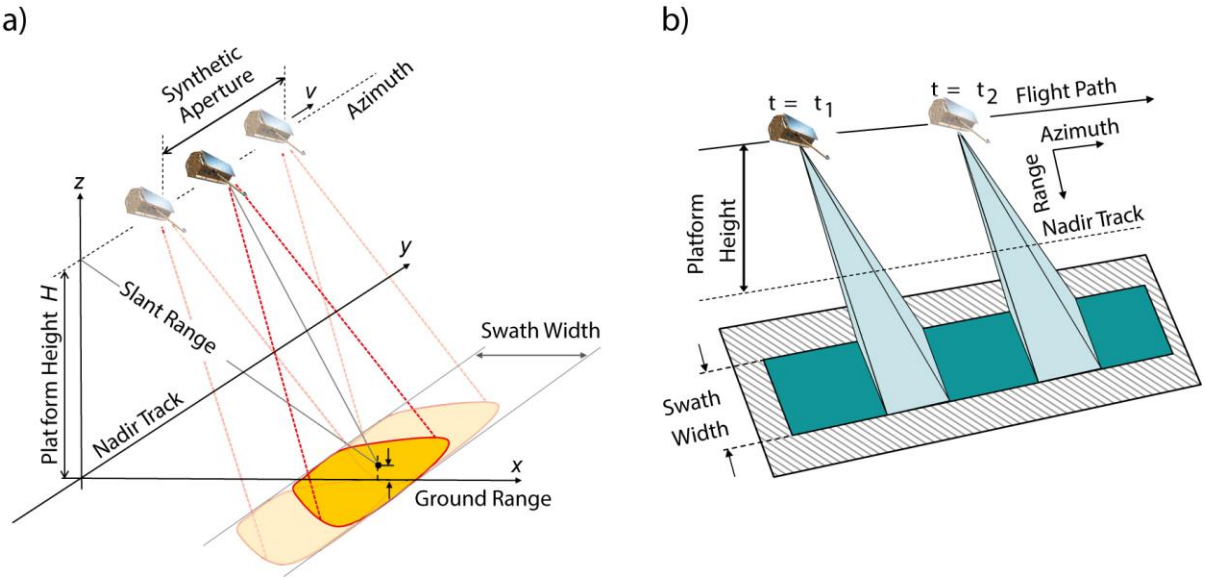

Figure 1-4: Principles of TSX SAR imaging adapted from Moreira et al. (2013) . Panel a) shows the SAR imaging geometry, panel b) shows the StripMap imaging mode of TSX.

Surface roughness determines the scattering mechanism as shown in Figure 1-5. A rougher surface will result in higher backscatter intensity due to diffuse scattering. A smooth surface will reflect more energy away from the sensor and result in a low backscatter as result of specular scattering, for example on calm water. In the case of right angles on the surface a high portion of the signal will be reflected back to the antenna and result in a high backscatter intensity, for instance in residential areas. This is also referred to as double bounce (Figure 1-5). The dielectric properties of a targeted object strongly depend on its water content. High water content results in less penetration of the signal and high reflectivity, leading to high backscatter intensity. Variations in surface wetness as well as the thermal state (frozen or non-frozen) of the ground greatly affect the microwave signal.

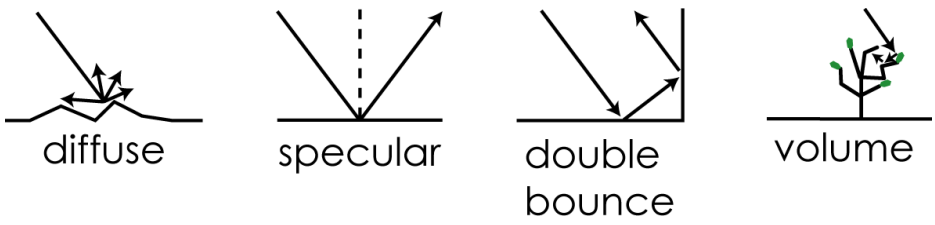

Figure 1-5: Scattering mechanism in SAR imaging

Snow, ice and vegetation are media with discrete and randomly distributed scattering elements within a volume. The signal scatters within and between these elements resulting in complex interactions referred to as volume scattering. The size of the

scattering elements determines if the signal is attenuated or amplified, which results in lower or higher backscatter intensity, respectively.

On surfaces with vegetation cover, L-Band SAR systems using longer wavelengths can penetrate through the vegetation canopy and the backscattered signal has a higher contribution from the underlying ground, known as surface scattering (Ulaby et al., 1986). Shorter wavelength X-Band systems have a higher contribution from the vegetation layer and are therefore more sensitive to changes in canopy cover or volume scattering (Fontanelli et al., 2013). In general the scattering mechanisms of a vegetated surface can be complex due to different contributions of the surface and corresponding moisture signals depending on vegetation type. As such, these signals are not always easy to interpret, in particular because the processes of surface and volume scattering can overlay each other (Ulaby et al., 1986). However, the penetration of signals into the surface layers can also provide valuable information about surface properties.

The phase or temporal component of the microwave signal is used in SAR interferometry (InSAR) methods for generation of digital elevation models (DEMs) or surface displacement maps (Krieger et al., 2007). The coherence in InSAR expresses the correlation quality between two acquisitions and varies from 0 to 1 equalling completely decorrelated signals and perfectly correlated signals, respectively. A challenge for InSAR is low phase coherence between two SAR images due land surface changes between acquisitions (Zebker and Villasenor, 1992). However, low coherence can also indicate a direct geophysical signal resulting from land surface changes (Rignot and Zyl, 1993; Wegmuller and Werner, 1997). For example, land surface changes from snow to no snow can lead to a complete decorrelation between acquisitions (Strozzi et al., 1999).

1.2.2 TerraSAR-X

The German Aerospace Center's TanDEM-X satellite mission operates two X-Band SAR satellites launched in 2007 (TerraSAR-X) and 2010 (TanDEM-X) that operate with a wavelength of 31 mm and corresponding frequency of 9.6 GHz (DLR, 2007; Zink et al., 2012). In this thesis the term TerraSAR-X (TSX) will be used for data from both, the TerraSAR-X and the TanDEM-X satellites. The standard operational mode of TSX is the single receive antenna mode that can be used in different imaging modes. The StripMap imaging mode of TSX is a basic SAR imaging mode also used by other SAR sensors (e.g. ERS-1). In the StripMap mode the ground swath is illuminated with a continuous sequence

of pulses while the antenna beam is fixed in elevation and azimuth (Figure 1-4 b). The result is an image strip with continuous image quality and a spatial resolution of approximately 3 m. In the Starring Spotlight imaging mode of TSX a fixed target is illuminated by the steered antenna from different locations along the azimuth. The longer illumination time leads to a higher spatial resolution which can be up to 40 cm though the spatial coverage is limited (Rizzoli et al., 2017).

TSX data has been successfully applied in terrestrial Arctic environments in a variety of disciplines, such as monitoring lake ice conditions, the identification of freeze to bottom dynamics in the central Lena Delta (Antonova et al., 2016a), and the identification and characterization of different ice types in river channels (Jones et al., 2013). TSX has also been used in the terrestrial domain to monitor surface changes associated with thermokarst and thermos erosion and resulting subsidence (Antonova et al., 2018; Liu et al., 2015; Stettner et al., 2017; Zwieback et al., 2017) as well as land cover classification of Siberian wetlands (Widhalm et al., 2015) and different tundra vegetation types in the western Canadian Arctic (Ullmann et al., 2014). The sensitivity of X-Band SAR to the vegetation canopy has been explored for the potential application of Arctic shrub monitoring (Duguay et al., 2015). The TSX satellites have a consistent high geometric accuracy resulting from reliable orbit accuracy, precisely calibrated instrument delays and accurate delay and timing corrections achieving absolute geometric accuracies of subpixel level (Eineder et al., 2008).

1.3 DATA AND METHODS

A variety of satellite and ground data from two long-term observatory sites, Lena Delta and Qikiqtaruk, were used for the analysis of rapid permafrost disturbance, snowmelt and vegetation phenology, presented in the Chapters 2, 3 and 4, respectively (Table 1-2). In Chapter 2, observations of the rapid erosion of an ice-rich riverbank cliff top were made using an extensive single-orbit TSX time series with a total of 71 images, two very high spatial resolution optical images and temporally and spatially high resolution in-situ time-lapse imagery from one camera. The TSX data were segmented into cliff and no cliff areas using a threshold-based approach. The results were filtered using morphological neighbourhood filters and then vectorised in order to extract the cliff top line for a given acquisition. The cliff top lines in the optical images were manually digitized. All cliff top lines were analysed within a geoinformation system and erosion rates at 22 day and annual

intervals were extracted. Finally, Erosion rates and climate baseline data served as input for linear mixed models to analyse climatic impact on erosion.

In Chapter 3, snow cover extent (SCE) maps were generated at an 11-day temporal resolution from TSX using a thresholding on backscatter ratio images between dry and wet snow images (Nagler and Rott, 2000). Reference SCE maps were created from Landsat 8 imagery using the Normalized Difference Snow Index (NDSI) (Hall et al., 2002, 1995). The TSX data and Landsat 8 SCE maps were quantitatively compared using confusion matrices between corresponding SCE maps. A combined TSX and Landsat 8 time series of fractional snow cover (FSC) was created for selected catchments and compared to local FSC data from time-lapse observations. In Chapter 4, time series of backscatter and coherence were extracted over 30 selected areas of interest (AOIs) that were thoroughly described during a joint fieldwork campaign of the Alfred Wegener Institute (AWI) and the University of Edinburgh (UoE) in 2014. The backscatter and coherence time series were compared to the greenness excess index (GEI), a proxy for vegetation phenology and vitality that was extracted from six in-situ phenological cameras. TSX data were also compared to climatic baseline data and vegetation height.

Table 1-2: Overview of datasets, methods as well as developed data products and data sources.

	Dataset	Count	Resolution		Method	Product	Data source
			Spatial [m]	Temporal			
Lena Delta - Permafrost disturbance (Chapter 2)	TSX	71	2,4	22 days	Thresholding, vectorisation, morphological filter	annual & intra-annual erosion, input linear mixed models	German Aerospace Centre (DLR)
	GeoEye-1	1	0,5	-	digitalisation	annual erosion, input linear mixed models	commercial
	Worldview-1	1	0,5	-	digitalisation	annual erosion, input linear mixed models	commercial
	Time-lapse camera	1	0,5	4 hours	manual extraction	Video, Intra-annual erosion rates	own installation in 2015
	Climate data	-	-	1 hour	temporal aggregation	Baseline data, Input linear mixed models	http://fluxnet.fluxdata.org/
Qikiqtaruk - Snowmelt & Vegetation phenology (Chapter 3 & 4)	TSX	138	6 / 20 / 30	11; variable	dry snow / wet snow ratioing (Nagler and Rott, 2000), thresholding, Lee filter	SCE maps , FSC time-series, Backscatter & Coherence time-series	German Aerospace Centre (DLR)
	Landsat	20	30	variable	Normalized Difference Snow Index (NDSI) (Hall et al., 2002, 1995)	SCE maps from NDSI, FSC time-series	United States Geological Survey (USGS
	Time-lapse camera	7		1 hour	Greenness Excess Index (GEI)	FSC time-series, Vegetation phenology	Alfred Wegener Institute (AWI) / University of Edinburgh (UoE)
	Vegetation plots	81	0.5		Vegetation plots	Vegetation height, ecological classification	University of Edinburgh (UoE)
	Climate data	-		daily	temporal aggregation	Baseline data	Environment Canada

1.4 AIMS AND OBJECTIVES

The main objective of this thesis was to evaluate the capabilities of TSX to monitor seasonal dynamics of permafrost disturbance, snow melt and vegetation phenology (Figure 1-6). These three prominent and crucial ecosystem components have strong seasonality and are experiencing changes in both the spatial and temporal domain. To achieve this objective, TSX X-Band time series in combination with ground-based time-lapse cameras and optical remote sensing data at high to medium spatial resolutions (0.5 to 30 m) were used to extract parameters related to permafrost disturbance, snow, and vegetation.

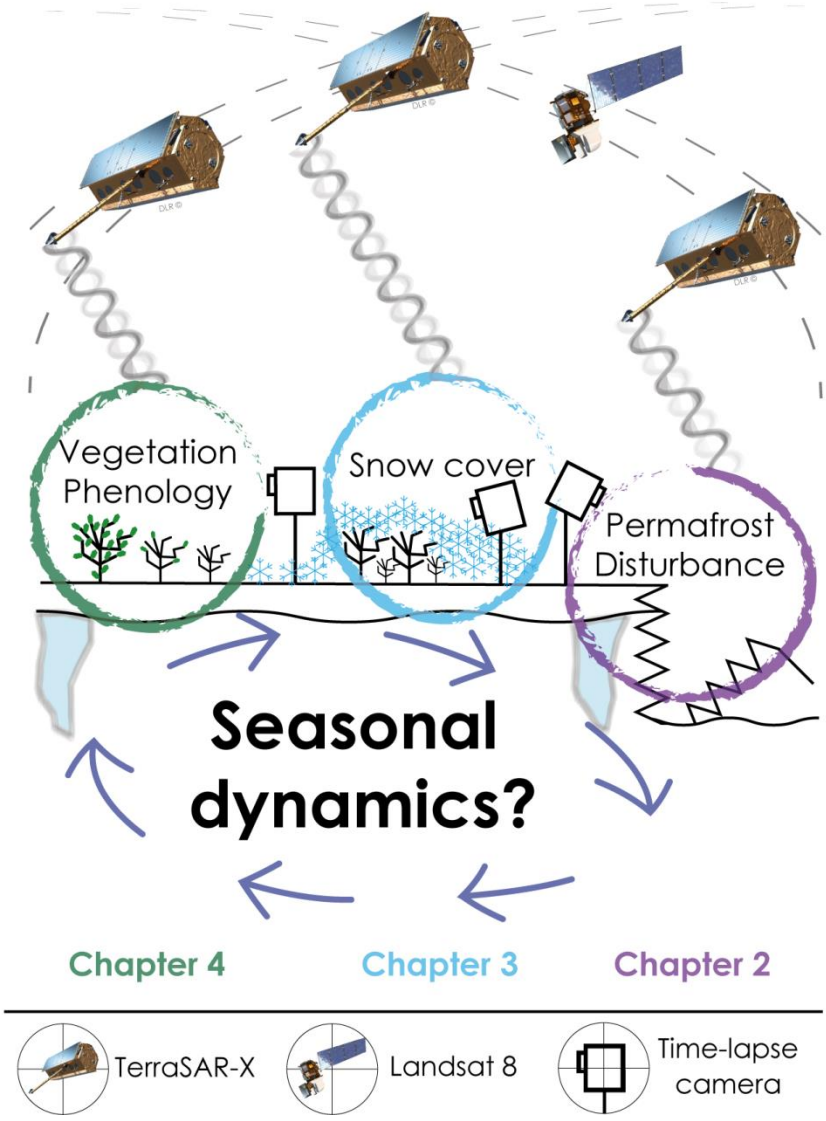

Figure 1-6: Schematic of the research focus

The thesis addresses the following three research questions:

Chapter 2 Is TSX time series capable of monitoring the dynamics of rapid permafrost degradation in ice-rich permafrost on an intra-seasonal scale and can these datasets in combination with climate data identify the climatic drivers of permafrost degradation?

Chapter 3 Can multi-pass and multi-polarized TSX time series adequately monitor seasonal snow cover and snowmelt in small Arctic catchments and how does it perform compared to optical satellite data and field-based measurements?

Chapter 4 Do TSX time series reflect the phenology of Arctic vegetation and how does the recorded signal compare to in-situ greenness data from RGB time-lapse camera data and vegetation height from field surveys?

1.5 STUDY AREAS AND DATA

The research of the thesis was conducted in the central Lena Delta, Russia (Chapter 1) and Qikiqtaruk (Herschel Island), Canada (Chapter 2 & 3).The Lena Delta in the Laptev Sea and Qikiqtaruk (Herschel Island) in the Beaufort Sea were chosen as long-term monitoring sites for TSX based on the recommendations of the PSTG resulting in high temporal resolution of TSX acquisitions. Both sites are located within the continuous permafrost zone, with more than 90% coverage of frozen ground (Figure 1-7).

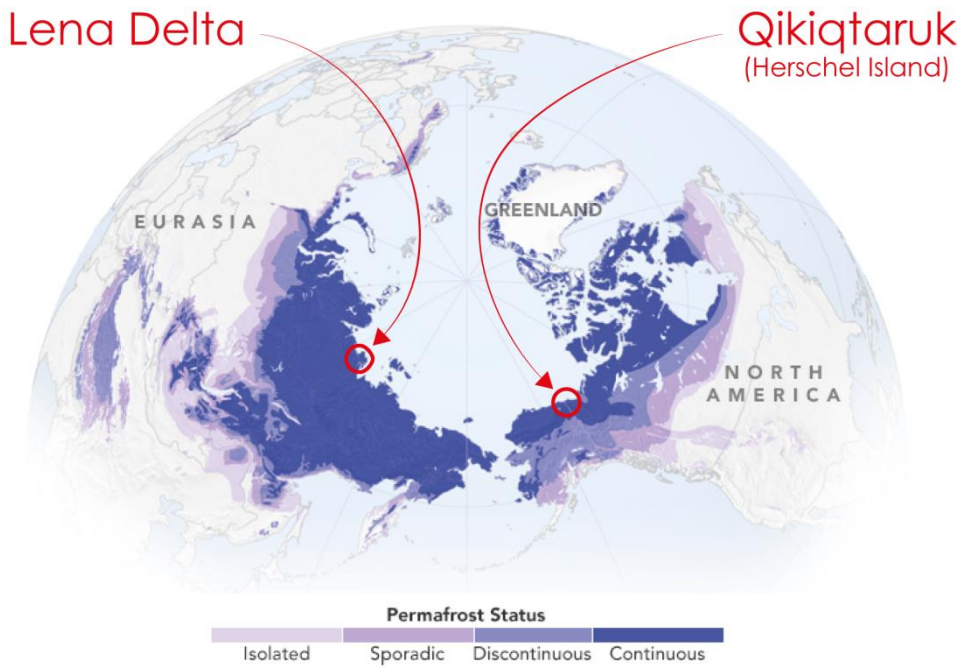

Figure 1-7: Location of the Lena Delta and Qikiqtaruk (Herschel Island) and northern hemisphere permafrost distribution. Graphic adapted from NASA Earth observatory and National Snow and Ice Data Center. https://earthobservatory.nasa.gov

The central Lena Delta at the margins of the Laptev Sea in Siberia is sparsely populated because of its remoteness but has some settlements for fisheries and transportation by ship is frequent in summer. The southern band of the Delta is characterized by remnant islands built of ice- and organic-rich sediments from the late Pleistocene that are underlain by a 15 to 21-meter-thick sand unit (Schirrmeister et al., 2011). The organic-rich upper sediments, once thawed and transported, have been shown to be quickly available for biological degradation (Vonk et al., 2013). The islands are experiencing rapid degradation by the eroding force of the Lena River, one of the largest contributors of freshwater to the Arctic ocean (Peterson et al., 2002). The majority of the annual discharge is provided during massive spring floods in early June after the winter river ice cover

breaks up and low-lying areas are inundated for days to weeks (Fedorova et al., 2015). The landscape surface is characterized by upland polygonal tundra and large thermokarst lakes and basins that can cut long coalesced bands into the topography (Morgenstern et al., 2011a). The surface of the upland is flat and poorly drained, so that ponds and standing water are common features (Schneider et al., 2009). In proximity to the thermokarst basins drainage increases and the surface is dryer, in particular on the slopes, while the basins themselves are wet and feature Holocene-aged ice wedge growth. Vegetation in the study site is mostly prostrate, characterized by dwarf shrub tundra and mosses with graminoid vegetation (Schneider et al., 2009). At the riverbanks of the dissected islands freshly eroded cliffs and bare ground are exist that are often covered by distinct surface features that result from thawing of laterally cut ice-wedge networks called Baydzarakhs (Schirrmeister et al., 2011). The riverbank cliffs can have a vertical dimension of 40 to 50 m (Morgenstern et al., 2013). Borehole data from the Lena Delta showed an increase of permafrost temperatures in the last decades (Boike et al., 2013).

Qikiqtaruk (Herschel Island) is located along the Yukon Coast in the Beaufort Sea and is a culturally important heritage site for local communities as it was the only safe natural harbour along the Yukon Coast in times of the whaling industry (Burn, 2012). Qikiqtaruk is experiencing frequent flooding and strong coastal erosion and is characterized by the existence of very large permafrost degradation features, referred to as retrogressive thaw slumps (Lantuit et al., 2012; Obu et al., 2017; Radosavljevic et al., 2015). Due to its glacial history it is composed of fine grained marine sediments that were pushed up by the last glacial advance (Fritz et al., 2012). As a result, massive ice bodies exist buried in the ground that when thawed result in the retrogressive thaw slumps along the coast and inland (Lantuit et al., 2012). Holocene-aged ice wedges are exposed in the thaw slump headwalls. The island is characterized by upland type tussock tundra that is incised by small streams, with a higher stream density in the eastern part of the Island (Ramage et al., under review). Snow cover on the island starts to develop in September and remains until the snowmelt in May. Strong winter winds predominantly come from Northwest and East and affect snow distribution (Solomon, 2005). Resulting compacted snowbanks in the valleys can stay until June and July or last throughout the summer (Burn, 2012). Qikiqtaruk has experienced a warming of air temperatures in the last 20 years that also is expressed in warmer permafrost temperatures as borehole measurements from the island show (Burn and Zhang, 2009). Satellite data has shown that spring snow cover in the region has drastically decreased in the past decades (Brown and Robinson, 2011).

1.6 THESIS STRUCTURE AND AUTHOR CONTRIBUTIONS

The thesis is composed of an introduction in Chapter 1, Chapter 2, 3 and 4 represent the three main research chapters and submitted manuscripts as well as an overall synthesis and discussion of the findings in Chapter 5. Chapter 2 is an original publication that has been published in a peer-reviewed and ISI listed scientific journal and Chapter 3 and Chapter 4 have been accepted for review in peer-reviewed, ISI listed scientific journals. Chapters 2, 3 and 4 represent stand-alone independent research. There is some overlapping general information between the publications particularly in the description of the study area, methods, and introduction sections of chapters 3 and 4 as the work was conducted in the same study area and data were used in multiple applications.

1.6.1 CHAPTER 2 - MONITORING INTER- AND INTRA-SEASONAL DYNAMICS OF RAPIDLY DEGRADING ICE-RICH PERMAFROST RIVERBANKS IN THE LENA DELTA WITH TERRASAR-X TIME SERIES

Authors: Samuel Stettner, Alison L. Beamish, Annett Bartsch, Birgit Heim, Guido Grosse, Achim Roth and Hugues Lantuit

Remote Sens. 2017, 10, 51; doi:10.3390/rs10010051

This first published manuscript presents a new method to quantify rapid degradation of ice-rich permafrost riverbanks in the central Lena Delta, Russia using TSX time series. Samuel Stettner, Annett Bartsch, Guido Grosse, Hugues Lantuit and Birgit Heim conceived and designed the study; Samuel Stettner collected, processed, and analysed all data; Hugues Lantuit, Birgit Heim and Annett Bartsch provided guidance on the analysis, and interpretation of the data; Annett Bartsch and Achim Roth contributed to the interpretation of the SAR data; Alison Beamish did the statistical analysis; Samuel Stettner wrote the paper; All authors contributed valuable edits and suggestions throughout the writing process.

1.6.2 CHAPTER 3 – TERRASAR-X TIME SERIES FILL A GAP IN SPACEBORNE SNOWMELT MONITORING OF SMALL ARCTIC CATCHMENTS

Authors: Samuel Stettner, Hugues Lantuit, Birgit Heim, Jayson Eppler, Achim Roth, Annett Bartsch, Bernhard Rabus

Remote Sens. 2018, under review. Manuscript ID: remotesensing-318946

This second manuscript, accepted for review in the Special Issue "Ten Years of TerraSAR-X – Scientific Results" in the Journal Remote Sensing presents an evaluation of the use of TSX for snow cover extent monitoring in order to study snowmelt events in small Arctic catchments. Conceptualization, Samuel Stettner, Hugues Lantuit and Birgit Heim; Data curation, Samuel Stettner and Achim Roth; Formal analysis, Samuel Stettner; Investigation, Samuel Stettner, Jayson Eppler, Annett Bartsch and Bernhard Rabus; Methodology, Samuel Stettner, Jayson Eppler, Annett Bartsch and Bernhard Rabus; Resources, Birgit Heim; Validation, Samuel Stettner, Hugues Lantuit and Birgit Heim; Visualization, Samuel Stettner; Writing – original draft, Samuel Stettner; Writing – review & editing, Hugues Lantuit, Birgit Heim, Jayson Eppler, Achim Roth, Annett Bartsch and Bernhard Rabus.

1.6.3 Chapter 4 – Estimation of Arctic tundra vegetation phenology with TerraSAR-X

Authors: Samuel Stettner, Alison Beamish, Bernhard Rabus, Jayson Eppler, Achim Roth, Annett Bartsch, Isla Myers-Smith, Hugues Lantuit, Jeff Kerby, Birgit Heim

Remote Sens. Env. under review. Manuscript ID: RSE-S-18-01373

The third manuscript, submitted in Remote Sensing of Environment links TSX backscatter time series and greenness time series from time lapse RGB imagery to Arctic vegetation phenology. Samuel Stettner, Hugues Lantuit and Birgit Heim created the concept for the paper. Samuel Stettner and Isla Myers-Smith conducted the fieldwork. Samuel Stettner, Jayson Eppler and Bernhard Rabus did the data processing. Data acquisition planning was done by Samuel Stettner and Achim Roth. Data analysis was done by Samuel Stettner and Alison Beamish. Samuel Stettner and Alison Beamish did the generation of figures and tables. Samuel Stettner and Alison Beamish wrote the manuscript. Annett Bartsch and Bernhard Rabus contributed to the interpretation of the SAR data, Jeff Kerby helped with the interpretation of the phenological data. All authors contributed to the editing of the manuscript.

Chapter 2

2 Monitoring inter- and intra-seasonal dynamics of rapidly degrading ice-rich permafrost riverbanks in the Lena Delta with TerraSAR-X time series

2.1 Abstract

Arctic warming is leading to substantial changes to permafrost including rapid degradation of ice and ice-rich coasts and riverbanks. In this study, we present and evaluate a high spatiotemporal resolution three-year time series of X-Band microwave satellite data from the TerraSAR-X (TSX) satellite to quantify cliff-top erosion (CTE) of an ice-rich permafrost riverbank in the central Lena Delta. We apply a threshold on TSX backscatter images and automatically extract cliff-top lines to derive intra- and inter-annual CTE. In order to examine the drivers of erosion we statistically compare CTE with climatic baseline data using linear mixed models and analysis of variance (ANOVA). Our evaluation of TSX-derived CTE against annual optical-derived CTE and seasonal in situ measurements showed good agreement between all three datasets. We observed continuous erosion from June to September in 2014 and 2015 with no significant seasonality across the thawing season. We found the highest net annual cliff-top erosion of 6.9 m in 2014, in accordance with above-average mean temperatures and thawing degree days as well as low precipitation. We found high net annual erosion and erosion variability in 2015 associated with moderate mean temperatures but above average precipitation. According to linear mixed models, climate parameters alone could not explain intra-seasonal erosional patterns and additional factors such as ground ice content likely drive the observed erosion. Finally, mean backscatter intensity on the cliff surface decreased from –5.29 to –6.69 dB from 2013 to 2015, respectively, likely resulting from changes in surface geometry and properties that could be connected to partial slope stabilization. Overall, we conclude that X-Band backscatter time series can successfully be used to complement optical remote sensing and in situ monitoring of rapid tundra permafrost erosion at riverbanks and coasts by reliably providing information about intra-seasonal dynamics.

2.2 INTRODUCTION

The Arctic is warming almost twice as fast as the global mean (AMAP, 2012). This phenomenon contributes to the rapid degradation of permafrost landscapes which has far-reaching implications for ecological and social systems at local and global scales (Grosse et al., 2011; Liljedahl et al., 2016; Romanovsky et al., 2010; Schuur et al., 2015). Thermokarst and thermal erosion are prominent processes associated with permafrost degradation. Thermokarst is defined as a process by which characteristic landforms result from the thawing of ice-rich permafrost or the melting of massive ice (van Everdingen, 2005), such as thaw slumps (Hugues Lantuit et al., 2012b) and thermokarst lakes or basins (Morgenstern et al., 2011a). Thermal erosion is the removal of ice-bearing permafrost by the combined thermal and mechanical action of moving water (Aré, 1988; van Everdingen, 2005), and is also the most effective process of permafrost degradation (Kanevskiy et al., 2016; Shur, 1988). It dominates the reshaping of permafrost landscapes by the erosion of ice-bearing riverbanks (Costard et al., 2014; Walker et al., 1987), coastlines (Aré, 1988; Günther et al., 2013) and lake shores (Jones et al., 2011) and leads to the formation of retrogressive thaw slumps (Lantuit et al., 2012b), as well as gullies and valleys (Morgenstern, 2012). Thermo-denudation is the combined influence of solar insulation and heat advection on the energy balance of the ground surface causing erosion above the water level (Aré, 1988).

Riverbank erosion in continuous permafrost is strongly influenced by the hydro-mechanical and thermal forces of water (Aré, 1988) but the magnitude and timing is determined by factors such as sediment type, snow and ice cover, air and water temperature, and wind (Walker et al., 1987). Thermo-erosional niching is the undercutting of cohesive, ice-rich banks by water and is a prominent process of riverbank erosion (Scott, 1978) leading to rates of up to 19 m per year (Kanevskiy et al., 2016). Different stages of erosion are observed over long time periods with riverbanks eventually stabilizing, a process that can occur in as little as three years (Kanevskiy et al., 2016). In later stages of riverbank erosion, thermo-denudation in the upper part of the bank is the main driving process leading to bank erosion. Seasonal stages define the relative contributions of thermal and mechanical components of bank retreat (Tananaev, 2016). In the lower Lena Costard et al., (2014) identified a strong seasonality in the erosion of ice-rich riverbanks with flooding and ice push during and after ice break-up in the spring as the main drivers of erosion. High variability in erosion data has been previously observed at eroding ice-

rich riverbanks (Shur et al., 2002) and is possibly linked to varying ground ice contents along bank sequences.

Ice-rich permafrost regions in Siberia have been studied extensively with regard to thermal erosion using optical remote sensing data (Günther et al., 2012; Morgenstern et al., 2014). Yet, the intra-seasonal dynamics of rapid permafrost degradation (such as the erosion of permafrost coasts or riverbanks) remain largely unknown due to a lack of intra-seasonal, high temporal resolution measurements. This is mainly due to persistent cloud coverage in the Arctic and the associated limitation in successful optical image acquisitions. High spatial resolution active microwave remote sensing is a promising alternative as it is unaffected by cloud cover and solar illumination. Synthetic Aperture Radar (SAR) antennas transmit pulses in the microwave length of the electromagnetic spectrum and receive their echoes after they propagate through the atmosphere and are scattered by objects on the earth's surface. The received microwave signal results from the physical structure and the dielectric properties of the surface in addition to parameters of the satellite viewing geometry. The resulting backscatter intensity can be used to distinguish between different land surfaces.

Today's SAR systems can provide high spatial resolution data and operate using a variety of wavelengths and polarization configurations depending on the desired application. However, in contrast to optical remote sensing, the interpretation and evaluation of SAR data from highly dynamic tundra environments is a newly developing and challenging area of research. Through joint international programs and efforts by the Polar Space Task Group (PSTG), SAR time series at high spatial and temporal resolution are increasingly available in selected tundra environments (Bartsch, 2014) offering a unique opportunity for detailed assessment of intra-seasonal permafrost degradation. SAR data has been successfully used to characterize Arctic tundra environments (Ullmann et al., 2014; Widhalm et al., 2015) and to monitor surface changes (Antonova et al., 2016b; Högström et al., 2014; Short et al., 2011). X-Band SAR data have also been used with differential interferometric SAR techniques to detect and monitor mass movements of landslides and rock falls in a variety of locations and conditions (Notti et al., 2010; Strozzi et al., 2010). Single pass interferometry with X-band SAR data has been tested for the detection of permafrost degradation features in the Arctic (Zwieback et al., 2016, 2017) and reported challenges in applying interferometric SAR to complex terrain in Arctic environments. Zwieback et al., (2017) tested interferometric methods at the same study site presented in

this paper and found that the complex topography with foreshortening and layover effects introduced a strong azimuth ambiguity. In addition, Antonova et al., (2016b) reported low coherence values over tundra surface on Kurungnakh Island, Siberia (where our site is located) using 11 day SAR multi-pass interferometry. Investigations from Widhalm et al., (2015), Antonova et al., (2016b) and Ullmann et al., (2017) on X-Band SAR data in tundra landscapes showed low spatial variability in X-Band backscatter for different tundra types (polygonal wet tundra and shrub tundra) during the snow free summer months. In contrast, bare ground conditions that occur after erosion and are accompanied by the removal of the vegetation layer have been shown to have higher backscatter in X-Band with HH polarization (Ullmann et al., 2017). The stability of the tundra backscatter and the high backscatter of bare ground allows for differentiation of these two surfaces.

In this paper, we use a three-year X-Band time series acquired by the TerraSAR-X (TSX) satellite to examine the capability of X-Band SAR to monitor erosion of an ice-rich riverbank in the central Lena Delta, Siberia at high temporal and spatial resolution. Our specific objectives are to (1) evaluate the performance of X-Band SAR data acquired by TSX for the analysis of rapid permafrost erosion against in situ and optical datasets; (2) quantify inter- and intra-annual cliff-top erosion of a rapidly eroding ice-rich permafrost riverbank; (3) investigate relationships between cliff-top erosion and climate data; and (4) examine backscatter intensity dynamics of tundra and cliff surfaces.

2.3 STUDY AREA

The study site is located within the central Lena River Delta in north-eastern Siberia between 72°–74° North and 123°–130° East (Figure 1 a). The Lena River Delta is the largest of the Arctic deltas covering about 29,000 km² (Schneider et al., 2009; Walker, 1998) and is located in the zone of continuous permafrost with a maximum permafrost thickness of 500 to 600 m (Romanovskii et al., 2004). The region is characterized by an Arctic continental climate with strong seasonal variations. The mean annual air temperature is –12.5 °C, with mean monthly temperatures in February and July of –33.1 °C and 10.1 °C, respectively (Boike et al., 2013). Rainfall occurs mostly from mid-May to the end of September with a seasonal mean of 125 mm (Boike et al., 2013). Snow cover in the Lena Delta develops between October and July with an average thickness of about 40 cm (Boike et al., 2013).

We collected erosion data on a 1930 m long rapidly eroding riverbank section on the south-eastern side of Kurungnakh Island located in the Olenekskaya channel, which is one of the four main branches of the Lena River Delta (Figure 2-1 a). The sediments at the

study site consist of fine-grained, ice- and organic-rich material that is widely distributed in Siberia and is also referred to as Yedoma (Grosse et al., 2013; Strauss et al., 2017). The distribution of Yedoma sediments in the Lena Delta is shown in Figure 2-1 a. Maximum heights of the undisturbed tundra upland on top of the Yedoma at the study site are about 55 m a.s.l. (Morgenstern et al., 2013) (Figure 2-1 c). The Yedoma at the study site features polygonal networks of large ice wedges up to 20 m deep and 5 to 7 m wide that can be exposed along the riverbank (Schirrmeister and Grigoriev, 2004). The Yedoma is underlain by a 15 to 20-m thick fine layered sand unit of fluvial origin (Schirrmeister et al., 2003). Gravimetric ice contents of the Yedoma in this area can reach up to 150 weight %, related to the dry sediment weight (Wetterich et al., 2008). The study site is located in a riverine environment without marine wave activity, about 10 km inland from the outer delta margins. The annual average water discharge of the Olenekskaya channel shows strong annual variations ranging from 700 to 1.500 m^3/s (Fedorova et al., 2015) and open water conditions exist from June to October. The water levels during spring river ice break-up in late May to early June can reach up to 12 m above normal at this location but does not exceed the upper limit of the sand unit (Figure 2-1 c). While the lower sand unit experiences fluvial erosion, the Yedoma cliff top is not directly affected by thermal erosion through Lena River waters, even during spring floods. Thermo-denudation processes at the cliff top are thus mainly driven by atmospheric influences, similar to other coastal Yedoma sites in the Laptev Sea (Günther et al., 2013), resulting in the formation of thermo-cirques, also referred to as thaw slumps. Thermal erosion is occurring at various cliff locations with complex geometry where gullies channelize runoff from the tundra of the Yedoma hinterland.

The studied cliff section is covered by small mounds of partially thawed and revegetated silty material called Baydzarakhs which remain after the thaw of ice wedge networks (Figure 2-1 c). Steep cliff headwalls feature large ice wedge exposures and indicate very high ground ice contents. Active cliff sections that undergo erosion have bare and wet ground and meltwater streams can result in channel formation. Non-active cliff sections are drier and feature pioneering vegetation. These areas show similarities to the floors of retrogressive thaw slumps, described elsewhere in the literature (Lantuit et al., 2012b). In contrast the upland is much more homogenous and characterized by an intact vegetation layer that consists of a dry moss-, sedge- and dwarf shrub-dominated tundra type and sparsely distributed ponds.

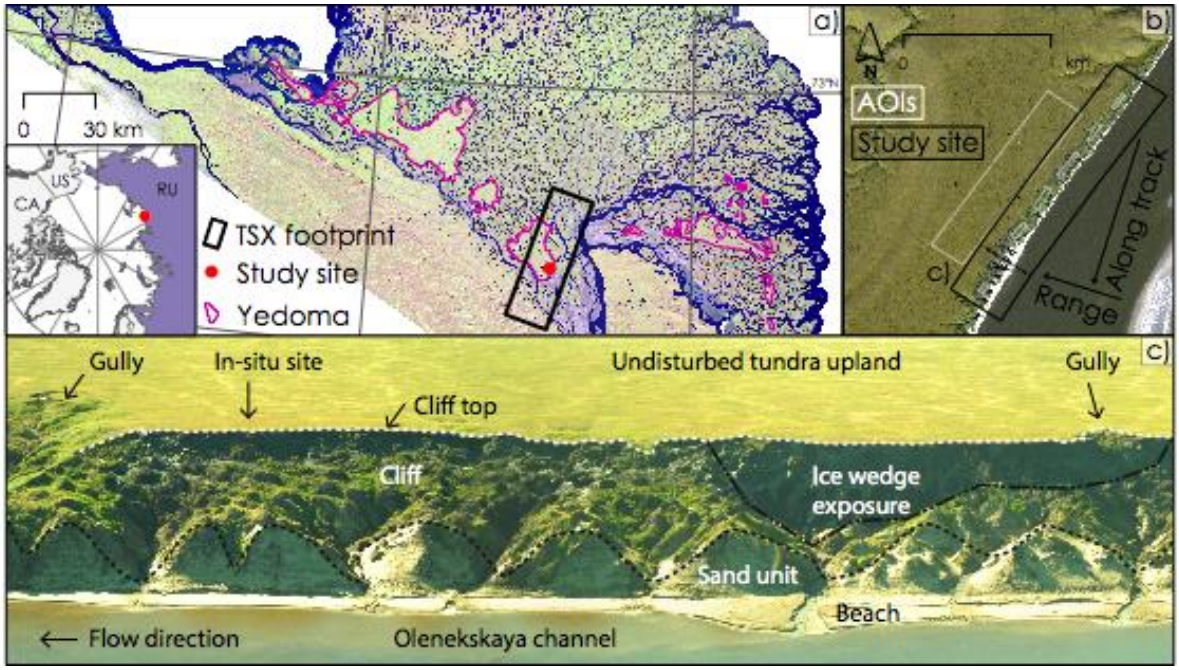

Figure 2-1: Regional overview of the Lena Delta study site. (a) The central Lena Delta with the distribution of ice- and organic-rich Yedoma deposits (Morgenstern et al., 2011b) and the footprint of the TSX data. The inset map on the lower left shows the location of the study site in Siberia, Russia (RU). The red dot in (a) marks the position of the study site shown in (b, c); (b) Viewing geometry of the SAR sensor, Areas of Interest (AOI) and study site extent; (c) stitched oblique helicopter-based photograph from the study site taken in July 2013 from helicopter showing the main terrain units.

2.4 Data and methods

2.4.1 SAR data and processing

The Lena Delta was designated as a long-term monitoring site by the German Aerospace Centre (Deutsches Zentrum für Luft- und Raumfahrt, DLR, Oberpfaffenhofen, Germany) as part of the international collaboration of the PSTG within the World Meteorological Organization. As such, a unique high temporal resolution time series of TSX data acquisitions exists for the central Lena Delta. A time series consisting of 71 SAR images was acquired between 11 March 2013 and 2 October 2015 at approximately 08:34 local time (UTC 22:34), spanning a total observation period of 935 days. The chosen orbit was in descending pass with an 11-day orbital revisit time. The SAR antenna was right-looking and the acquisition incidence angle was 31° in the scene centre. This orbit configuration allows for observation of the east facing study site without shadowing effects. The TSX images have an azimuth and range pixel spacing of 0.9 and 2.4 m, respectively, and the scene size is approximately 18 × 56 km. The TSX images were acquired in the StripMap imaging mode and delivered in processing Level 1B as dual polarized Single-Look Slant Range Complex

(SSC) images. Because of a change in the dual-polarization configuration from HH/HV to HH/VV by the DLR in May 2016, we used only the consistent HH (horizontal sent and received) polarization channel for our analyses.

All data were processed using the open source Sentinel Application Platform (SNAP) Version 3.0, provided by the European Space Agency (ESA) (ESA, 2017). In order to compare the backscatter intensity between individual SAR acquisitions the backscatter reflectivity of each acquisition must be normalized. We calibrated all TSX images and calculated the backscatter intensity ($\sigma°$) and converted it to the widely used decibel (dB) scale. We retained the highest detail possible and avoided blurring effects by not performing any kind of image filtering. Consequently, a higher level of noise, which originates from the speckle effect that is present in SAR imagery, remains in the resulting backscatter images. Continuous terrain changes between acquisitions at the cliff top prohibit precise terrain correction using a digital elevation model (DEM) and we therefore used ellipsoid-based terrain correction for all images. The geocoded images remained distorted but were comparable among each other. The expected ground range resolution is approximately 2 m, given the radar geometry of the TSX orbit with an incidence angle of 31° and a slant range resolution of 1.17 in combination with the cliff top topography with slope angles up to 45°. The radar image slant range geometry was transposed to a square image pixel size of 2.4 m and images were geocoded using an ellipsoid correction and nearest neighbour resampling to the Universal Transverse Mercator (UTM) Map projection WGS84 Zone 52 North. Exact co-location of selected images was confirmed using two corner reflectors located on southern Kurungnakh. The TSX images were subset to the extent of the study site (cliff top) to reduce computing time (Figure 2-2).

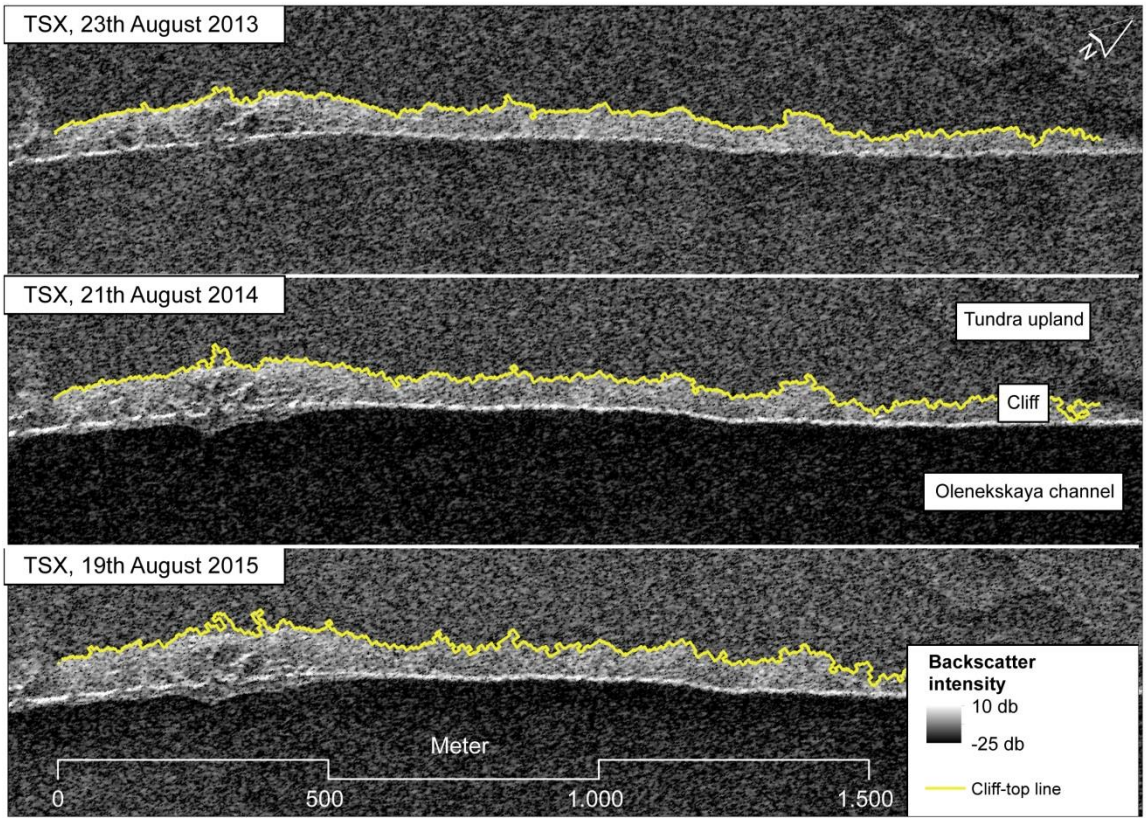

Figure 2-2: Selected spatial subsets of TSX X-Band backscatter intensity images of the study site with cliff-top lines overlaid in yellow.

Areas of interest (AOI) within the SAR image space (see Figure 1 b) were chosen based on field knowledge to analyse backscatter characteristics of cliff and tundra across the study period. AOI 'tundra' covered an area of 0.36 km2 and was representative of an undisturbed dry moss-, sedge- and dwarf shrub-dominated tundra type. AOI 'cliff' consisted of 6 subareas, covering a total of 0.02 km2 and were situated on sections of the cliff that showed characteristic high backscatter intensity in the TSX time series. The backscatter intensity value of each pixel within the AOIs was extracted from all 71 TSX images. Because frozen ground conditions and wet snow strongly alter the dielectric properties and resulting backscatter of the cliff surface, we divided the time series into "summer" (24 acquisitions) and "winter" (47 acquisitions) scenes based on the meteorological dataset. Summer was defined as images acquired when mean daily air temperatures were above 0 °C. Summer images that were likely subject to snowmelt or diurnal freezing were not considered for cliff top extraction.

2.4.2 AUTOMATED CLIFF-TOP LINE EXTRACTION FROM SAR DATA

In order to measure the amount of erosion between TSX acquisitions, the cliff tops were automatically generated for all summer TSX acquisitions (Figure 2-3). We implemented the workflow for cliff top extraction using the ModelBuilder toolbox in ArcGIS™ (ESRI© 10.3.1). The approximately perpendicular and tilted orientation of the active cliff towards the SAR sensor introduces a foreshortening effect to the SAR image that we use for image segmentation. Foreshortening further increases the higher backscatter intensity of the cliff and allows for better differentiation between cliff and tundra. We evaluated thresholds from statistic backscatter values of the AOIs against visually derived thresholds. The threshold of –10.5 dB that resulted from the difference between the means of summer backscatter intensity over the cliff and tundra AOIs did not lead to satisfactory discrimination of the cliff. Ultimately, a range of intensity thresholds was visually evaluated for the segmentation of the upper cliff boundary and tundra and a global threshold of –7.8 dB was chosen as a parameter in the automated cliff top extraction method. Using this threshold, a binary classification was performed on each backscatter image classifying all values above the global threshold as 1 (cliff) and all values below as 0 (not cliff). Due to the remaining speckle effect in the SAR imagery, some pixels within the cliff segment were classified as background and some pixels on the tundra were classified as cliff. To address this problem we applied a two-step neighbourhood filtering processing on each binary image based on closing and opening morphological filters. Both were applied using the smallest possible step size of one pixel. The cliff segments of the binary raster files were then converted to polygon vector files. In order to avoid a step-like structure in the cliff-top lines that would result from a strict conversion of the raster cell edges to a polygon, the polygons were simplified based on the algorithm by (Douglas and Peucker, 1973). We extracted a total of 24 cliff-top lines between 2013 and 2015 from the TSX time series.

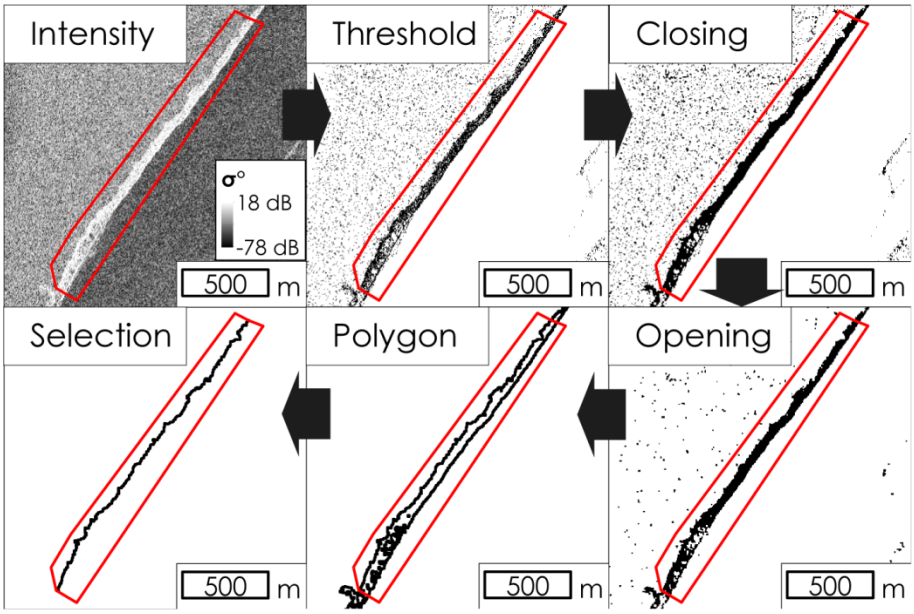

Figure 2-3: Schematic of automated cliff-top line extraction from TerraSAR-X (TSX) data. Black arrows indicate the direction of the workflow. We converted the TSX sigma nought backscatter images to a binary image (1 = cliff, 0 = background) using a global threshold. We then applied closing and opening to the cliff pixels and converted the binary images to a polygon vector file and extracted the cliff-top line.

2.4.3 Quantification of cliff-top erosion with the Digital Shoreline Analysis System

In order to quantify cliff-top erosion from the extracted cliff-top lines, we used the Digital Shoreline Analysis System (DSAS, version 4.1) in ArcGIS™ (ESRI©, 10.3.1) provided by the United States Geological Survey (Thieler et al., 2009). Using DSAS we calculated the distance in m between two cliff-top lines at the intersections with transects that are orientated perpendicular to the cliff section. We used 387 transects with 5 m spacing and a length of 250 m. We extracted cliff-top lines for every 11-day orbital pass but calculated the distance between cliff-top lines at 22-day intervals, rather than the possible 11 days to match the expected erosion at the study site to the TSX ground resolution.

The distance between two time steps is from here on referred to as cliff-top erosion (CTE). CTE was calculated for (1) all 22-day intervals of the TSX cliff-top lines; and (2) the first and last TSX cliff-top line of each year. Negative and positive CTE values reflect retrogressive and progressive cliff-top movement, respectively. Environmental factors have temporal and local differing impacts on each TSX backscatter acquisition and consequently on the derived cliff-top lines. We used the interquartile range of all CTE measurements on one transect within a year to identify outliers. We assumed that the

outliers do pick up erosion in most cases but tend to over- or underestimate CTE. If a CTE value was above or below the interquartile range of all CTE measurements along the same transect within a year it was changed and set to the 1st or 3rd quartile, respectively. We assumed only retrogressive movement of the cliff top to be true and set all positive values to zero. Additionally, we set all values that are below 1.2 m, half a pixel size of TSX, to 0, since erosion at this scale is not resolved by TSX (see 2.4.1).

Massive block failures with decametre scale commonly occur at permafrost cliffs with thermo-abrasion through waves (Aré, 1988). In this case, our filtering could potentially falsely identify cliff top accretion instead of actual erosion if the method detects the cliff-top line of a tundra block that is about to collapse and moves in offshore direction. However, at the study site presented in this paper, eroded tundra blocks are commonly smaller than 1 meter and well below the detection limit of TSX, and this effect is therefore not present in the data.

2.4.4 Cliff top mapping from optical satellite data

During the time of the TSX time series we obtained one Worldview-1 scene acquired on August 4th, 2014 in panchromatic imaging mode and 0.5 m spatial resolution and one Worldview-2 scene acquired on August 26th, 2015 in panchromatic and multispectral imaging mode with a spatial resolution of 0.5 and 1.8 m, respectively (Figure 2-4). The Worldview-2 multispectral data were pan-sharpened to obtain the highest spatial and spectral resolution using Geomatica software (PCI Geomatic's© Geomatica 2015 OrthoEngine Service Pack 1). Both images were orthorectified using rational polynomial coefficients (RPC) in an image block adjustment, which uses the geolocation information from both images in the same mathematical model. Using RPCs allows for subpixel geo-positioning accuracies with very high resolution imagery when using only a single ground control point (Fraser and Ravanbakhsh, 2009). We used a network of high accuracy ground control points from a field survey in 2013 for precise geolocation with subpixel accuracy in the UTM Map projection WGS84 Zone 52 North. The study site presents a challenging environment for delineation of high-precision ground control points since the tundra environment is very dynamic and does not feature static features such as road intersections or buildings. We used characteristic features such as small ponds and intersections of polygonal ice wedge networks which appeared stable in comparison to older high spatial resolution imagery as ground control points. As topographic input we used a digital elevation model derived from a panchromatic stereo image triplet of the

ALOS PRISM Sensor with acquisition dates of September 21st, 2006 with an absolute height accuracy of 4.41 m (Stettner, 2014). The cliff top position was manually mapped from both images at a mapping scale of 1:500, which proved to be appropriate for capturing fine details of the cliff-top line (Günther et al., 2013). Because the cliff top could not be clearly identified in the northern part of the cliff, the mapping of the optical data was only performed in the area of DSAS Transect IDs 1 to 296 covering a length of 1475 m. DSAS was used to quantify CTE between the two optical cliff-top lines.

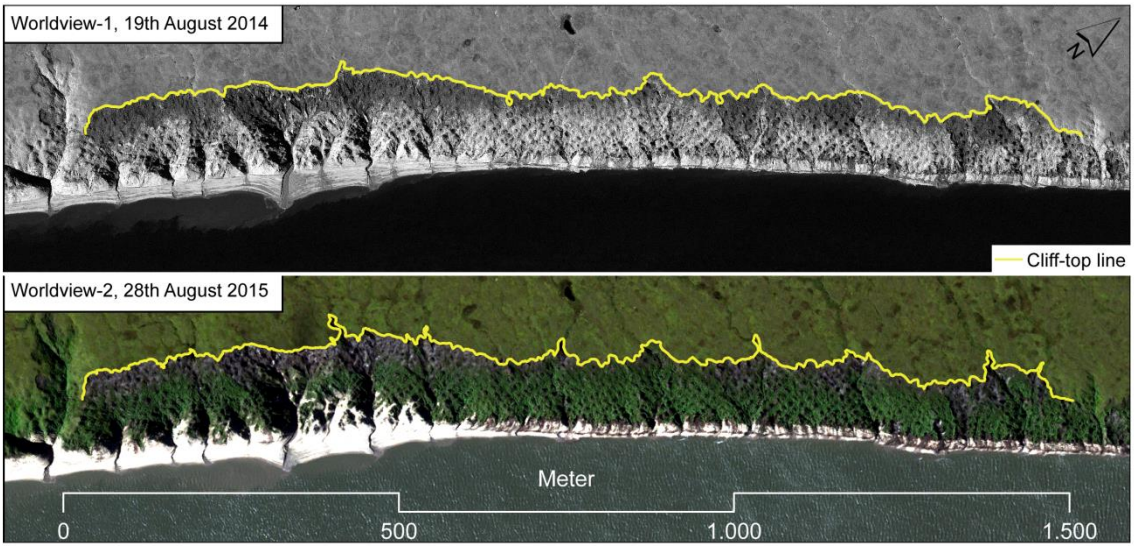

Figure 2-4: Optical satellite data and digitized cliff-top lines.

2.4.5 IN-SITU OBSERVATIONS OF CLIFF TOP EROSION

We established a 15 m transect perpendicular to the cliff top to record in situ erosion in 2015 (Figure 2-5). The transect location was chosen based on site knowledge and optical satellite imagery, which showed sustained rates of erosion and a representative cliff morphology. A total of 29 equally spaced (50 cm) wooden stakes were installed and monitored using a battery powered Brino TLC200 pro time-lapse camera mounted on a 2 m aluminum pole. Images were acquired sequentially every four hours. The camera was set up on 21 June 2015 and operated until 30 August 2015, capturing a total of 70 days. The date of the first visible instability of a stake was recorded as the date of erosion. We then calculated a theoretical daily cliff-top erosion rate.

Figure 2-5: In-situ monitoring of cliff-top erosion on Kurungnakh Island. The field photo from 21st of June 2015 shows the field of view of the time lapse camera on the eroding cliff top. The camera monitored a 15 m long transect that was set up perpendicular to the cliff-top line and consisted of 29 equally spaced (50 cm apart) wooden stakes. Photo: Samuel Stettner, June 2015.

2.4.6 CLIMATE DATA

Micro-meteorological data records from a long-term measurement station on Samoylov Island (72°22′26″ N and 126°29′45″ E), approximately 8 km northeast of the study area, were used to investigate the influence of climatic variables on erosion (Figure 2-6). The station belongs to the Fluxnet network with the ID RU-Sam (http://fluxnet.fluxdata.org/). Aggregated 30 min means of air temperature at 2 m height (°C), precipitation (mm water column), and incoming shortwave radiation (W/m2) were resampled to daily means. When less than 75% of the total measurements of the day were recorded the daily mean value was omitted. Thawing-degree days (TDD) of each year were calculated by summing positive daily mean temperature values. To examine the influence of climatic variables and their interactions on the intra-annual cliff-top erosion, we compared the median erosion rates of each of the 22-day TSX intervals from the DSAS analysis (see 2.4.3) with corresponding 22-day aggregated mean values of wind speed, temperature, TDD, incoming solar radiation as well as 22-day aggregated sums of precipitation.

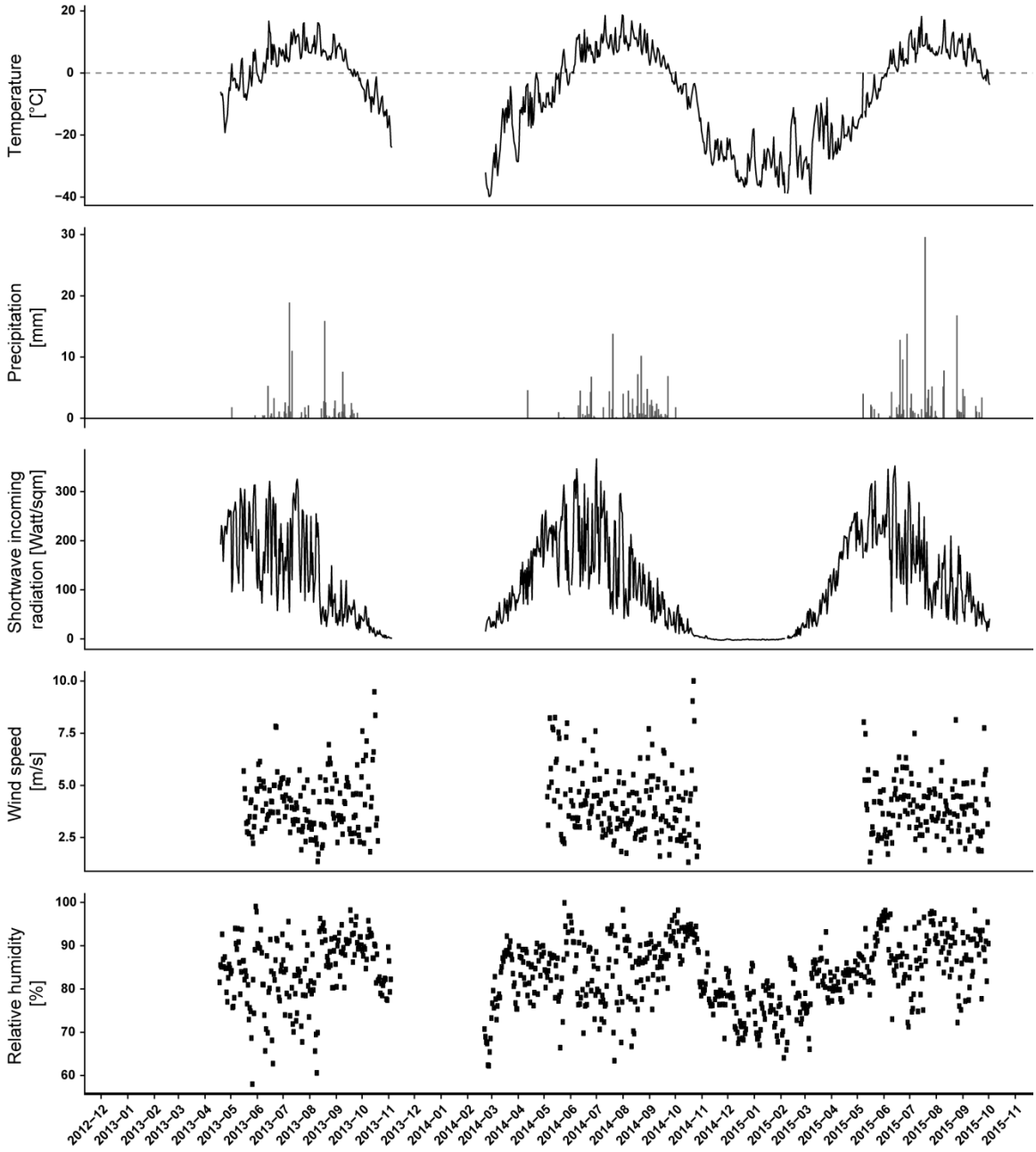

Figure 2-6: Selected climate parameters during the observation period. The data are from the weather station located on Samoylov Island, 8km northeast from the study site.

2.4.7 Statistical data analysis

To determine inter-annual variation of CTE and climate data we used analysis of variance (ANOVA). Mean CTE and net CTE of the entire cliff top, as well as mean temperature, TDD, mean incoming shortwave radiation, mean precipitation, precipitation sum, and wind speed were compared by year. Tukey's Honest Significant Differences (HST) post-hoc test was used to determine where the significant differences were for the annual data. Annual CTE and climate variables were subsequently qualitatively compared. We

compared the recorded in situ erosion data to the TSX CTE measurements on the DSAS transect that corresponded to the in situ transect. A simple t-test was used to determine if the in situ and corresponding TSX cliff-top erosion data were significantly different. A significance level (p) < 0.05 was used for all analyses. All analyses were performed using the stats package in the R Studio software environment (R Core Team, 2016).

We used linear mixed models implemented in the lme4 package within RStudio to examine the intra-annual variation of CTE within each year (Bates et al., 2014). The models were built using the 22-day CTE values with corresponding 22-day aggregated climate variables. Linear mixed models were chosen as they permit the regression of multiple explanatory variables (fixed effects) while also accounting for biases associated with time series data such as repeated measures (random effects). We defined wind speed, temperature, incoming solar radiation and precipitation as fixed effects and transect ID and mid-date as random effects to account for repeated measurements. Models were built for each year with increasing complexity beginning with the null model (no fixed effects), to all fixed effects with no interactions, and finally all fixed effects plus interactions. Models were fitted using restricted maximum likelihood due to differing fixed effects. The Akaike Information Criteria (AIC) is a criterion of the quality of the model, with lower AIC values showing better models. An ANOVA was conducted between the best fixed effect model and the null model to determine if the two were significantly different.

2.5 Results

2.5.1 TSX erosion versus in-situ and optical datasets

Extracted TSX cliff-top lines using the backscatter intensity threshold from summer 2013 to 2015 showed gradual and constant erosion at sites with simple cliff geometries (Figure 2-7 a). At locations with complex cliff geometries (gullies) and incised hinterland surfaces strong deviations up to tens of meters from previous or subsequent cliff-top lines were observed. This cliff geometry-dependent performance was also reflected in the comparison with in situ and optical data (Figure 2-7 a). The accumulated erosion of the in situ and two TSX datasets (TSX1 and TSX2), each representing 22-day intervals without 11 day temporal overlap, at a cliff section with simple geometry, were in the same order of magnitude (Table 2-1) and a t-test of theoretical daily erosion rates confirmed that the datasets were not significantly different (p < 0.05).

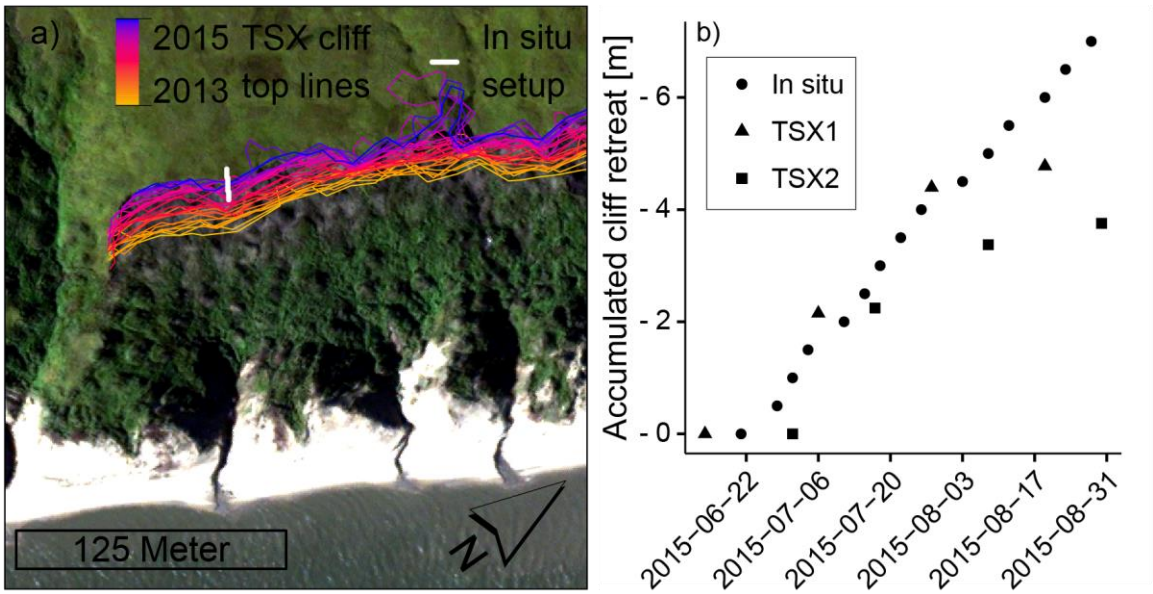

Figure 2-7: (**a**) Spatial subset of TerraSAR-X (TSX) cliff-top lines from 06/16/2013 to 08/30/2015 with underlying true-color Worldview-2 satellite image (acquired 08/26/2015).Please note that we manually compensated the offset between TSX cliff-top lines and the underlying Worldview-2 image that resulted from the differing terrain corrections applied. (**b**) Accumulated CTE of in situ and TSX measurements from 21st of June to 30th of August 2015 at the location of the time lapse profile.

Table 2-1: Comparison of in situ and TerraSAR-X derived cliff-top erosion (CTE) and theoretical cliff-top erosion rates at the location of the in situ setup. Erosion rates were calculated by dividing the net CTE by the number of days with a mean daily temperature above 0 °C in each observation period. The presented values are single measurements.

Sensor	Observation Start (yyyy-mm-dd)	Observation End (yyyy-mm-dd)	Days above 0 °C	Net CTE (m)	Theoretical Cliff-Top Erosion Rate (m/day)
In situ	2015-06-21	2015-08-30	71	- 7.0	0.09
TSX	2015-06-25	2015-08-30	67	- 5.19	0.07

When TSX and the optical data were compared across the entire cliff top including areas with complex geometry, there were greater deviations across the complex cliff sections (Figure 2-8). Overall, the southern half of the cliff (Transect ID 1–149) was characterized by stronger erosion and simple cliff geometry while the middle and northern part (Transect ID: 150–300) was characterized by complex geometry and higher variability in erosion. This spatial geometry and variability is reflected in the comparison of both datasets (Figure 2-8 a). Some of the disagreement between optical and TSX data could also be due to the differing methods of terrain correction causing shifts of ±1 transect, equalling ±5 m horizontal offsets. Despite these deviations, the net CTE and theoretical erosion rates of the optical and TSX data were overall consistent (Table 2-2).

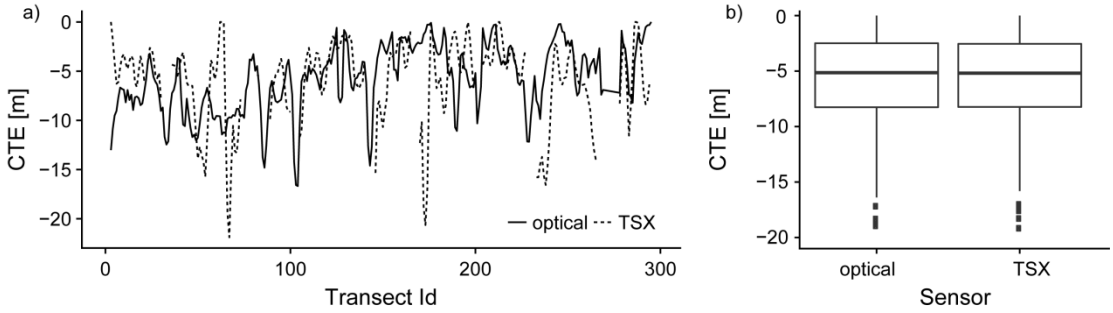

Figure 2-8: (a) Comparison of annual optical (solid) and TSX (dashed) measurements of Cliff-top erosion (CTE) along DSAS transects. CTE of both datasets was processed with a moving average with a step size of 3. TSX data at complex cliff geometries are omitted. The Transect ID number increases from south to north; (b) Boxplot diagrams of optical and TSX CTE measurements.

Table 2-2: Comparison of optical and TSX-based cliff-top erosion (CTE) measurements. Erosion rates were calculated by dividing the net CTE by the number of days with a mean daily temperature above 0 °C in each observation period. The presented values are single measurements.

Sensor	Observation Start (yyyy-mm-dd]	Observation End (yyyy-mm-dd)	Days above 0 °C	Mean net CTE (m)	Theoretical Cliff-Top Erosion Rate (m/day)
Optical	2014-08-19	2015-08-26	126	-5.78 ± 4.45	0.04
TSX	2014-08-21	2015-08-30	128	-6.92 ± 6.31	0.05

2.5.2 Inter- and intra-annual cliff-top erosion and climate data

Inter-annual variability of CTE and climate data is shown in

Table 2-3. The mean CTE of all 22-day TSX periods was highest in 2014 with –1.96 m ± 1.8 m and significantly different in all years ($p < 0.05$). In 2015 and 2013, median CTE were not significantly different. In addition to significantly higher CTE in 2014, mean temperature, TDD, and incoming shortwave radiation were all above the long-term average while recorded precipitation was lowest and no extreme precipitation events were recorded. In 2015, mean temperatures were close to the long-term mean but TDD were considerably lower and incoming shortwave radiation was at the lowest of the three years. The year 2015 also had above-average precipitation and a high number of extreme precipitation events compared to 2014 and 2013. In 2013 and 2015, between five and seven precipitation events (>10 mm) were detected, while 2014 had only light precipitation (<5 mm). Incoming shortwave radiation was highest in 2014, but in general did not show large variations across the years.

Table 2-3: Annual characteristics of erosion and climate at the study site. The mean and median cliff-top erosion (CTE) per 22-days represents the average of all TSX 22-day steps within one year. In contrast, the mean net CTE is derived from the comparison of the first and last TSX summer observation of each year. The climate data in this table represent a temporal subset from June to September.

	2013	2014	2015	Long Term Mean *
Mean CTE per 22-days (m)	−1.37 ± 1.55 [a]	−1.96 ± 1.85 [b]	−1.85 ± 1.97 [c]	
Median CTE per 22-days (m)	−1.24	−1.9	−1.49	
Mean net CTE (m)	−4.1 ± 3.7 (88 days) [a]	−6.9 ± 4.6 (88 days) [b]	−5.1 ± 5.3 (66 days) [c]	
Mean Temperature (°C) (June to September)	6.1 ± 4.8 [a]	7.6 ± 4.7 [b]	6.4 ± 4.4 [ab]	6.4 ± 3.4 (1998–2014)
Thawing-degree days (June to September)	691.9	824.2	628.9	790 ± 120 (1998–2014)
Mean incoming short wave radiation (W/m²) (June to September)	133 ± 87.2 [a]	141.4 ± 91 [a]	130.9 ± 81.7 [a]	-
Mean Precipitation (mm) (June to September)	0.9 ± 2.6 [a]	0.8 ± 1.6 [a]	1.1 ± 2.9 [a]	1.3 ± 3.1 (1998–2008)
Precipitation sum (mm) (June to September)	109	104	146	124 ± 69 (1998–2008)
No of extreme precipitation events >15/10/5 mm (June to September)	2/3/5	0/0/5	2/5/8	1.45 ± 1.30/2.58 ± 1.83/ 6.5 ± 4.23 (1998–2008)

[a,b,c] different letters within a row represent significantly different means with $p < 0.05$; * Long term mean data (1998 to 2012) was taken at a micro-meteorological weather station (Boike et al., 2013) with the same instrumentation as the climatic record.

In general, intra-annual CTE did not show any strong or consistent seasonal trends (Figure 2-9). In 2013 CTE was lowest and could only be detected in the early and late season. In 2014 two peaks of CTE were observed, the early season showed the highest CTE between end of June and mid-July, after which July showed low CTE values. Early August showed high CTE values and late August again had low values. 2015 showed high CTE in the early and late season, with a minimum observed in July.

The influence of climatic variables on intra-annual CTE was examined by linear mixed models and results are presented in Table 2-4. The results of the linear mixed models suggest that overall the measured climate variables do not have a consistent influence on variations in 22-day CTE within each year. In 2013 the combination of incoming shortwave radiation, TDD, and precipitation sum had the strongest effect on erosion. In 2014, precipitation sum alone was identified as an influential parameter on erosion, although

the result was not significantly different from the null model (no fixed effects). In 2015 both precipitation sum and incoming shortwave radiation influenced CTE. In 2013 and 2015 the models were significantly different than the null model, while the 2014 model was not.

Table 2-4: Results of the linear mixed models fitted by restricted maximum likelihood with middate (MD) and TransectID (TID) as random effects. Fixed effects included: CTE: cliff-top erosion, SWIN: incoming shortwave radiation, P: precipitation, TDD: thawing-degree days. AIC: Akaike Information Criterion, BIC: Bayesian Information Criterion. p-values represent results from analysis of variance between the model and null model (no fixed effects).

Year	Fixed Effects	Random Effects	AIC	BIC	*p*-Value
2013	CTE~SWIN + P + TDD	MD + TID	7138.6	7138.6	<0.01
2014	CTE~P	MD + TID	10,993.4	1102.9	>0.05
2015	CTE~SWIN + P	MD + TID	10,962.7	10,998.0	<0.05

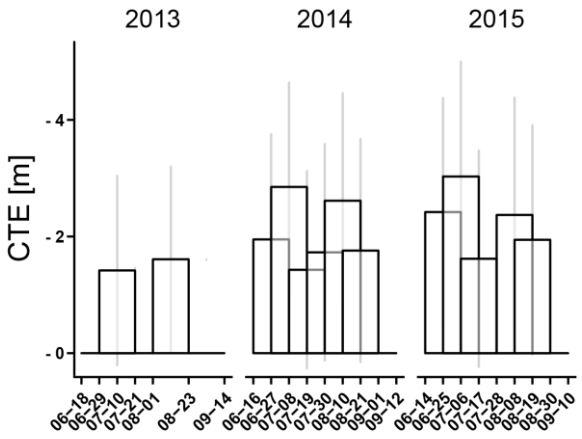

Figure 2-9: Intra-seasonal median cliff-top erosion (CTE) from TerraSAR-X (TSX) 22-day observation periods for the years 2013, 2014 and 2015. Grey vertical lines represent the standard deviation. Please note that observation periods are overlapping in most cases. The overlap is linked to the method used to report on the data: TSX has a repeat pass of 11 days, but we chose here to present all 22-day combinations of CTE data

2.5.3 BACKSCATTER TIME SERIES

To understand how the surface properties driving erosion rates were changing, the backscatter intensity of the observation period was examined. Backscatter intensity of the cliff was higher in the summer months and showed a decreasing trend from early to late summer (Figure 2-10). In all years the cliff showed a peak in backscatter intensity at the beginning of summer between mid-April and mid-May during the transition to above freezing air temperatures and snowmelt. The early season peak in 2013 was less strongly expressed than in 2014 and 2015. Also, in 2013 the earliest onset (early May) of

temperatures above 0 °C was observed. By contrast, 2015 temperatures did not reach above 0 °C until the beginning of June. The summer tundra backscatter intensity was slightly lower in 2013 and 2014 than in 2015. In the late season of 2013 and 2014 when temperatures dropped below 0 °C cliff backscatter showed a drop of approximately 3 dB. An ANOVA revealed that backscatter intensity was significantly different between all years for both cliff and tundra with $p < 0.005$. A general decrease in backscatter intensity of the cliff and an increase in backscatter intensity of the tundra were observed over the three years (Figure 2-10).

A general divergence of mean backscatter values of the cliff and tundra in summer and convergence in winter was observed. There was a clear difference in the summer acquisitions in all years as shown in Figure 2-5. The chosen threshold of –7.8 dB was below the median of cliff AOIs and above the 1st quartile of the tundra AOI in all years. The mean summer tundra backscatter of –15.5 ± 6.5 dB was significantly lower and less variable than the mean summer cliff backscatter of –6.4 ± 6.9 dB ($p < 0.05$) (Table 2-5). Backscatter of the tundra surface increased from –16.3 ± 6.5 to –15.6 ± –6.5 to –14.8 ± 6.5 dB in the summers of 2013, 2014 and 2015, respectively. The cliff surface showed a slight decrease of backscatter from –5.3 ± 6.6 to –6.7 ± 7 dB from summer 2013 to 2015, respectively.

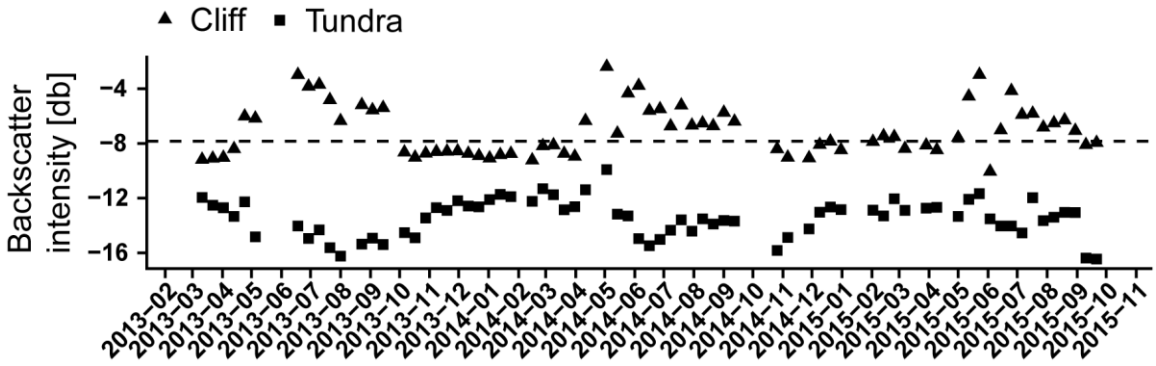

Figure 2-10: Median sigma nought backscatter of TSX acquisitions in cliff (triangles) and tundra (squares) AOIs. The dashed line shows the visually derived threshold of –7.8 dB.

Table 2-5: Mean backscatter over Areas of interest (AOI) by year.

	AOI	2013	2014	2015	All
Mean summer backscatter	Tundra	–16.29 ± 6.53 [a]	–15.62 ± 6.47 [b]	–14.81 ± 6.47 [c]	–15.50 ± 6.51
	cliff	–5.29 ±6.65 [a]	–6.88 ± 6.93 [b]	–6.69 ± 7.05 [c]	–6.39 ± 6.93

[a,b,c] different letters within a row represent significantly different means with $p < 0.005$

2.6 DISCUSSION

Three years of riverbank cliff-top-erosion data from the Lena Delta, Siberia highlight the potential of spatially and temporally high-resolution SAR backscatter time series to monitor rapid tundra disturbance by the degradation of ice-rich permafrost at an inter- and intra-annual scale. This study presents a novel application of TSX X-Band to monitor cliff-top erosion in Arctic tundra.

2.6.1 INTER-ANNUAL DYNAMICS OF CLIFF-TOP EROSION

The mean annual net erosion of the entire cliff top derived from the filtered TSX data of -4.1 to - 6.9 m per year falls within the range of reported rates of riverbank cliff-top erosion at other Siberian river delta sites (Yana and Indigirka) with comparable cliff height and thermo-denudation-affected systems between 1950 and 1990 (Shur et al., 2002). The mean annual TSX erosion rate of - 6.9 m in summer 2015 was further validated by the optical data, which showed mean erosion rates of - 5.8 m falling within the variance range of one standard deviation (Table 2-2).

Our analyses showed that mean annual net erosion was significantly different between all years. To better understand the inter-annual differences, we examined mean annual climatic variables in relation to long-term, 10-year means. We found that in 2014 erosion was highest, concurrent with above-average air temperatures, the highest thawing-degree days and shortwave incoming solar radiation, as well as low precipitation. This finding emphasizes the link between air temperatures and ice-rich permafrost degradation and highlights the potential for greater release of material in the fluvial system (Kokelj et al., 2015). Interestingly, in 2015 the erosional activity was significantly higher than in 2013 even though air temperatures were comparable and thawing-degree days and solar radiation were lower. This suggests that the difference between these two years was the result of above-average precipitation both in frequency and intensity. Precipitation has been directly linked to ice-rich permafrost erosion in previous studies (Kokelj et al., 2015). The difference between years and the corresponding climatic conditions suggests a contingent sensitivity of erosion to temperature and precipitation. In other words, precipitation appears to be an important factor when temperatures are at or below average whereas when temperatures are above average, precipitation has less of an influence.

2.6.2 Intra-annual dynamics of cliff-top erosion

Erosion was detected in all analysed 22-day time steps but no obvious seasonal patterns were observed. The onset of erosion occurs in spring when a threshold of air temperature or ground warming is reached. At this time, water availability from snowmelt can lead to increasing erosion potential (Dupeyrat et al., 2011). Rapid riverbank erosion with high seasonality in spring has been recorded in the lower Lena River (Costard et al., 2014). In our riverbank system we could not observe any statistically significant seasonal peaks of erosion that would indicate times with high erosion. The base of the cliff section in our study is not made of ice-rich and highly erodible sediments but is composed of a sand unit that buffers the thermo-erosional activity of the Lena River also during spring flood. This prevents the development of thermo-erosional niches and consequently the rapid erosion by block collapse that is an important component at other Arctic riverbank and coastal cliff systems (Günther et al., 2013; Kanevskiy et al., 2016; Scott, 1978). Given that the cliff top is decoupled from the thermo-erosional processes of the Lena River, its erosion likely results from atmospheric forcing and depends on the local sediment and ground ice properties (Ramage et al., 2017), as well as regional climatic conditions (Schuur et al., 2015). This link explains the relatively gradual thermo-denudation at the cliff top. Interestingly, intra-annual (22-day time steps) erosion was most consistently influenced by precipitation as indicated by the results of the linear mixed models. This result suggests that precipitation has a greater influence over shorter periods of time than temperature. This phenomenon has been documented by Kokelj et al., (2015) who found greater sediment outflow from eroding thaw slumps three to four days following precipitation events. Though precipitation was identified as the most important variable statistically, it is the interaction between temperature, precipitation, and incoming solar radiation that best explains the variability in intra-annual erosion rates.

2.6.3 Backscatter dynamics of tundra and cliff surfaces

The backscatter time series clearly demonstrates the ability of SAR X-band data to differentiate between undisturbed tundra and the cliff, justifying the applied thresholding method. In addition, examining the backscatter time series provides insight into changing tundra and cliff surface properties. The observed lower cliff backscatter in 2014 and 2015, compared to 2013, could be the result of a flattened surface geometry and/or partial re-vegetation of the cliff surface. Both effects take place during cliff stabilization of ice-rich permafrost riverbank sites. Kanevskiy et al., (2016) showed that rapidly eroding ice-rich

vertical riverbank cliffs can stabilize to a flattened cliff with Baydzarakhs (soil remaining after melting of massive ground ice) and vegetation within as little as four years. The ground surface flattens when the cliff top retreats further inland while the cliff base, in our case the underlying sand unit, remains stable. The lower cliff slope angle consequently decreases the effect of foreshortening in the SAR data. Additionally, vegetation is likely to establish relatively quickly on previously eroded and now stable flattened surfaces. Fresh vegetation canopy can increase the fraction of volume scattering and positively affect backscatter intensity (Antonova et al., 2016b). Existing studies on the effect of tundra vegetation on backscatter (Duguay et al., 2015; Ullmann et al., 2014, 2017) do not address the effect of fresh vegetation on previously degraded tundra surfaces. The mixed signals of vegetated and eroding surfaces within the cliff AOIs could explain the higher standard deviations of backscatter in 2015. The active cliff top eroded inland while our chosen cliff AOIs were static and stayed at the same location. Consequently, the scar zone slowly moved out of the AOI and was less represented in the backscatter signature. This time series suggests that segmentation of tundra and cliff using a simple thresholding on X-band backscatter could become more challenging if summer backscatter signatures of cliff and tundra continue to converge over time.

The backscatter time series additionally showed variability during the winter-summer transition, which is very likely driven by changes in the dielectric properties of the ground. When the ground surface was frozen during winter, backscatter signatures of the cliff were lower than in summer but during the transition, values were highly variable over short periods of time. As a result, SAR acquisitions dated before and during snowmelt and during frozen ground conditions were not considered for cliff top retreat analysis. This exclusion could potentially misrepresent important early season dynamics and annual estimates of erosion, but CTE measurements between the last acquisitions of a season to the first acquisition of the following season showed low erosion values, indicating little erosion in this time. In addition, the observed variability of backscatter could indicate the influence of soil moisture on backscatter from bare surfaces in summer which has been shown to increase backscatter by up to 5dB in X-Band (Gorrab et al., 2015). The impact of soil moisture on backscatter could have implications for image thresholding and resulting cliff-top extraction.

Complex cliff geometries at water tracks and gullies and less steep stabilized cliff sections could also introduce variability into the TSX backscatter data. The sensitivity of radar to

non-line-of-sight features is known, terrain features with steep scarps not aligned to orbit direction have been shown to introduce illumination error (Shi et al., 2017) and shallower slopes impact backscatter angle, both reducing backscatter intensity and the foreshortening effect (Eriksen et al., 2017). These complex non-linear features can introduce errors to the extracted cliff-top line position and should be taken into consideration when monitoring at intra-annual timescales.

2.7 Conclusions

This study demonstrates that high temporal TSX X-Band backscatter time series in HH polarization can monitor intra-and inter-annual cliff-top erosion dynamics of a Siberian ice-rich riverbank at 22-day intervals. This resolution represents a temporal resolution that was previously challenging for Arctic remote sensing data. A backscatter threshold of –7.8 dB was used to separate the stable and low backscatter signature of –15.5 dB of undisturbed tundra upland and the high backscatter signature of –6.4 dB, of non-vegetated cliff top of summer time acquisitions. We successfully derived cliff-top erosion data across three years from a total of 24 acquisitions. We evaluated these TSX-derived CTE against in situ and optical satellite observations and found that they show comparable seasonal and annual cliff-top erosion. The method is affected by high terrain complexity, by non-line-of-sight features and also by high surface soil moisture. All three impact the automatic extraction of cliff top and make TSX susceptible to over- and underestimation.

We show that ice-rich Yedoma riverbank cliff tops erode consistently throughout the thawing season with little seasonality, largely through thermo-denudation. Maximum erosion rates appeared to be affected by warm air temperatures but precipitation is also important in years when temperatures are below or at long-term averages. Intra-annual erosion rates seemed to be consistently affected by precipitation. However, unmeasured small-scale microclimatic parameters, micro topography and ground ice content are also likely to impact the magnitude of the erosion rates. Overall, this novel method represents a promising new tool to assess rapid changes linked to tundra disturbance and permafrost degradation.

2.8 ACKNOWLEDGMENTS

The authors want to thank the German Helmholtz Alliance Earth System Dynamics (EDA) for partial funding of this project and access to the TSX datasets. Samuel Stettner and Hugues Lantuit were additionally supported through HGF COPER, Guido Grosse through ERC PETA-CARB (ERC #338335) and Annett Bartsch through the European Space Agency project DUE GlobPermafrost (Contract Number 4000116196/15/I-NB). They also thank Julia Boike (AWI Potsdam), Lars Kutzbach (University of Hamburg) and Christian Wille (GFZ Potsdam) for providing the climatic data records. We thank Barbara Widhalm for support in TSX data processing for an early version of the datasets presented in this manuscript. Special thanks to Alexander Winkler and Norman Rößger that were affiliated to the University of Hamburg and Günther Stoof from AWI Potsdam for their help during the field campaign in spring 2015. Many thanks also to the station staff on the Samoylov research station and the AWI logistics for providing excellent field research conditions!

Chapter 3

3 TerraSAR-X time series fill a gap in spaceborne snowmelt monitoring of small Arctic catchments

3.1 Abstract

The timing of snowmelt is an important turning point in the seasonal cycle of small Arctic catchments. The TerraSAR-X (TSX) satellite mission is a synthetic aperture radar system (SAR) with high potential to measure the high spatiotemporal variability of snow cover extent (SCE) and fractional snow cover (FSC) on the small catchment scale. We investigate the performance of multi-polarized and multi-pass TSX X-Band SAR data in monitoring SCE and FSC in small Arctic tundra catchments of Qikiqtaruk (Herschel Island) off the Yukon Coast in the Western Canadian Arctic. We quantitatively compared TSX and Landsat 8 derived SCE maps using confusion matrices and analysed the spatiotemporal dynamics of snowmelt from 2015 to 2017 using TSX, Landsat 8 and in-situ time lapse data. Our data showed that the quality of SCE maps from TSX X-Band data is strongly influenced by polarization and to a lesser degree by incidence angle. VH polarized TSX data performed best in deriving SCE when compared to Landsat 8. TSX derived SCE maps from VH polarization were additionally able to detect late lying snow patches that were not detected by Landsat 8. Results of the in-situ data validation showed that TSX FSC was also accurately capturing the temporal dynamics of different snowmelt regimes, while Landsat 8 had fundamental data gaps in all three snowmelt periods due to cloud cover. However, validation results also revealed that diurnal temperature variations in the early snowmelt season impact the capability of TSX to detect wet snow cover and have to be considered during mission planning. We conclude that TSX performs at a significantly higher temporal resolution than Landsat 8 data and provides a more complete temporal picture of snowmelt dynamics than optical data, which due to cloud related data gaps generally only indicated the onset and end of snowmelt.

3.2 Introduction

The evolution of snowmelt is a crucial component in the seasonal cycle of small Arctic catchments; affecting temporal and spatial patterns of hydrology, vegetation, and biogeochemical processes. Snow insulates permafrost-affected soils from cold temperatures in winter and from warm temperatures in spring (Ling and Zhang, 2003;

Zhang et al., 1996; Zhang and Stamnes, 1998). Deeper and prolonged winter snow cover can increase permafrost temperatures and over time can lead to increased active layer thickness, soil nutrient availability, and shifts in vegetation composition (Johansson et al., 2013; Krab et al., 2017; Schimel et al., 2004; Semenchuk et al., 2015). In addition, late lying snow patches affect the soil moisture content and thermal properties of the active layer late in the season and create unique vegetation communities beneath and in their vicinity (Ballantyne, 1978). Both prolonged winter snow and late lying snow patch dynamics directly affect heterotrophic soil respiration and consequently carbon cycling (Bartsch et al., 2007; Brooks et al., 2011; Hobbie and Chapin, 1996; Ostendorf et al., 1996; Schimel et al., 1996, 2004).

The time between the onset and end of snowmelt initiates the hydrological year, drives vegetation phenology, and marks an increase in soil biogeochemical activity (Billings and Mooney, 1968; Hinzman et al., 1996; Woo, 1976). In small Arctic catchments, snowmelt is often the most important hydrological driver and generates the majority of annual discharge (Pohl and Marsh, 2006). The timing of snowmelt, as opposed to temperature, drives the onset of vegetation phenology and thus influences subsequent phenological phases and overall fitness of individual plants (Billings and Bliss, 1959; Bjorkman et al., 2015a). On regional scale spring snow cover in May and June in the Northern Hemisphere has decreased drastically in the last 30 years following trends of increasing air temperatures and reductions in sea ice extent and duration (Brown and Robinson, 2011). On a local scale, changes in winter precipitation in the Arctic are expected to be highly variable in space and time (Weller et al., 2005). Furthermore the spatial variability of snow cover extent (SCE) and the temporal variability of snowmelt, expressed on a catchment scale through changes in fractional snow cover (FSC), is inherently high due to low vegetation and snow redistribution by strong and prevailing wind patterns (Clark et al., 2011; Liston and Liston, 2004). Adding to the uncertainty in changes to SCE and snowmelt is the observed expansion of tall shrubs across the Arctic which will greatly impact the distribution and depth of snow (Myers-Smith et al., 2011; Sturm et al., 2001). Consequently, the monitoring of snowmelt at high spatial and temporal scales is important to better understand the impacts of changing SCE on the abiotic and biotic functioning of small catchments in a rapidly changing Arctic.

Currently in Arctic regions there is no operational product available that captures snow cover in simultaneously high temporal and spatial resolution. Snow cover products from

remote sensing data sources are predominantly derived from optical and microwave sensors. To detect snow, optical sensors rely on the high proportion of reflected radiation in the visible spectrum in contrast to very low reflection in the near infrared part of the electromagnetic spectrum. Common optical sensors for snow cover retrieval include the Moderate Resolution Imaging Spectroradiometer (MODIS), the Advanced Very High Resolution Radiometer (AVHRR), and the Landsat series (Dietz et al., 2012). MODIS has a spatial resolution of up to 250 m and theoretically delivers a daily snow product. AVHRR also delivers daily snow cover information with a 1 km spatial resolution. Landsat 8 acquires imagery at a spatial resolution of 30 m and with a revisit time of 16 days (Irons et al., 2012). The theoretical temporal resolution of MODIS and AVHRR would be sufficient to track the temporal dynamic of snowmelt, but their spatial resolution is not sufficient to capture snowmelt at the small Arctic catchment scale. Landsat 8 offers a spatial resolution sufficient for analysis at the small catchment scale and in Arctic regions converging satellite orbit paths increase the temporal resolution, which would allow monitoring of the highly dynamic phenomenon of snowmelt (Salomonson and Appel, 2004). However, the retrieval of snow cover from optical sensors in Arctic regions is often challenging due to complete and fragmented cloud cover which introduces gaps in the time series or errors in snow detection (Stow et al., 2004). This limits optical time series spatially and temporally, consequently prohibiting fine-scale mapping of the rapid and spatially variable phenomenon of snowmelt. Microwave satellite systems operate largely unaffected by atmospheric distortions from water vapour and clouds and also are independent of solar illumination; as a result they can acquire data at all times. Passive microwave systems can detect snow cover and snow properties at high temporal resolution (Romanov et al., 2000), but the acquired imagery is at a coarse km scale spatial resolution, which is unsuitable for small catchment analyses. Recent active microwave satellite missions operating in Synthetic Aperture Radar (SAR) modes can obtain imagery in sufficient spatial and temporal resolution for small catchment based analysis.

The German active microwave TerraSAR-X (TSX) satellite mission has high potential to address the temporal limitations of operational optical and spatial limitations of other microwave missions by reliably providing imagery in high spatial and reasonable temporal resolution through combining different orbits and viewing geometries. The TSX satellites have a revisit time of 11 days and acquire imagery at a spatial ground range resolution of 1.7 to 3.5 m in the StripMap imaging mode with incidence angles between 20 and 45° (Roth et al., 2002). TSX is a SAR system that emits pulses in the microwave length of the

electromagnetic spectrum, which propagate through the atmosphere. The SAR antenna receives the pulse echoes after being scattered by objects on the Earth's surface, transmitting the physical structure and dielectric properties of the surface. The amplitude of these echoes determines the backscatter intensity and can be used to describe and classify different surfaces. However, a prominent feature of SAR imagery is the speckle effect which introduces a variation to the image texture in a granular pattern that does not arise from the imaged surface but from the SAR system itself. This signal is often regarded as unwanted noise and makes averaging necessary to retrieve the actual mean backscatter amplitude of the surface.

Air, ice and at times liquid water make up a snowpack. The main parameters differentiating the backscatter of dry snow and soil background is the mass of snow or snow water equivalent (SWE), the size of the snow grains, and the roughness and dielectric properties of the soil (Rott et al., 2009; Ulaby and Stiles, 1980). As air does not influence the transmitted microwave signal (Mätzler, 1994; Mätzler and Wegmüller, 1987), the propagation and backscatter of microwaves from a snowpack depend on the dielectric constants of ice and water, which are very different and can be used to map snow volume and cover (Leinss, Parrella, and Hajnsek 2014; Schellenberger et al. 2012). In general, wet snow is easily classified due to free water within the snowpack strongly attenuating the microwave signal (Schellenberger et al. 2011; Nagler and Rott 2000). The ability of X-band SAR systems like TSX or COSMO-SkyMed to map wet snow due to attenuation of the microwave signal by free water within the snowpack has been widely reported (H Rott and Nagler 1993; Nagler 1996; Nagler and Rott 2000; D. Floricioiu and Rott 2001; Schellenberger et al. 2012; Wendleder et al. 2015). The presence of wet snow in a snowpack is indicative of the onset of snowmelt and therefore offers an opportunity to monitor snowmelt dynamics in high spatial and temporal detail.

Our research goal is to resolve the spatiotemporal patterns of the highly dynamic seasonal snowmelt in small Arctic catchments by combining time series of multi-orbit and multi-polarization TSX data with optical remote sensing data and in-situ observations. We investigate snowmelt dynamics of three years in small Arctic catchments at the long-term Canadian Arctic terrestrial observatory Qikiqtaruk (Herschel Island) that is also part of the World Meteorological Organization's Polar Space Task Group initiated TSX long-term monitoring dedicated to permafrost applications (Bartsch et al., 2014). We address the following research questions: (1) How does TSX perform in mapping SCE in small Arctic

tundra catchments compared to Landsat 8 optical satellite data; (2) How does TSX resolve temporal dynamics of snowmelt compared to in-situ observations and (3) What are the spatiotemporal dynamics of fractional snow cover from 2015 to 2017 in the small catchments of Qikiqtaruk? In order to answer these questions, we performed a quantitative comparison of snow cover extent (SCE) from Landsat 8 with SCE products derived from three different TSX polarizations at different incidence angles. In a second step we validate catchment based FSC derived from TSX and Landsat 8 with in-situ observations and relate the results to catchment characteristics.

3.3 STUDY AREA

Qikiqtaruk (Herschel Island; 69°34′N; 138°55′W) is located off the north-western Yukon coast in the Western Canadian Arctic approximately 2 km from the mainland (Figure 3-1). The climate of Qikiqtaruk is polar continental with mean annual air temperatures between -9.9 and -11 °C and mean annual precipitation between 161 and 254 mm year^{-1} (C R Burn, 2012). The dominant wind direction is northwest and storms are frequently observed in late August and September (Solomon, 2005). The island is characterized by rolling hills with a maximum elevation of 183 m above sea level and polygonal tundra that is dissected by a variety of different valley types (De Krom, 1990; Rampton, 1982). There is only one larger water body in the centre of the Island, referred to by the local community as Water Lake.

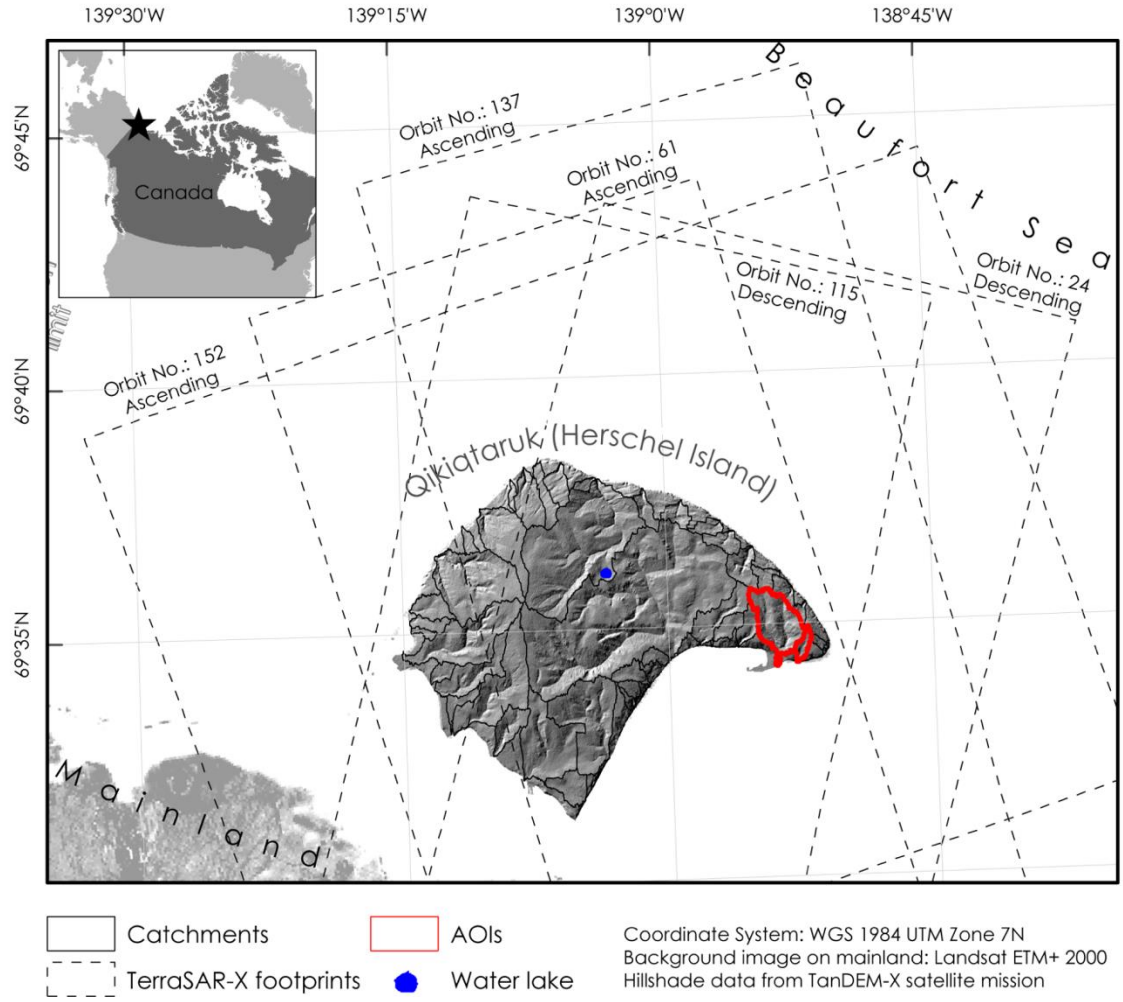

Figure 3-1: Location of Qikiqtaruk in the Southwestern Beaufort Sea Region and footprints of TerraSAR-X imagery.

Chapter 3 Study area

The vegetation of Qikiqtaruk belongs to the lowland tundra type and is dominated by graminoids and dwarf shrubs, with a relatively species-rich forb flora and a well-developed moss layer (Kennedy et al., 2001; Myers-smith et al., 2011; Smith et al., 1989). The sediments are unconsolidated and mostly fine-grained glacigenic material with marine origin (Blasco et al., 1990; Fritz et al., 2012). The thickness of the active layer generally ranges between 40 and 60 cm in summer, depending on topography (Burn and Zhang, 2009; Kokelj et al., 2002). Permafrost on Qikiqtaruk is continuous and can be extremely ice-rich with mean ice volumes ranging between 30 and 60 vol%, and up to values > 90 vol%, when underlain by massive ground ice beds (Couture and Pollard, 2017; Fritz et al., 2015; Hugues Lantuit et al., 2012b). While mean annual air temperatures have been stable in the Western Canadian Arctic between 1926 and 1970, a total increase of 2.7 °C was observed here between 1970 and 2005 (Burn and Zhang, 2009). The effect of this increase of temperature is also exhibited on Qikiqtaruk Island where a deepening of the active layer by 15 to 25 cm has been documented between 1985 and 2005 (Burn and Zhang, 2009).

Seasonal snow cover typically starts to develop in September and lasts until June. Most snow falls in autumn before sea ice forms and when the ocean still provides a source of liquid water (Burn and Zhang, 2009). During winter, strong winds from northwest or north-eastern directions affect the snow distribution. Because the tundra vegetation on elevated areas is sparse and trapping capacities are low, the strong winds blow much of the upland surfaces clear of snow and consequently large snow drifts develop in topographic depressions such as valleys and gullies (Burn, 2012). These snowdrifts can last through the summer, in particular when protected from melting by an insulating layer of plant detritus. This layer can develop during winter when the strong winds transport and deposit plant detritus together with snow. Ramage et al. (2018) identified 40 hydrologic catchments on Qikiqtaruk Island that drain into the surrounding ocean. Our study focuses on the catchments around the Ice Creek catchment in the south-eastern part of the island (Figure 3-1)

3.4 DATA AND METHODS

In order to create maps of snow cover extent (SCE) and fractional snow cover (FSC) we used dense time series of TSX as well as Landsat 8 imagery and in-situ time-lapse camera data. Our workflow is presented in Figure 3-2.

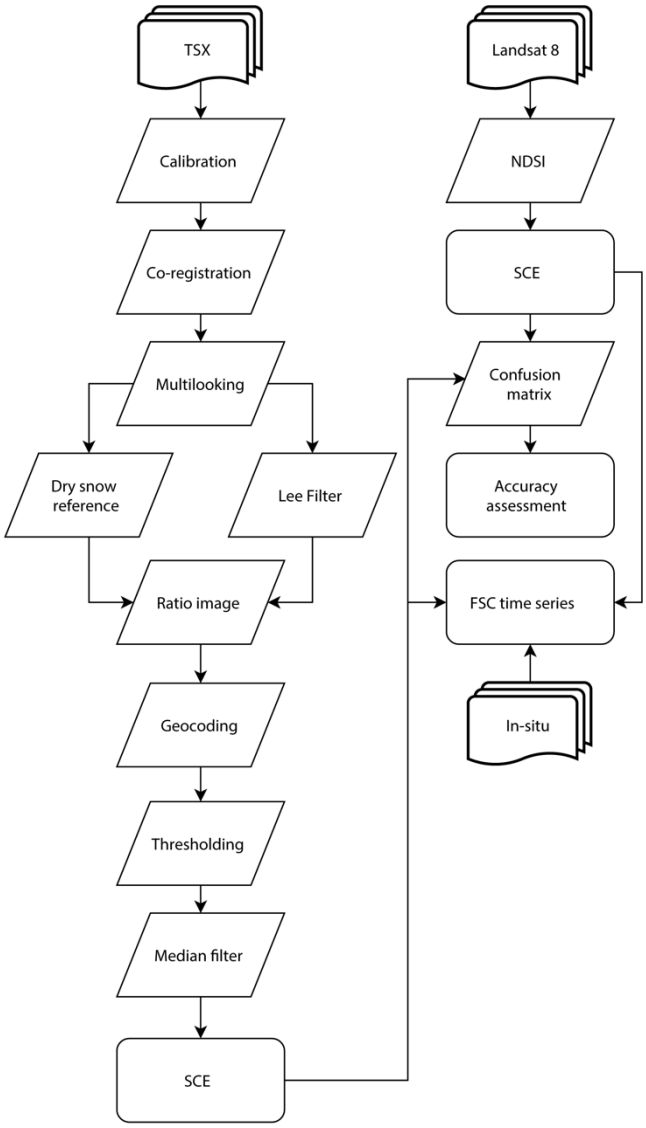

Figure 3-2: Data processing schematic for the optical Landsat 8 and TSX data. Layered objects represent input data, diamonds processing steps and rounded rectangles results. FSC=Fractional Snow Cover; NDSI=Normalized Difference Snow Index; SCE=Snow Cover Extent.

3.4.1 SAR SATELLITE DATA

We used dual cross-(VH/VV) and co-polarized (HH/VV) multi-orbit TSX time series with acquisition dates between April and July from 2015 to 2017. TSX uses a right looking active phased array antenna that operates at an X-Band centre frequency of 9.65 Ghz with an

orbital revisit time of 11 days. Using multi-orbit data from ascending and descending orbit headings allowed us to increase the revisit time to observe snowmelt in high temporal resolution. The incidence angles of the orbits at the image scene centre varied between 25° and 39° with varying pixel spacing between 1.9 to 2.8 m in range and 6.6 m in azimuth (Table 3-1). Though shadowing and layover can affect the quality of TSX data, the relief of Qikiqtaruk is low meaning the influence of layover and shadow is generally minimal inland. We masked out the coastal areas with the steep cliffs since they are not representing delineated catchments and could introduce errors of shadow and layover.

Table 3-1: Information on TSX orbits used in this study. RA = Range, AZ = Azimuth The incidence angle θ refers to the image scene centre.

	Acquisition time						
Orbit No.	UTC	Local time	Orbit heading	Incidence angle θ	Pixel spacing RA& AZ	Polarization	No. of winter scenes
24	16:08	9:08	Descending	31°	2.3 / 6.6	HH / VV	7
61	2:26	19:26	Ascending	32°	2.2 / 6.6	VV / VH	5
115	15:59	8:59	Descending	39°	1.9 / 6.6	VV / VH	4
137	2:35	19:35	Ascending	39°	1.9 / 6.6	HH / VV	2

3.4.2 Optical satellite data

We used all available cloud-free Landsat 8 imagery from 2015 to 2017 between the months of April and July. In total we used 20 Landsat 8 Operational Land Imager (OLI) acquisitions downloaded in processing Level-1 TP. We downloaded all acquisitions using the bulk download application from the USGS earth explorer service (https://earthexplorer.usgs.gov). The Landsat 8 OLI visible, near-infrared and shortwave infrared bands have a 30 m spatial resolution. We created quasi-true RGB composite imagery from every acquisition as visual reference and additionally used the green and short wave infrared bands for SCE generation (see section 3.4.5).

3.4.3 In-situ time-lapse camera data

Time-lapse cameras were set up in the framework of the Helmholtz Young Investigators Group "COPER" and the "ShrubTundra" research projects in the spring of 2016 and 2017 as part of ongoing hydrological and phenological monitoring on the island. Five cameras acquired images at an hourly resolution in a northward facing aspect with a landscape field of view. One camera was set up for monitoring a hydrological flume at the outlet of the western Ice Creek catchment and acquired imagery at a three hourly resolution from

April 24th to July 20th in 2016 (Camera ID: TL2). Four phenological cameras (PC) were set up for monitoring of phenology of vegetation communities at locations around the Ice Creek catchment (Camera IDs: PC2, PC3, PC5 and PC6). While camera TL2 represents snow dynamics of deeply incised valley locations, cameras PC2, PC3, PC5 and PC6 represent snow dynamics of upland tundra topography and vegetation of Qikiqtaruk. The time-lapse camera data was used for ground-based validation of TSX derived FSC time series. Photos that correspond to the TSX acquisition dates and time of day were used in the analysis when available, otherwise the closest date and time were chosen. The greatest difference between photos and TSX acquisition was a single day. The cameras were subject to disturbance by wildlife, active layer thaw and weather, and therefore were not always operational causing data gaps up to several days.

In addition, meteorological records from an automated weather station run by Environment Canada on Simpson Point on the south-eastern spit of the island (World Meteorological Organization ID: 715010) were used to assess the FSC time series in 2015, 2016, and 2017.

3.4.4 Snow Cover Extent from TerraSAR-X

To generate SCE maps from TSX we adapted the workflow suggested by Nagler and Rott (2000) and calculated ratio images of backscatter intensity - calibrated to radar brightness in sigma nought (σ0) as well as speckle-filtered, see details below - between an averaged dry snow reference image from TSX winter scenes (See Table 3-3) and melting snow scenes from spring/summer with the same orbital configuration. The reduced backscatter signal of melting snow is the basis for a threshold segmentation that efficiently differentiates between wet snow and dry snow or no snow.

The backscatter intensity of images acquired during the spring show notable differences between acquisitions caused by drifting sea ice and snowmelt that reduce the quality of co-registration when using cross-correlation. For a given acquisition orbit all images therefore were co-registered to sub-resolution accuracy with respect to a pre-selected master image using the highly accurate orbital information from TSX and ellipsoidal heights. In order to avoid early season effects of snowmelt with resulting high soil moisture variations and beginning vegetation dynamics, we chose mid-summer acquisitions (July) as the master images when environmental conditions had stabilized.

By applying 3x9 multilooking to the intensity images we address the speckle effect inherent to SAR imagery obtaining a roughly square pixel size of around 20m (Table 3-1). We further reduced the effect of speckle by applying a Lee filter with a window size 5x5 pixel (Lee 1983).

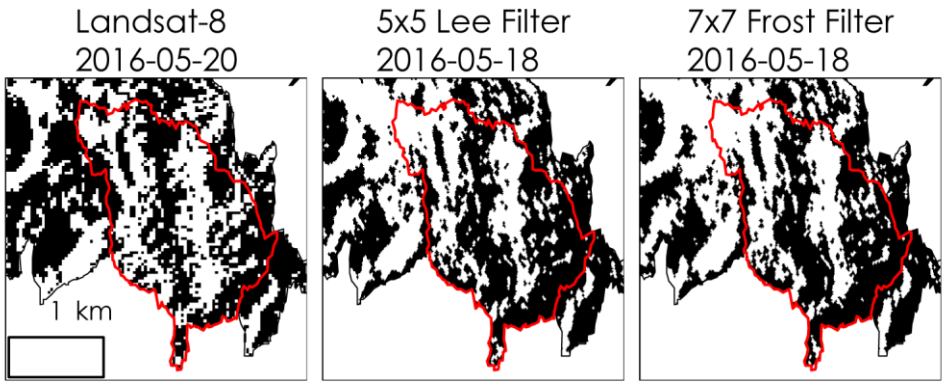

Figure 3-3: Comparison of filter methods for SCE generation. White pixels represent snow. The red line represents the Ice Creek catchment limit on the south-eastern part of Qikiqtaruk.

We tested the Lee (Lee, 1983) and Frost (Frost et al., 1982) filters to address the speckle effect within the intensity images for their performance for SCE generation. Figure 3-3 shows the optical reference data from Landsat 8 and the result from TSX with two day later acquisition date and differing filter techniques. The differences between the Frost and the Lee Filter were insignificant; however, the processing time for the moving window calculation of the Frost filter was much longer. We therefore decided to use the Lee Filter with a 5x5 window for all SCE generation, since it satisfactorily removes speckle related effects from the SCE maps.

We computed the σ0-ratios between the melting snow images and the dry snow reference separately for each polarization channel before transforming the ratio images to logarithmic scale (dB). We then geocoded the ratio images using the intermediate DEM product from the TanDEM-X mission with a spatial resolution of 12.5 meters and a vertical accuracy of 2m (Krieger et al., 2007). The DEM was created by DLR using several TerraSAR-X scenes from winter 2010 and 2011 and the Height Error Map provided with the DEM product states a mean error of 0.72 ± 0.2 m within the area of the hydrological catchments. We applied a threshold of 1 to all TSX ratio images, with values below 1 showing the presence of wet snow. We iteratively tested several thresholds and finally determined a threshold of 1 with the best performance of detecting snow and avoiding noise. We filtered the thresholding results using a median filter with a window size of 5x5 pixels.

3.4.5 Snow Cover Extent from Landsat 8

We applied the spectral band ratio of the Normalized Difference Snow Index (NDSI) to generate SCE maps from Landsat. The NDSI is a commonly applied ratio index for snow detection from optical sensor data (Hall et al., 2002) using the contrast in the visible green versus the shortwave infrared band reflectance. We applied the NDSI with OLI bands 3 and 6 and the threshold technique with NDSI > 0.4 to binary classify snow presence and absence with greater or less than 50% snow cover at pixel-level, respectively (Crawford et al., 2013).

3.4.6 Accuracy assessment of TerraSAR-X Snow Cover Extent

Confusion or error matrices are commonly used to assess the quality of classified spatial data from different data sources, at the same time not (Foody, 2002). In order to estimate the quality of TSX derived SCE we created confusion matrices between a TSX SCE and the corresponding Landsat 8 SCE. We chose corresponding Landsat 8 SCE with acquisition dates not further apart than ± 3 days from the TSX SCE. We used 5000 accuracy assessment points and for every pair, which were proportionally distributed between the classes of "snow" and "no snow" in a stratified random approach. We averaged the final results from 100 iterations of this accuracy assessment. The results include the Users, Producers and Overall accuracies as well as the Kappa index of agreement (k). These values give an indication of the reliability of the TSX maps, with Users indicating that TSX is detecting snow where Landsat 8 does not, Producers indicating that TSX is not detecting snow when Landsat 8 is, Overall is a weighted measure that indicates the general occurrence of errors. Finally k is an important parameter for comparison of categorical maps with only few classes like in the case of a snow / no snow binary classification. K shows the agreement between both maps and additionally compensates to some extent to chance agreement, with k = 0 means no agreement, k = 1 means total agreement and k < 0 showing more disagreement than a random assignment of classes between the TSX derived SCE map and the corresponding Landsat 8 SCE map.

3.4.7 Fractional Snow Cover time series analysis

We calculated the fractional wet snow cover (hereafter referred to as FSC) from the generated SCE maps in percent (%) for 1) all small catchments on the island and 2) for the entire island by merging all individual catchments into a single area. We resampled and aligned the TSX SCE to the 30 m spatial resolution of the Landsat 8 SCE. The footprints of

the TSX orbits 152, 137 and 24 do not cover the entire western part of the island. We calculated the fraction of snow pixels within a catchment for every SCE with regard to the total number of pixels within the catchments. We used the WGS UTM Zone 7N coordinate system for all map outputs. To validate the time series of TSX FSC, we analysed in-situ data from the time lapse cameras in and around the Ice Creek catchment (Table 3-4). For each time lapse image the snow cover within the field of view was estimated interactively by an independent visual interpretation of the photo by three different individuals. We then averaged the three estimations for every image acquisition. Additionally, for the cameras observing phenology in 2017 we averaged the estimations of the four available cameras per date in order to obtain a valid representation of the upland tundra type of the island.

3.5 Results

3.5.1 Evaluation of TSX Snow Cover Extent

The assessment of the TSX derived SCE from three polarization channels demonstrates the influence of polarization in X-Band on the application of monitoring SCE in an Arctic environment. All polarizations detected SCE patterns that were also reflected by Landsat 8 (Figure 3-4, Figure 3-5, Figure 3-10, Figure 3-11 and Figure 3-12).

Comparison of seven VH-, eight VV- and 15 HH-based TSX-derived SCE maps with paired optical SCE maps showed that the VH polarization channel performed best and most consistently in detecting snow cover during the snowmelt period (Table 3-2). We achieved the highest mean overall accuracy of 0.80 when using VH polarized images, compared to a mean overall accuracy of 0.71 and 0.66 for HH and VV polarized images, respectively. At the same time the variation of overall accuracy was highest in the VH polarization with 0.27 compared to 0.19 and 0.20 in the HH and VV channels. The mean kappa value was also highest in the VH channel with 0.21. The incidence angle and time difference between paired TSX and optical acquisitions did not show a clear effect on the overall accuracy. While the overall accuracy of the SCE maps from VH data generally showed a higher agreement later in the snowmelt season, the kappa index decreased significantly, except for the TSX acquisition from May 10th 2016. The other polarizations did not show a clear influence of time on the overall accuracy of SCE, but also showed a clear trend of decreased kappa index in the late season (Table 3-2).

Table 3-2: Confusion matrix results from the comparison of TerraSAR-X and Landsat 8 derived SCE for the three polarizations. U = Users accuracy, P = Producers accuracy, O = Overall accuracy, k= kappa index

TSX date	Polarization	Orbit	Incidence angle	Landsat Date	U	P	O	k
2015-05-15	HH	137	39	2015-05-16	0.78	0.68	0.68	0.36
2015-05-16	HH	152	25	2015-05-16	0.73	0.86	0.72	0.37
2015-05-26	HH	137	39	2015-05-25	0.95	0.91	0.87	0.20
2016-05-12	HH	137	39	2016-05-11	0.05	0.89	0.78	0.07
2016-06-28	HH	24	31	2016-06-28	1.00	0.78	0.78	0.00
2017-06-24	HH	152	25	2017-06-24	0.99	0.88	0.86	-0.01
2017-06-26	HH	24	31	2017-06-24	0.96	0.37	0.37	-0.03
2017-07-07	HH	24	31	2017-07-08	1.00	0.59	0.59	0.00
Mean					0.81	0.75	0.71	0.12
Standard deviation					0,32	0.32	0.19	0.17
2015-05-24	VH	115	39	2015-05-25	0.98	0.89	0.88	0.41
2015-06-23	VH	61	32	2015-06-26	1.00	0.98	0.98	0.12
2016-05-10	VH	115	39	2016-05-11	0.01	0.88	0.23	0.00
2016-05-18	VH	61	32	2016-05-20	0.86	0.68	0.74	0.49
2016-05-21	VH	115	39	2016-05-20	0.72	0.97	0.76	0.44
2016-07-12	VH	61	32	2016-07-14	1.00	0.98	0.98	0.01
2016-07-15	VH	115	39	2016-07-14	1.00	1.00	1.00	0.01
Mean					0.80	0.91	0.80	0.21
Standard deviation					0,36	0.11	0.27	0.22
2015-05-15	VV	137	39	2015-05-16	0.77	0.53	0.63	0.29
2015-05-16	VV	152	25	2015-05-16	0.72	0.85	0.71	0.36
2015-05-24	VV	115	39	2015-05-25	0.96	0.47	0.49	0.05
2015-05-26	VV	137	39	2015-05-25	0.95	0.88	0.84	0.19
2015-06-23	VV	61	32	2015-06-26	1.00	0.84	0.83	0.00
2016-05-10	VV	115	39	2016-05-11	0.02	0.89	0.32	0.01
2016-05-12	VV	137	39	2016-05-11	0.06	0.81	0.88	0.09

Continuation Table 3-2

TSX date	Polarization	Orbit	Incidence angle	Landsat Date	U	P	O	k
2016-05-18	VV	61	32	2016-05-20	0.81	0.55	0.65	0.32
2016-05-21	VV	115	39	2016-05-20	0.78	0.82	0.75	0.48
2016-06-28	VV	24	31	2016-06-28	1.00	0.58	0.58	0.00
2016-07-12	VV	61	32	2016-07-14	1.00	0.67	0.67	0.00
2016-07-15	VV	115	39	2016-07-14	1.00	0.92	0.92	0.00
2017-06-24	VV	152	25	2017-06-24	0.98	0.83	0.82	-0.01
2017-06-26	VV	24	31	2017-06-24	0.96	0.28	0.28	-0.02
2017-07-07	VV	24	31	2017-07-08	1.00	0.47	0.47	0.00
Mean					0.80	0.69	0.66	0.12
Standard deviation					0.32	0.32	0.20	0.20

The comparison of TSX derived VH polarized SCE maps from orbits 61 and 115 and optical derived SCE maps highlight the spatial patterns of agreement between the two data sources (Figure 3-4 and Figure 3-5). Figure 3-4 represents a comparison of VH and VV polarized TSX SCE from orbit 61 and the corresponding Landsat 8 SCE at three different stages of snowmelt in 2015 and 2016. The Landsat 8 SCE map from 26th of June 2015 shows only a few remaining and small snow patches in low-lying valleys. On the 23rd of June 2015 the TSX in VH shows elongated single patches of snow distributed sparsely over the island while the VV channel detects larger connected areas of snow cover except in the central part of the island. During peak snowmelt the TSX derived SCE from the 18th of May 2016 showed denser snow cover than the Landsat 8 SCE from the 20th of May 2016. In particular, TSX detected denser snow cover on the higher and flat terrain in the centre of the island and northwest of the Ice Creek catchment (Figure 3-4, second row). The later stage snowmelt maps also show good agreement between TSX and optically derived products (Figure 3-4, third row). The general pattern of overestimation of VV is evident in all VV polarized SCE maps in Figure 3-4**Fehler! Verweisquelle konnte nicht gefunden werden.** and also in Figure 3-5. The Kappa Index is highest in peak snowmelt, indicating that the observed agreements are best here, compared to the late stages of snowmelt.

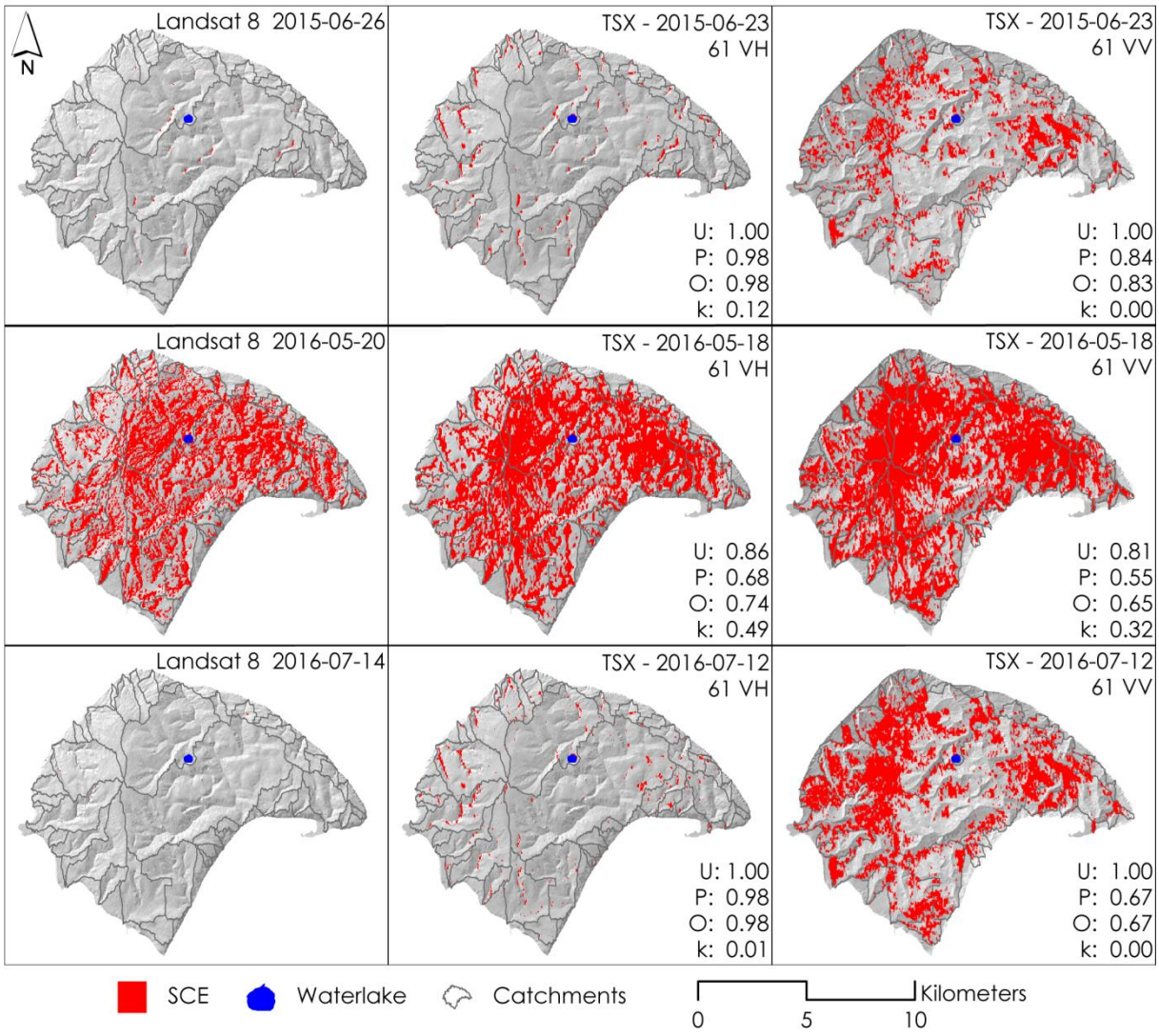

Figure 3-4: Comparison of Landsat 8 SCE (left panels) and corresponding TSX SCE derived from the VH (middle panels) and VV (right panels) polarized channels of orbit 61 from three dates in 2015 (first row) and 2016 (second and third row). Also shown are the results of the accuracy assessment, U = Users accuracy, P = Producers accuracy, O = Overall accuracy, k = Kappa Index.

In Figure 3-5 the May 25 2015 Landsat 8 SCE map shows several elongated snow banks remaining on the island. The corresponding TSX result from a day earlier shows the same pattern in VH but additionally detects what appear to be wet snow patches with a more scattered distribution on the western part of the island. The VV channel again shows strong overestimation of SCE almost in all areas of the island. The early melt, as shown in the second row of Figure 3-5 is not captured well by TSX in both polarizations, while the overall accuracy is considerably higher in the late snowmelt season of 2016. Again the Kappa Index indicates best classification results during peak snowmelt.

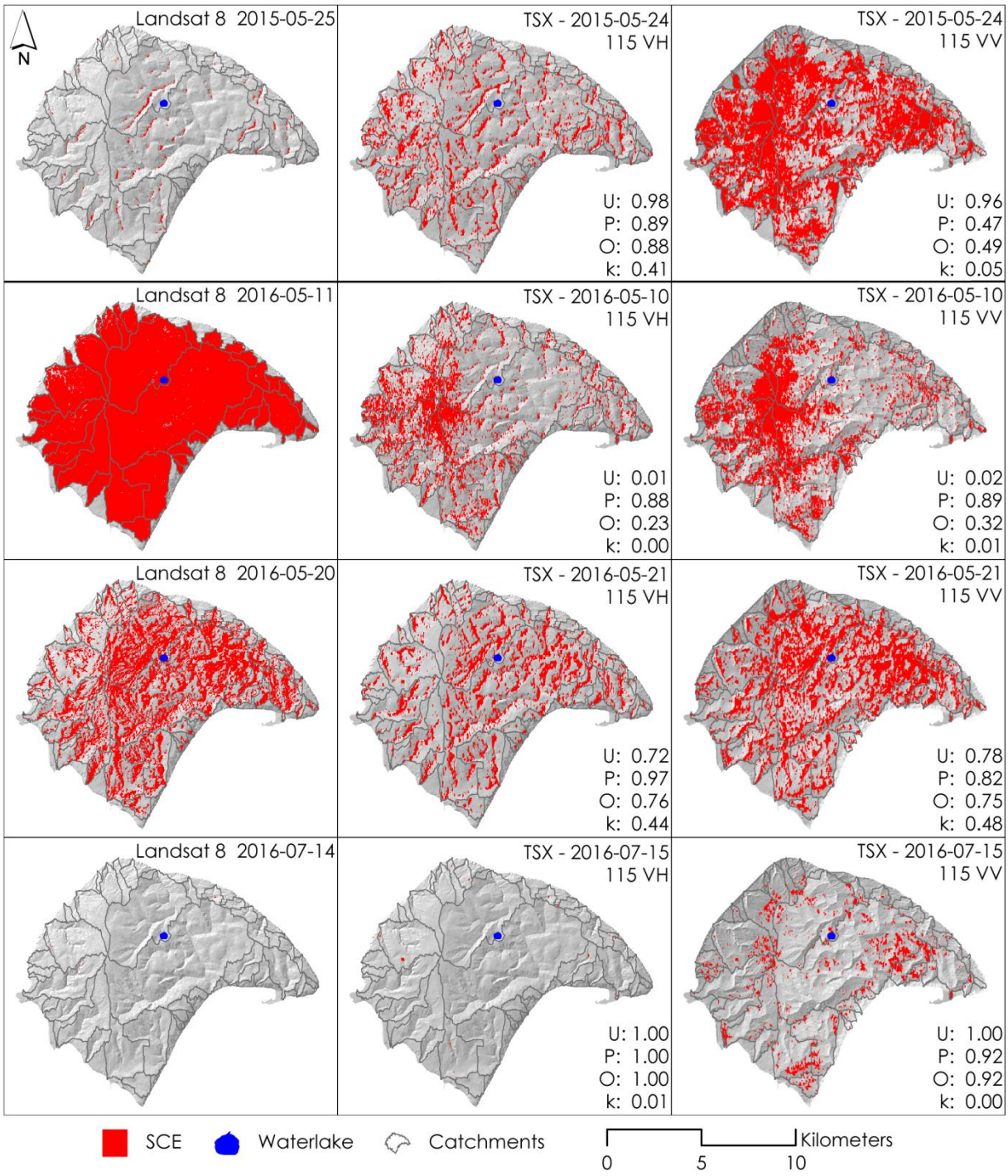

Figure 3-5: Comparison of Landsat 8 SCE (left panels) and corresponding TSX SCE derived from the VH (middle panels) and VV (right panels) polarized channels of orbit 115 from four dates in 2015 (first row) and 2016 (second, third and fourth row). Also shown are the results of the accuracy assessment, U = Users accuracy, P = Producers accuracy, O = Overall accuracy, k = Kappa Index.

3.5.2 Time series of Fractional Snow Cover in all catchments

Building on the results of the accuracy assessment, all orbits with VH polarization were chosen to examine the snowmelt dynamics in 2015, 2016, and 2017. Figure 3-6 shows a time series of FSC products calculated for the unified catchment area from Landsat 8 and VH polarized TSX-derived SCE as well as the corresponding minimum, mean and maximum daily air temperatures. In all three years, the TSX derived FSC showed good agreement with the optical Landsat 8 FSC and both data sources show a typical snowmelt pattern with increasing air temperatures (Figure 3-7). The agreement between TSX and Landsat 8 FSC data was lowest early in the snowmelt period (April to early May). Due to the independence of TSX to atmospheric conditions and cloud cover, the temporal resolution of TSX was higher in all years particularly in the phase of rapid snow cover decline from mid-May to June.

In 2015, the TSX FSC was below 50 % in beginning of May and increased to 75 % in mid-May when there was no Landsat 8 acquisition. Maximum air temperatures were above 0°C early in mid to late-April before falling below around -5°C for about 2 weeks, which corresponds to low snow cover observed by TSX in early May. Both TSX datasets show an increase in FSC followed by a sharp drop to around 10% FSC at the beginning of June followed by a slow gradual decrease of FSC to 0% in July which is visible in all datasets. In 2016, both TSX orbits showed nearly 100% FSC within the catchment areas in the beginning of May. TSX-derived FSC calculated from orbit 61 then showed a strong gradual decrease to around 25% at the end of May while FSC calculated from orbit 115 showed a sharp drop to around 25% in early May. The FSC derived from Landsat 8 imagery shows a sharp drop from 100% FSC in early to about 30% in mid-May. In the late stage of snowmelt, all datasets show FSC of approximately 5%. The air temperature in 2016 was stable around 0°C for almost the entire month of May, but shows two peaks in early and mid-May that corresponded to sharp drops in snow cover in Landsat 8 and TSX orbit 61.

Air temperatures in 2017 showed a gradual increase to 0°C by mid-May and a corresponding gradual decrease in TSX-derived FSC. There was an approximately two month gap in successful Landsat 8 acquisitions in 2017.

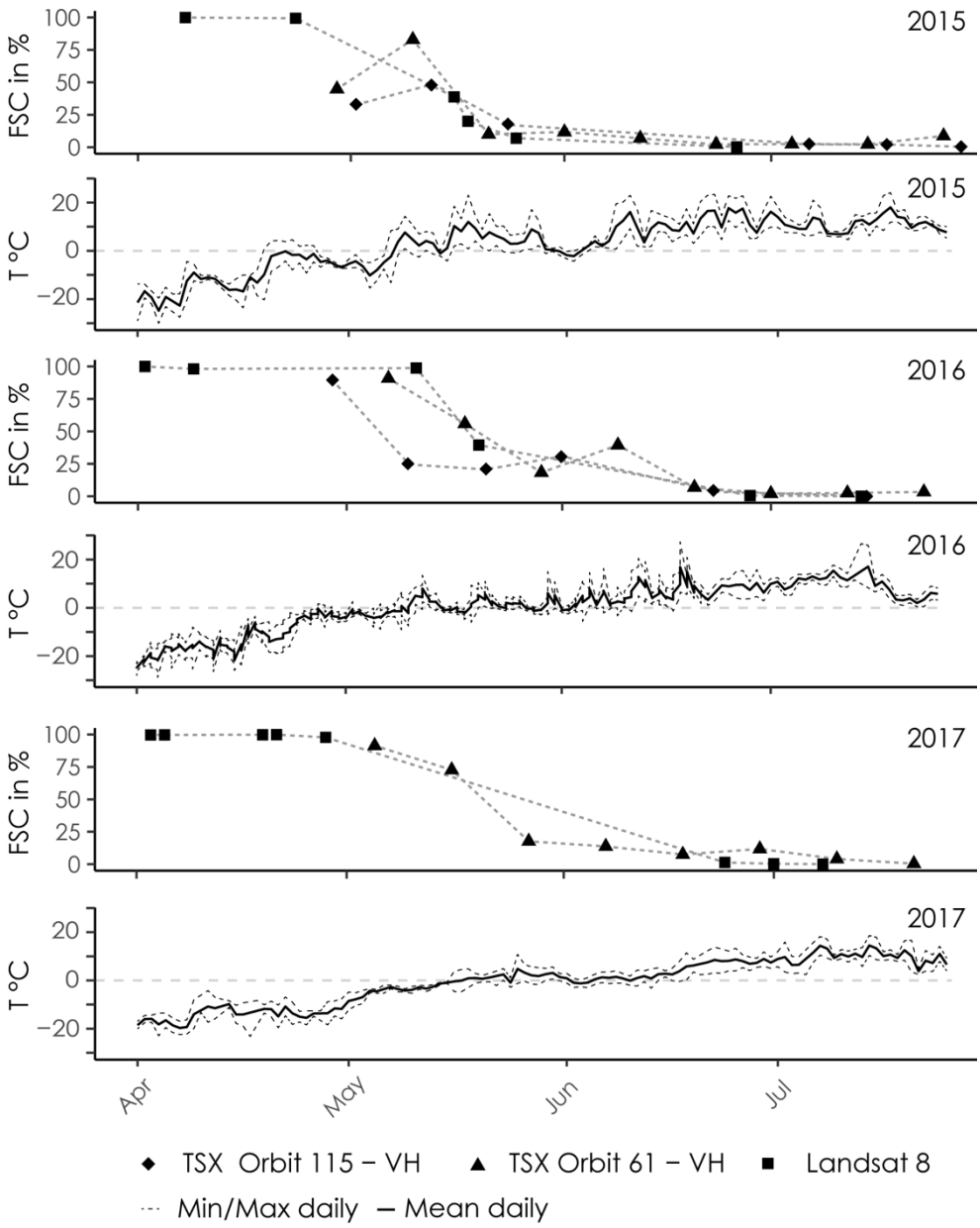

Figure 3-6: Time series of fractional snow cover (FSC) extent and air temperature of Qikiqtaruk from Landsat 8 and VH polarized TSX data from the orbits 115 and 61 for the years 2015, 2016, and 2017.

3.5.3 Time series of Fractional Snow Cover in small catchments

Figure 3-7 shows the time series of fractional snow cover in the Ice Creek catchment in 2016 as captured from different data sources. The six available acquisitions from Landsat 8 show the beginning snowmelt after the 9th of May with a sharp drop to about 50% within a week and a more gradual retreat of the snow cover to about 5% by the 27th of June. The SCE from orbit 61 recorded wet snow on the 9th of May at about 85% and showed a reduction of FSC at a relatively constant rate to about 20% in three weeks by the end of June.

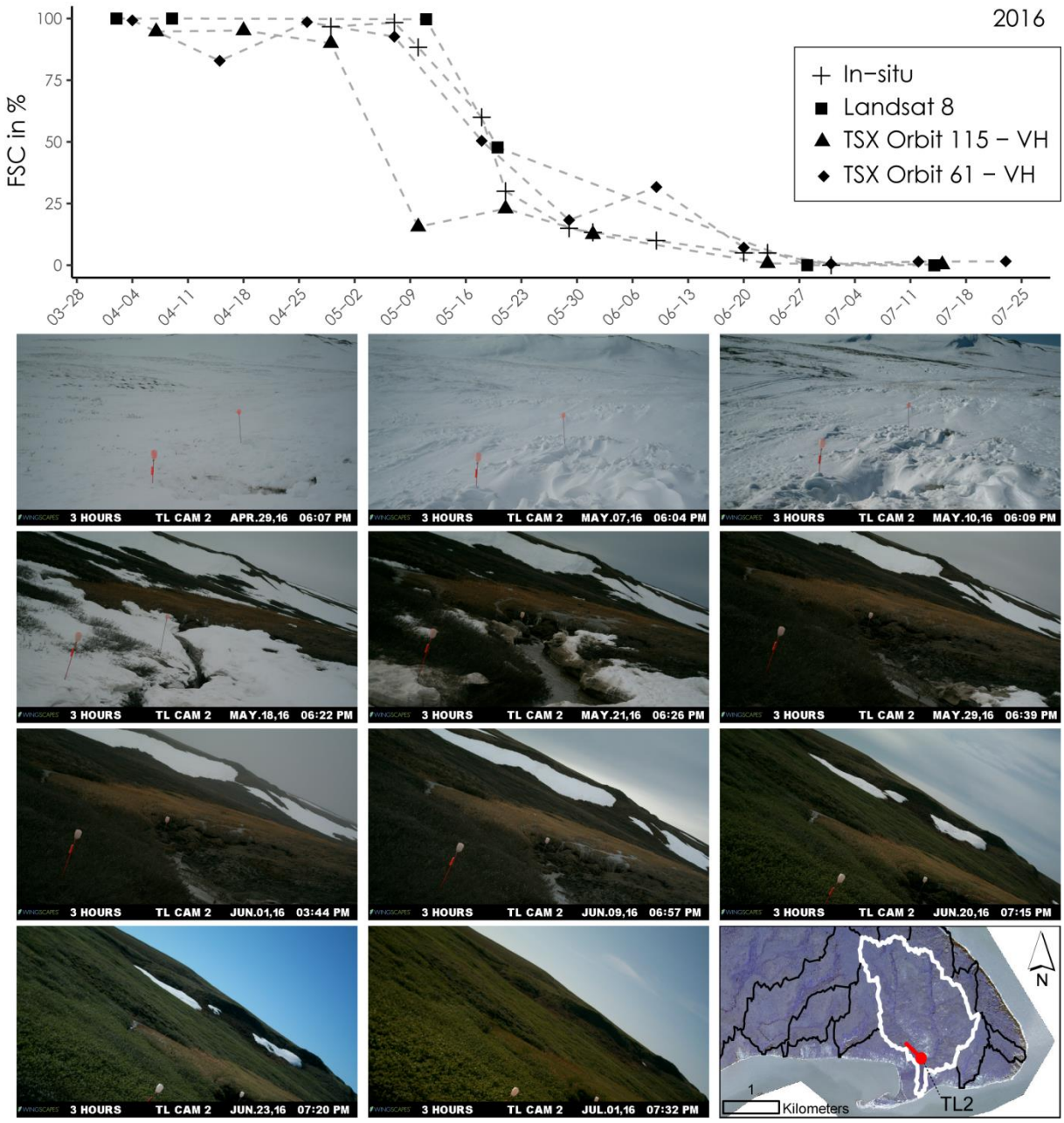

Figure 3-7: Top graph: Fractional snow cover from time lapse (in-situ), Landsat 8 and TerraSAR-X (TSX) imagery in 2016 in the Ice Creek catchment (white outline in the map inlet on lower right). Dates on the x-axis show month-day. Time-lapse imagery is from Camera TL2 and is located in the lower Ice Creek. It's location (red dot) and viewing direction (red line) is indicated in the inset map on the lower right. Please note that the camera was unstable and moved between images because of ground thaw. Please note that the acquisition time of orbit 115 is in the morning, potentially affected by refreezing snow layers in early May.

An increase of FSC to 30% is recorded with the next acquisition in early June, followed by a reduction to about 10% around the 20th of June followed by a slow decrease to 5% or less by the end of June. The SCE from orbit 115 shows a rapid decrease in FSC from around 80% to about 20% in a little more than a week between 29th of April and the 9th of May.

This coincides with the presented results in Figure 3-6 for the entire island and below 0°C minimum air temperatures and the morning acquisition of this orbit. A slight increase to around 25% FSC is followed by a gradual decrease to less than 5% by the end of June. The in-situ imagery, collected in the lower end of the ice creek valley within steeper valley topography, show snowmelt beginning around the 9th of May and a decrease of FSC to about 60% around 17th of May in less than two weeks. After that FSC decreases at a faster rate to about 25% in only a few days before a more gradual melt reduces FSC to 0% on July 1st.

Figure 3-8 shows the FSC time series for the year 2017 of a small catchment southeast of Ice Creek as observed from in-situ, Landsat 8 and TSX data. The Landsat 8 derived FSC is mainly from before or after the main snowmelt period. Therefore, the decrease in FSC appears gradual between 1st of May and the middle of June from 100% to below 25. The TSX derived SCE from orbit 61 detects wet snow cover in early June with an FSC of approximately 60% and decreases until end of May gradually to about 20%. Until end of June the FSC further decreases at a lower speed to about 5% and to 0% until end of July. The in-situ data, collected from time lapse cameras that represent only upland areas of the watersheds show a rapid decrease in FSC from 80% to 20% in the first two weeks of May. At the end of May FSC is below 5% and by early June no snow is detected.

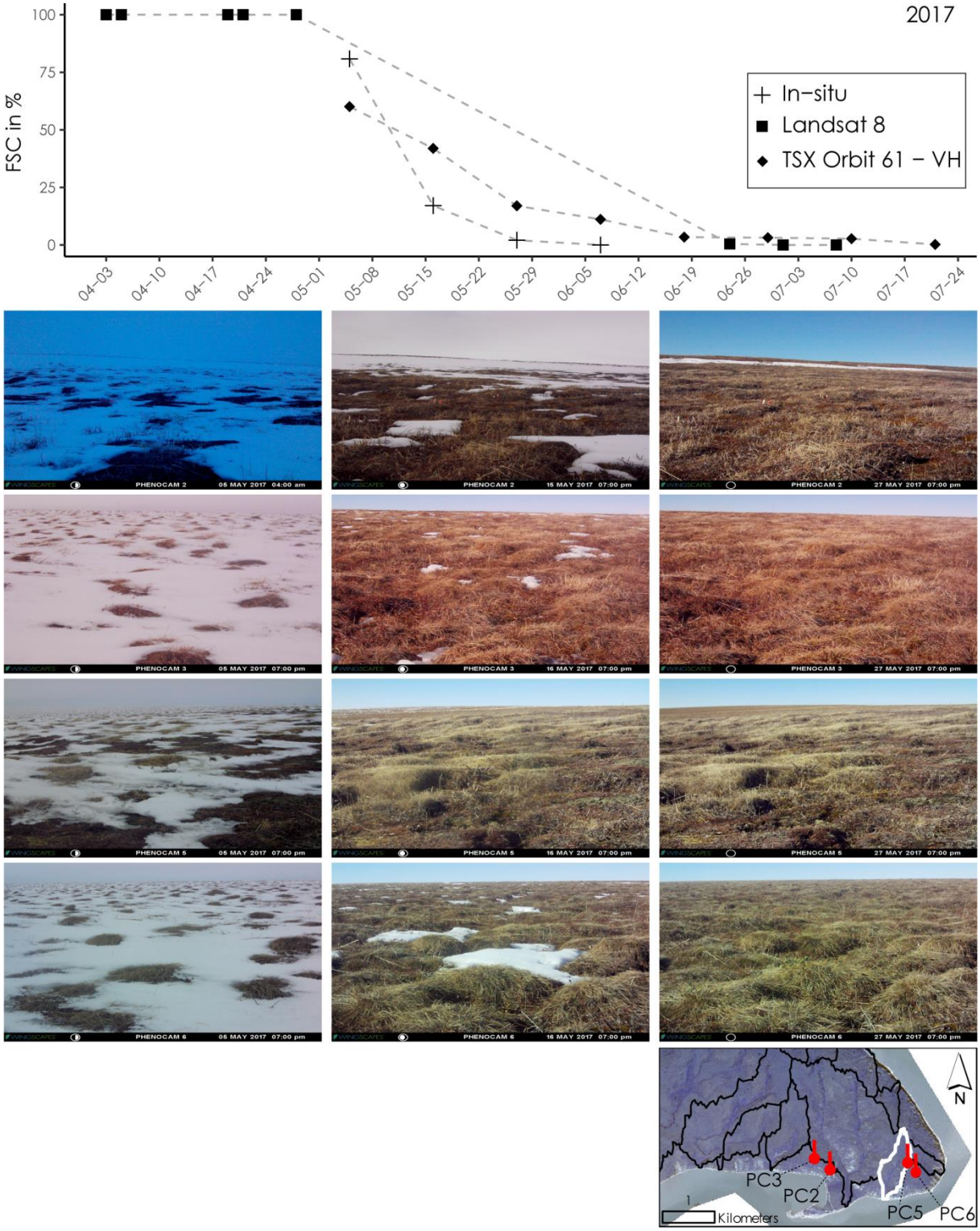

Figure 3-8: Top graph: Fractional snow cover from time lapse (in-situ), Landsat 8 (L8) and TerraSAR-X (TSX) imagery in 2017 in a selected small Arctic catchment (white shape in the map inlet on lower right). Dates on the x-axis show month-day. Time-lapse imagery is from the cameras PC2 (first row) and PC3 (second row), PC5 (third row) and PC6 (fourth row), all representing flat upland tundra locations with low vegetation and tussocks. Dates of the images are 5th of May (first column), 15/16th May (second column) and 27th of May (third column). Camera locations (red dots) and viewing directions (red lines) are shown in the inset map on the lower right.

3.6 DISCUSSION

3.6.1 SPATIOTEMPORAL MONITORING OF SNOWMELT DYNAMICS USING TSX

The high agreement between TSX and Landsat 8 derived SCE products supports that X-Band SAR data is a complementary gap filling data source for detailed spatiotemporal monitoring of snowmelt dynamics at both the landscape and small Arctic catchment scale. Overall, the cross polarized VH channel performed best in detecting wet SCE, particularly in the later stages of snowmelt when only snowbanks remained in protected areas. The better performance in the late season is likely due to the high water content in the snow pack at this stage of melt. TSX SCE from VH polarization also consistently detected snow patches later in the season when Landsat 8 did not detect snow anymore. This indicates that while the contribution of the very low backscatter in wet snow prevails within a pixel late in the season in the SAR system, the optical snow detection capabilities decrease with lower snow albedo later in the season. This shows an advantage of a SAR system with high spatial resolution over an optical system with high resolution for mapping of late lying snow patches that are often located in steeper topographic areas and create unique abiotic and biotic conditions (Green and Pickering, 2009). Nagler et al. (2016) previously showed that cross-polarized VH data in C-Band discriminates wet snow cover well, even on steep topography with limited dependence on incidence angle. Our results suggest that VH polarized X-Band data can be used to identify and monitor location and duration of late lying snow patches providing important information on changing thermal regimes and moisture conditions.

The TSX data provides a significantly higher temporal resolution than that available with Landsat 8 data alone revealing the rapid advancement of snowmelt shortly following snowmelt onset. This provides a better temporal picture of snowmelt dynamics than what can be derived from optical data which, due to cloud cover and subsequent data gaps, generally indicate only the onset and end of snowmelt. A more complete picture of snow cover and snowmelt timing provides an opportunity to understand better the impacts on hydrology, vegetation, active layer and permafrost thermal regimes.

At the catchment scale two different snowmelt dynamics were observed simultaneously with in-situ and TSX data. In a representative area of the Ice Creek catchment featuring strong topography and long lasting snow patches, TSX data showed high correspondence to fractional snow cover estimates using time lapse cameras (Figure 3-7). Both datasets in

this catchment type with strong topography showed a sharp drop of snowmelt followed by lower rate snowmelt when only the snowbanks remained. When selecting a catchment type with less expressed topography the FSC time series from TSX also corresponded to time-lapse imagery from upland tundra type with a rapid snowmelt pattern (Figure 3-8). However, snow patches were also present in the upland type class and prolonged the FSC signal.

On June 9th 2016, the time lapse imagery within the lower Ice Creek catchment showed dense fog for nine hours with no traces of snow on the ground after the fog lifted. The TSX SCE from that date (Figure 3-9) suggests that new snow cover developed in the upper catchment of the ice creek at higher elevation above the time lapse camera location. This highlights the ability of TSX to capture potentially also short lived snowfall events. Short term freezing and snowfall events in the spring time can negatively impact early vegetation development and greatly impact hydrological discharge of small Arctic catchments (Hinzman et al., 1996; Inouye, 2008).

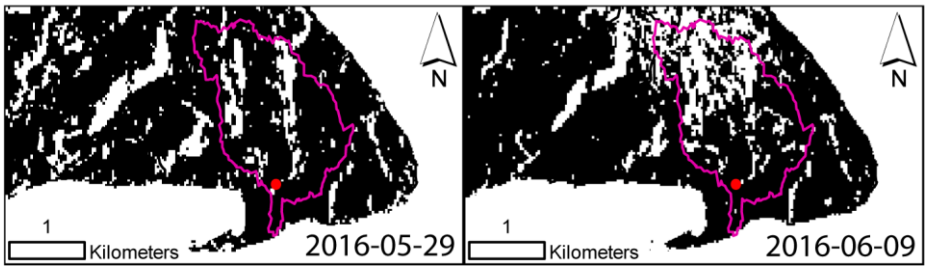

Figure 3-9: SCE from TerraSAR-X VH from the 29th of April 2016 (left) and from the 9th of May 2016 (right) for the Ice Creek catchment and surroundings. The red dot shows the position of the time lapse camera

3.6.2 Technical considerations for using TSX for wet snow detection

While our method improves the temporal resolution of snowmelt patterns, it faces potential limitations in low Arctic tundra environments. In the later phase of snowmelt, the HH and VV TSX-derived FSC were highly variable compared to the Landsat 8 derived FSC. This was also reflected in the very low kappa values from the accuracy assessment in all polarizations. The observed variability indicates that both channels react to other surface features. Nagler et al. (2016) also report lower accuracies of VV compared to the VH channel in C-Band, an effect likely connected to low local incidence angles. In our study the strong overestimations in VV are also likely influenced by local topography as the areas of false snow detection are predominantly on the flat tundra uplands on the western part of the island. These flat upland areas are likely the first to melt out

highlighting the sensitivity of VV to non-snow surface properties. Limitations in wet snow detection with the VV-polarized X-Band channel has been shown previously with false detection of wet snow in areas of water and (water saturated) bare ground (Mora et al., 2017). Additionally, while all polarizations will react to attenuation of the microwave signal in wet snow the cross polarized VH probably also reacts to a shift from volume scatter in dry snow to surface scatter on wet snow. This might increase the capability of VH to distinguish the active melt with liquid water concentrated at the snow surface from liquid water co-existing with the snow pack in vegetation or bare soils.

In addition to bare ground and water, previous research has also demonstrated the sensitivity of TSX (VV/HH polarized) data to the presence of Arctic shrubs and vegetation communities in summer (Ullmann et al., 2014) as well as in winter under a dry snow cover (Duguay et al., 2015). Under both conditions backscatter is expected to increase with higher shrub density because the fraction of volume scattering increases with taller vegetation. In the case of shrubs that protrude through the snow backscatter could increase through higher volume scatter and decrease the drop of backscatter between dry snow and wet snow images. As a consequence the algorithm would detect no snow even though snow is still present between and underneath the shrubs.

Previous research has shown that refreezing of the surface layer can increase the backscatter signal because of the change in dielectric properties of the frozen layer (Dana Floricioiu and Rott, 2001; Reber et al., 1987). Particularly the X-band can be sensitive to refreezing snow layers because of its short wavelength and minimal penetration through the frozen layer (Dana Floricioiu and Rott, 2001; Nagler et al., 2016). In this context the observed deviations between the 2015 as well as 2016 data from the 115 and 61 orbits in late April and early May most likely result from the difference in acquisition timing. Orbit 115 acquisitions are taking in the morning local time and 61 in the afternoon (see Table 3-1). Diurnal variations and resulting freeze thaw cycles are typical for the snowmelt period in the Arctic (Bartsch et al., 2007) with typical duration of periods with diurnal freeze thaw cycling in this region being up to two weeks (Bartsch and Annett, 2010). The freezing snow layers can drastically lower the detection of SCE (see Figure 3-5, row 2) and therefore the derived FSC product if the acquisition time is during the minimum temperatures of the day (Figure 3-7).

Although refreezing and presumably shrub vegetation can introduce some limitations for accurate mapping of wet snow with TSX, we were able to show that our 30 m aggregated

TSX SCE product added valuable information to the characterization of three snowmelt periods in small Arctic catchments. In combination with optical data from Landsat 8 a complete picture of snowmelt can be drawn, including short term snow dynamics. The potential of full spatial resolution TSX in combination with an optimized speckle filter for SCE generation would open up more applications for fine scale monitoring of the impact of snowmelt dynamics on ecosystem functioning in heterogeneous Arctic tundra environments.

It is important to emphasize that the TSX product is delivering a wet snow product in contrast to the optical data that do not differentiate between dry and wet snow. This can be drawn as a disadvantage when one is trying to draw a complete picture of snowmelt, because solely using TSX would not allow capturing the entire snow cover (dry or wet) at the onset of snowmelt. On the other hand the wet snow can show at what locations the snow is changing from dry to snow, information that is not captured by the optical sensors. The combination of different polarization channels of one acquisition in one product like proposed in Nagler et al. (2016) for VH/VV C-Band was not a suitable option in this study, since the VV channel did not add additional information content and furthermore showed strong deviations from the Landsat 8 based reference imagery.

3.7 Conclusions

The results of this study highlight the potential of TerraSAR-X X-Band to improve and complement existing optical data based snow cover products by increasing the temporal resolution of snow cover measurements. The VH polarization channel performed best when compared to Landsat 8 imagery, in particular at peak stages of snowmelt in mid-May. The VH polarization showed an advantage by detecting snow patches later in the season when Landsat 8 did not due to the lower reflectance of old snow. Differences in the incidence angle did not seem to have a strong effect on the accuracy of the SCE, although local topography and resulting incidence angle likely led to false snow detection in the co-polarized channels. The TSX data provides a significantly higher temporal resolution than that available with Landsat 8 data alone. This provides a much more complete temporal picture of snowmelt dynamics than the optical data which, due to data gaps as a result of cloud cover, generally indicates only the onset and end of snowmelt. However, acquisition timing needs to be considered due to diurnal temperature variations and resulting freezing snow layers that can strongly affect the capability of TSX to detect wet snow. Using both, in-situ time lapse camera data and TSX imagery we could show that

depending on catchment topography different temporal patterns of snowmelt exist. Overall, we conclude that a multi-source approach using conventional optical data in combination with high spatiotemporal resolution SAR in X-Band and in-situ time lapse camera data is very well suited to study rapid snowmelt in small Arctic catchments.

3.8 Acknowledgements

The authors want to thank the German Helmholtz Alliance Earth System Dynamics (EDA) for funding of this project and access to the TSX datasets. Samuel Stettner and Hugues Lantuit were additionally supported through HGF COPER, Annett Bartsch through the European Space Agency project DUE GlobPermafrost (Contract Number 4000116196/15/I-NB) and Birgit Heim through the Helmholtz program for Regional Climate Change REKLIM. The authors thank Isla Myers-Smith and Team Shrub setting up and sharing the data of the phenology time-lapse cameras, funding for this research was provided by NERC through the ShrubTundra (NE/M016323/1) standard grant. We thank George Tanski (AWI Potsdam), Jan Kahl (AWI Potsdam), Samuel McLeod (Herschel Ranger) and Edward McLeod (Herschel Ranger) for setting up the time lapse camera in spring 2016 possible. The authors thank Mike Kubanski (SARlab Vancouver) for his help with the code. The authors want to the Rangers of Herschel Island and the Aurora Research Institute for making the field work in this remote area possible. We thank Nicholas Coops and the IRSS lab at University of British Columbia for providing an excellent working environment during the processing of the optical satellite imagery for this work.

3.9 APPENDIX

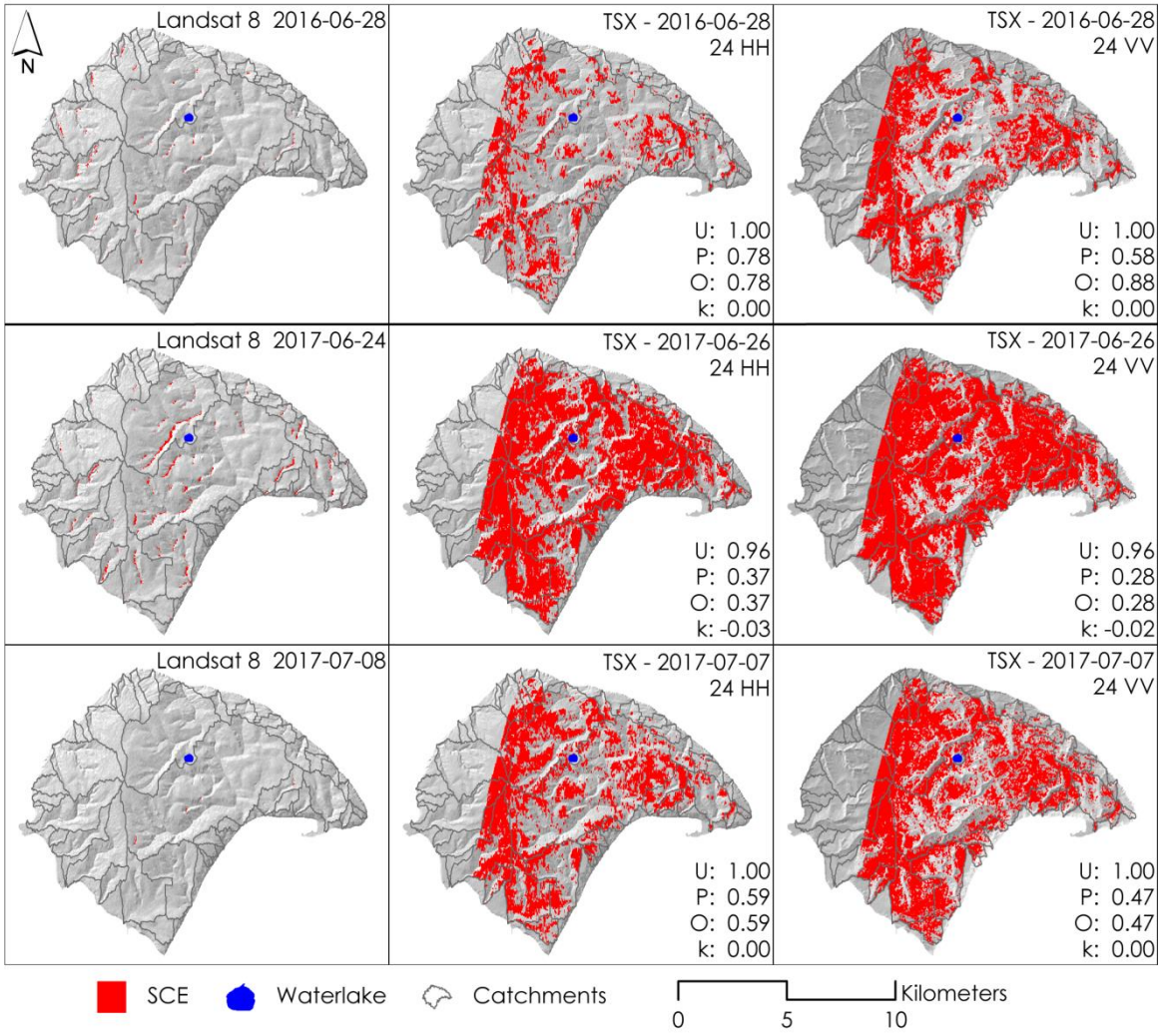

Figure 3-10: Comparison of Landsat 8 SCE (left panels) and corresponding TSX SCE derived from the HH (centre panels) and VV (left panels) polarized channels of orbit 24 with results of the accuracy assessment.

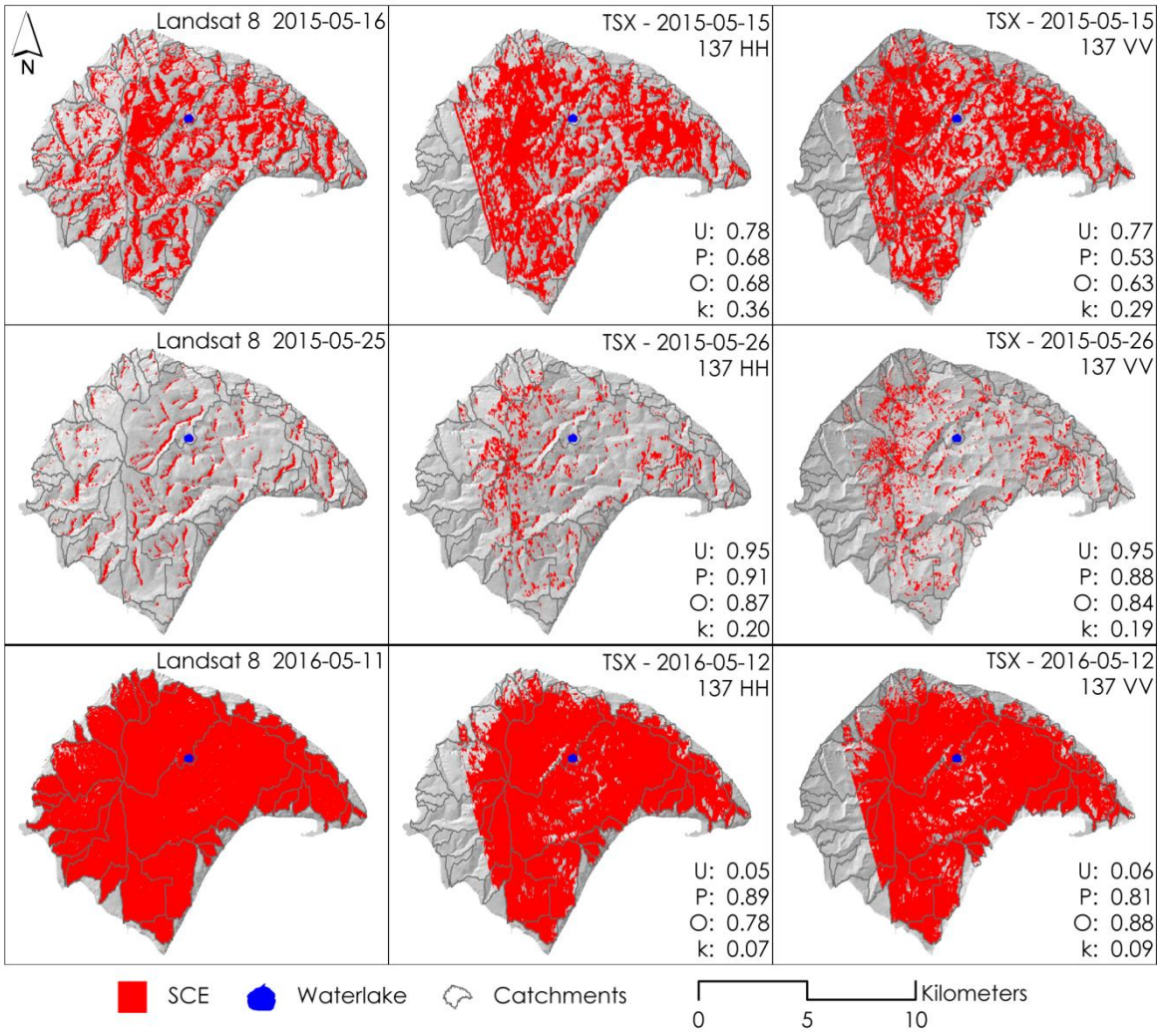

Figure 3-11: Comparison of Landsat 8 SCE (left panels) and corresponding TSX SCE derived from the HH (centre panels) and VV (left panels) polarized channels of orbit 137 with results of the accuracy assessment.

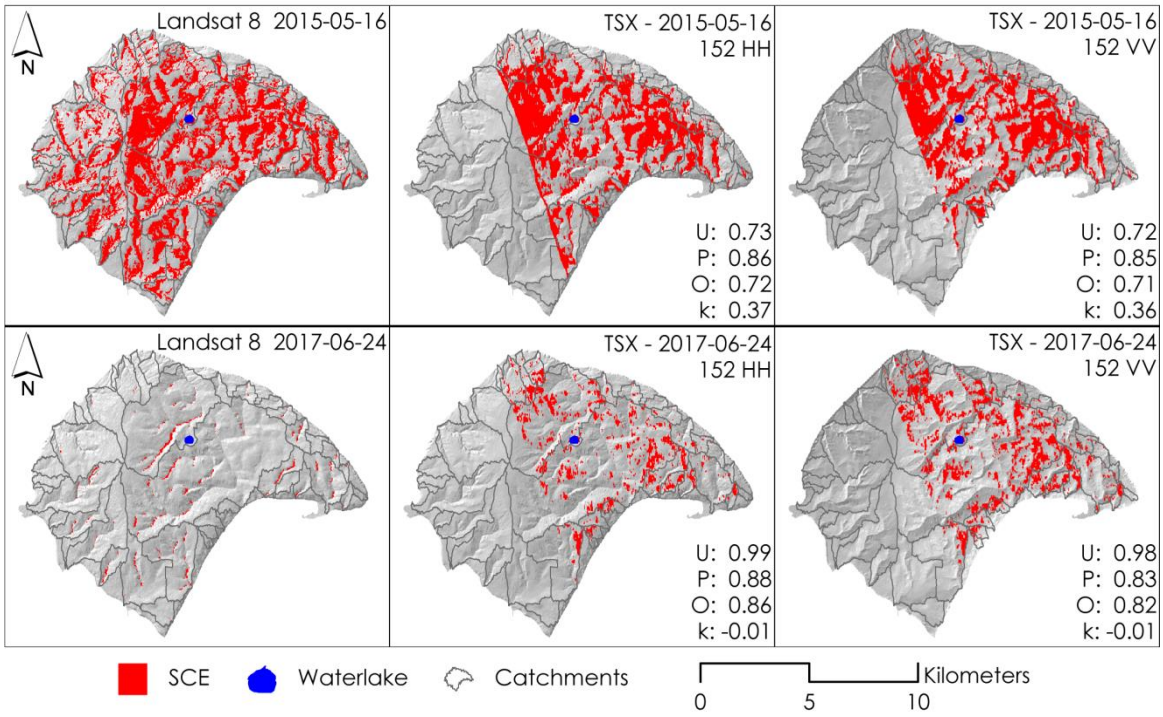

Figure 3-12: Comparison of Landsat 8 SCE (left panels) and corresponding TSX SCE derived from the HH (centre panels) and VV (left panels) polarized channels of orbit 152 with results of the accuracy assessment.

Table 3-3: List of TSX scenes used for the averaged dry snow reference.

Orbit 115	**Orbit 24**	**Orbit 61**	**Orbit 152**	**Orbit 137**
2015-02-03	2015-02-08	2015-02-11	2015-02-06	2015-02-05
2016-04-07	2015-04-15	2015-04-07	2015-04-02	2016-04-20
2016-04-18	2015-04-26	2016-04-04	2015-04-13	
2017-04-05	2016-04-01	2016-04-15	2015-04-24	
	2016-04-23	2016-04-26	2016-04-10	
	2017-04-10		2016-04-21	
	2017-04-21		2017-04-08	
			2017-04-19	

Chapter 3 Appendix

Table 3-4: Fractional snow cover from visual estimations of in-situ time lapse imagery. Camera TL2 acquired imagery at a three hourly resolution form April 24th to July 20th in 2016. Camera PC2 acquired imagery at a three hourly resolution form April 24th to July 20th in 2016.

Fractional snow cover (FSC)					
Date	**Estimation 1**	**Estimation 2**	**Estimation 3**	**Average**	**Camera ID**
2016-04-29	95	100	95	97	TL2
2016-05-07	95	100	100	98	TL2
2016-05-10	90	90	85	88	TL2
2016-05-18	70	50	60	60	TL2
2016-05-21	30	15	45	30	TL2
2016-05-29	15	10	20	15	TL2
2016-06-01	10	10	20	13	TL2
2016-06-09	10	10	10	10	TL2
2016-06-20	5	5	5	5	TL2
2016-06-23	5	5	5	5	TL2
2016-07-01	0	0	0	0	TL2
2017-05-05	80	90	70	80	PC2
2017-05-05	80	90	90	87	PC3
2017-05-05	75	90	60	75	PC5
2017-05-05	75	90	80	82	PC6
Average				81	

Table continues on the next page

Continuation Table 3-4

Fractional snow cover (FSC)					
Date	**Estimation 1**	**Estimation 2**	**Estimation 3**	**Average**	**Camera ID**
2017-05-15	50	50	30	43	PC2
2017-05-15	10	5	10	8	PC3
2017-05-16	5	5	5	5	PC5
2017-05-16	15	5	15	12	PC6
Average				17	
2017-05-27	10	5	10	8	PC2
2017-05-27	0	0	0	0	PC3
2017-05-27	0	0	0	0	PC5
2017-05-27	0	0	0	0	PC6
Average				2	
2017-06-07	0	0	0	0	PC2
2017-06-07	0	0	0	0	PC3
Average				0	

Chapter 4

4 Relationships between X-Band SAR and vegetation phenology in a low Arctic ecosystem

4.1 Abstract

Applications of synthetic aperture radar (SAR) in Arctic tundra ecosystems have increased recently with concurrent increases in high spatial resolution SAR satellites such as TerraSAR-X, RADARSAT-2 and Sentinel-1. The independence of SAR systems to cloud cover and refined acquisition strategies in Polar Regions have resulted in dense time-series. The application of these time-series to vegetation phenology, i.e. the emergence, growth, reproduction and senescence of vegetation, has not yet been explored in Arctic tundra ecosystems. Previous research has shown that X-Band SAR data is sensitive to the height and density of tall shrub (~1 m) vegetation. In the following study we used a three-year TerraSAR-X (TSX) X-Band time-series of backscatter and coherence from three orbits to explore relationships to vegetation greenness extracted from time-lapse phenological cameras (phenocams) at the long-term low Arctic monitoring site of Qikiqtaruk (Herschel Island) in the north western Canadian Arctic. Data were aggregated at regional (115,000 ha) and local (0.78 ha) scales and compared between orbits, polarizations and years. Further aggregation by pre-defined ecological classes revealed complex seasonal trends dependent on incidence angle and surface characteristics. Only the ecological class with erect shrub species (~50 cm) in mid moisture locations showed a decrease in backscatter intensity in the cross-polarized VH/VV channel with increasing vegetation greenness. All other fully vegetated, non-disturbed classes showed decreasing backscatter trends in the HH/VV co-polarized orbits suggesting sensitivity to seasonal surface drying rather than increased volume scattering by vegetation. Patterns at the regional scale showed no obvious relationship with vegetation phenology derived from phenocam time-lapse photography. This preliminary investigation does not strongly support the use of TSX X-Band data as a potential proxy for vegetation phenology in a diversity of low Arctic tundra types. However, it complements previous research on the varying sensitivities of cross- and co-polarized channels on monitoring vegetation and surface conditions, respectively and warrants further study.

4.2 INTRODUCTION

The use of Synthetic Aperture Radar (SAR) in remote sensing of Arctic permafrost environments has increased in recent years with a concurrent increase in operational SAR satellites such as the RADARSAT-2, Sentinel-1, which operate at C-Band (6 cm λ) as well as TerraSAR-X which operates at X-Band (3 cm λ) (e.g. Antonova et al., 2016; Banks et al., 2017; Stettner et al., 2018; Ullmann et al., 2014a; Widhalm et al., 2017; Zwieback et al., 2017). With these missions, the availability of microwave remote sensing data in high spatial resolution has greatly increased. SAR is particularly appealing for applications in the persistently cloud covered Arctic biome due to the independence of backscatter and coherence magnitude to atmospheric conditions. The application and interpretation of SAR data in Arctic tundra ecosystems is still a developing area of research (Bartsch et al., 2016) however, initiatives such as the Polar Space Task Group (PSTG) have focused efforts on improving knowledge and understanding of these data. Given the efforts of the PSTG and the atmospheric independence, dense landscape-scale time-series are available at temporal scales rarely obtained in Arctic ecosystems with optical imagery (Stettner et al., 2017). Applications ranging from subsidence (Antonova et al., 2018; Zwieback et al., 2017), to snow cover (Stettner et al. under review), to land cover classification (Ullmann et al., 2014) demonstrate the versatility of X-Band SAR data and highlight the highly complementary potential of these datasets.

Vegetation phenology in the Arctic is a sensitive indicator of climate change as it is primarily controlled by the timing of snowmelt (Barker, 2007; Bjorkman et al., 2015b; Cleland et al., 2007; Høye et al., 2013; Inouye, 2008; IPCC, 2014b; Schwartz et al., 2006). Decreases in spring snow cover have led to longer growing seasons altering vegetation phenology and composition including advanced spring phenology and the expansion of shrub species at some sites (Brown & Robinson, 2011; Myers-Smith et al., 2011; Høye et al., 2007). Shifts in vegetation phenology such as advanced spring phenology can impact species-climate interactions making species more susceptible to damage from frost and soil saturation as well as impacting primary productivity and annual carbon sequestration (Park et al., 2016; Wheeler et al., 2015; Wipf et al., 2009).

Arctic shrubs can be a dominant and often conspicuous woody species compared to the relatively prostrate and herbaceous nature of most Arctic tundra vegetation. Shrubs have diverse growth forms including tall multi-stemmed shrubs (0.4–4.0 m), erect dwarf shrubs (0.1–0.4 m), and prostrate dwarf shrubs (<0.1 m) that grow laterally along the ground surface (Myers-Smith et al., 2011). The expansion both laterally, and volumetrically of shrub vegetation

affects ecosystem processes impacting snow depth and associated hydrologic dynamics, nutrient exchange and associated net carbon balance, as well as albedo and associated energy fluxes (Lafleur and Humphreys, 2018; Mekonnen et al., 2018; Paradis et al., 2016). The direction and magnitude of shrub expansion processes and associated feedbacks are still relatively unknown (Myers-Smith et al., 2011), and thus capturing shrub cover change and phenology using new data sources would be beneficial for quantifying shrub cover change across the tundra biome.

Previous research by Ullmann et al. (2014) suggested that the use of shorter wavelengths from X and C-Band backscatter data is superior for the characterization and differentiation of wetland and tundra vegetation. The contribution of ground components in X-Band backscatter is less influential than in C-Band backscatter data making it more suitable for vegetation studies (Ulaby et al., 1986). In addition to the influence of wavelength, Duguay et al. (2015) showed that incidence angles are important to consider depending the desired application. They found that low incidence angles are more sensitive to shrub density, while high incidence angels are more sensitive to shrub coverage. This phenomenon is explained by a lower contribution by the ground signal with higher incidence angles due to greater proportions of volume scattering compared to surface scattering (Ulaby et al., 2014).

Given the high spatial and temporal heterogeneity of soil moisture in Arctic ecosystems, X-Band data with varying incidence angles should be superior for applications of vegetation monitoring in Arctic ecosystems due to the lower degree of surface scattering at this wavelength. X-Band SAR backscatter data has been previously related to Leaf Area Index (LAI) in agricultural systems with a general dependence on the dielectric properties of green vegetation, i.e. water content (Fontanelli et al., 2013; Ulaby et al., 1982). X-Band SAR has also been used extensively in forest applications including forest height and biomass estimations (Englhart et al., 2011; Perko et al., 2011). In Arctic ecosystems there have been many recent studies on land cover classifications using X-Band SAR (e.g. Banks et al., 2013; Ullmann et al., 2016, 2014a; Widhalm et al., 2015). Initial attempts to relate vegetation parameters of Arctic shrubs to X-Band backscatter showed that cross-polarized VH channels have the greatest sensitivity to shrub height and density in stands less than 1 m in height and densities lower than 20% (Duguay et al., 2015). While X-Band backscatter data have been related to land cover classifications and vegetation parameters, the ability of these data to track the seasonal emergence, growth and senescence (vegetation phenology) of shrub and non-shrub vegetation has not been explored.

This study represents a first attempt to explore the capabilities of X-Band Terra-SAR-X (TSX) data to characterize the phenological emergence and expansion of low Arctic tundra vegetation on Qikiqtaruk (Herschel Island), off the coast of the Yukon Territory in north western Canada. Cross (VH/VV) and co-polarized (VV/HH) multi-pass backscatter and coherence time-series from 2015 to 2017 were compared to greenness time-series from 2016 and 2017 extracted from in-situ phenological time-lapse cameras. We aimed to answer the following three main research questions: 1) Do TSX X-Band backscatter and coherence time-series correspond to in situ phenological greenness time-series? 2) Does incidence angle and polarization influence the observed relationship? 3) How does the relationship change from the regional to local scale?

4.3 STUDY AREA

Qikiqtaruk (Herschel Island; 69°34′N; 138°55′W) is located on the north-western Yukon coast in the western Canadian Arctic approximately 2 km off the mainland (Figure 4-1). The climate of Qikiqtaruk is polar continental with mean annual air temperatures between -9.9 and -11 °C and mean annual precipitation between 161 and 254 mm $year^{-1}$ (C R Burn, 2012). The dominant wind direction is northwest and storms are frequently observed in late August and September (Solomon, 2005). The island is characterized by rolling hills with a maximum elevation of 183 m above sea level and polygonal tundra that is dissected by a variety of different valley types (De Krom, 1990; Rampton, 1982).

Qikiqtaruk is classified as a lowland tundra vegetation type and is dominated by dwarf shrubs, graminoids as well as a species-rich forb community and a well-developed moss layer (Kennedy et al., 2001; Myers-smith et al., 2011; Smith et al., 1989). Sediments are unconsolidated, fine-grained glacigenic material with marine origin (Blasco et al., 1990; Fritz et al., 2012). Active layer thickness is between 40 and 90 cm depending on topography (Burn and Zhang, 2009; Kokelj et al., 2002). Qikiqtaruk is underlain by continuous and extremely ice-rich permafrost with mean ice volumes of 30 to 60 vol%, and maximum volumes > 90 vol% when massive ground ice beds are present (Couture and Pollard, 2017; Fritz et al., 2015; H Lantuit et al., 2012). Mean annual air temperatures increased 2.7 °C between 1970 and 2005 which has resulted in a deepening of the active layer by 15 to 25 cm between 1985 and 2005 (Burn and Zhang, 2009), with active layers continuing to deepen by 20 cm between 1999 and 2017 in the areas of ongoing ecological monitoring (Myers-Smith, under review).

Seasonal snow cover typically starts in September and lasts until June. The majority of the annual snow fall occurs in autumn prior to sea ice formation. Strong winds affect the snow

distribution leading to thin snow cover on upland surfaces and large snow drifts in topographic depressions such as valleys and gullies (C R Burn, 2012). Some snow patches in north-facing and shaded aspects last throughout the summer, in particular when protected from melting by an insulating layer of plant detritus.

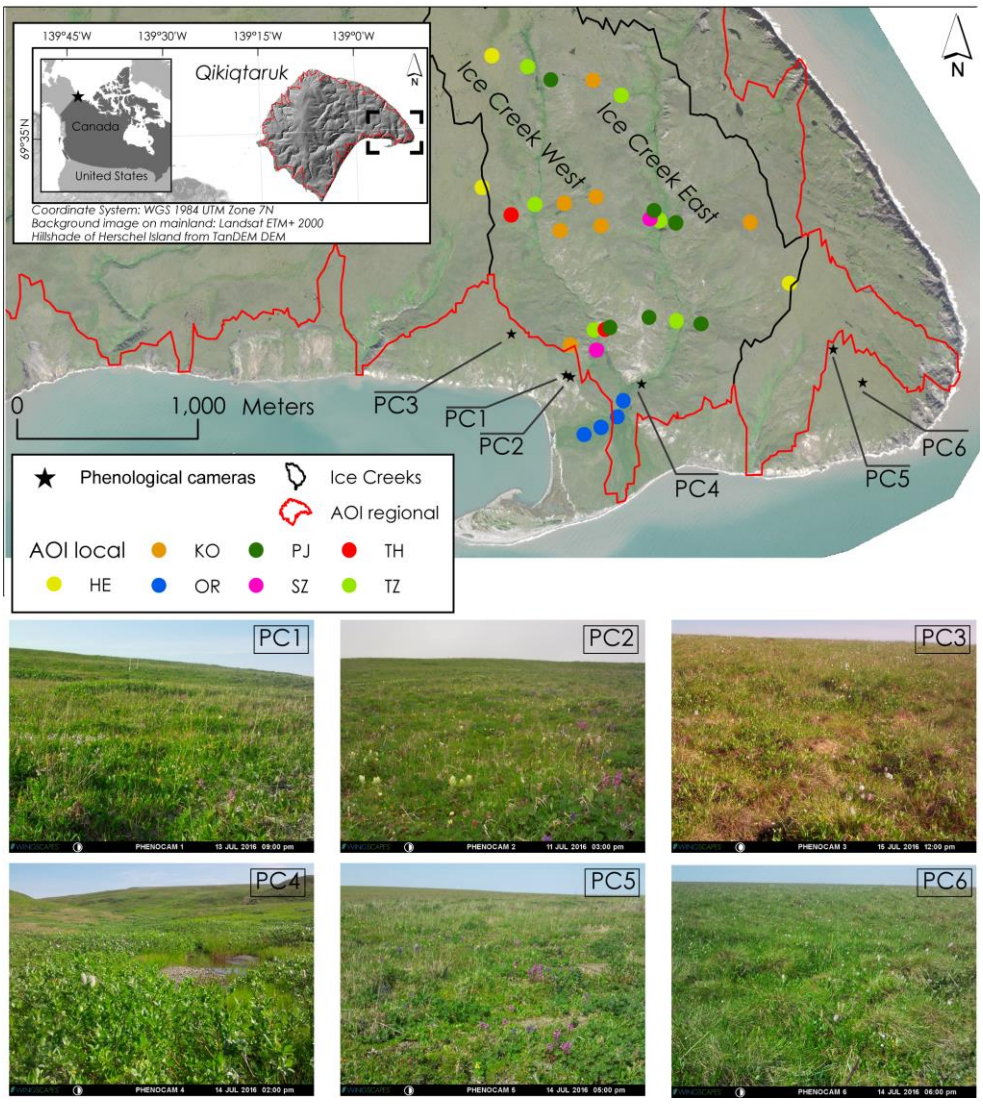

Figure 4-1: Overview of the Qikiqtaruk study site. The inset map shows the location of Qikiqtaruk (Herschel Island) along the Yukon Coast in the Western Canadian Arctic. The main map shows the locations of the Phenological Cameras PC1 to PC6 as well as the border of the Ice Creek watersheds in black and the Areas of Interest (AOI) in the red circles. The red border indicates the AOI of the entire Island, represented by all merged catchments identified by (Ramage et al., under review). The coloured circles represent the sites where the local (circle with 100 m diameter) backscatter signals were extracted. Different colours represent different ecological classes modified from (Obu et al., 2016). Detailed descriptions are available in Table 4-1. HE: Herschel; KO: Komakuk, OR: Orca, PJ: Plover and Jaeger, TH: Thrasher, SZ: Shrub zone, TZ: Transitional zone. The pictures at the bottom show the field of view of the phenological cameras at peak season 2016.

Qikiqtaruk was divided into ecological classes by (Smith et al., 1989) creating holistic map units that contain information about vegetation, soil type and landscape processes that are used in this study (see Table 4-1). Other studies focusing on Qikiqtaruk have translated the ecological classes into more comprehensive landscape units (Kokelj et al., 2002) or grouped them based on vegetation and terrain characteristics (Obu et al., 2015).

Table 4-1: Overview of selected ecological units on Qikiqtaruk based on Smith et al. (1989) and adapted from Obu et al. (2015).

Ecological unit	Name defined by (Smith et al., 1989)	Topography	Geomorphic disturbance	Slope (°)	Soil type	Vegetation
Hummocky tussock tundra	Herschel (HE)	flat to gently sloping uplands with distinctive hummocks	absent	1 (0-4)	Orthic Turbic Cryosol	*Eriophorum* tussock tundra
Slightly disturbed uplands	Komakuk (KO)	gently sloping uplands to gentle slopes	slow downslope movements and gelifluction	4 (0-6)	Orthic Turbic Cryosol	Salix arctica, Dryas integrifolia and Fabaceae sp.
Alluvial fans	Orca (OR)	alluvial fans and other riverine sediment accumulations	fluvial accumulation	2 (1-6)	Regosolic Static Cryosol	Salix richardsonii shrub vegetation
Moderately disturbed terrain	Plover and Jaeger (PJ)	complex slopes with unvegetated patches	moderate downslope movements, gullying and active-layer detachments	5 (2-18)	Regosolic Static Cryosol	Salix sp., Dryas sp., Fabaceae sp., Saxifraga sp., Petasites frigidus and a range of other taxa
Strongly disturbed terrain	Thrasher (TH)	steep slopes, cliffs and retrogressive thaw slumps	strong gullying, active coastal erosion, slumping and other mass wasting	15 (8-26)	Regosolic Static Cryosol	Sparsely vegetated with Salix arctica, Lupinus, Myosotis and Senecio
Valley bottom terrain	Shrub zone (SZ)	gently sloping to flat	absent	4 (0-6)	Regosolic Static Cryosol	Dominated by Salix richardsonii, S. arctica, S. reticulate, and Equisetum sp.
Riparian terrain	Transitional zone (TZ)	Flat to gently sloping valley walls	absent	5 (2-18)	Regosolic Static Cryosol	Sedge tundra dominated by Carex bigelowii and Petasites frigidus

4.4 DATA AND METHODS

4.4.1 IN-SITU TIME-LAPSE PHENOLOGICAL CAMERAS

PLANTCAM time-lapse phenological cameras (phenocams) manufactured by WINGSCAPES were set up in the spring of 2016 and 2017 as part of ongoing phenological monitoring on the island (Andresen et al., 2018; Beamish et al., 2018; Brown et al., 2016; Kępski et al., 2017). Six cameras acquired images at an hourly resolution at a height of approximately 1 m above the tundra surface with a landscape field of view between May and August with varying acquisition periods between cameras and years. Five of the cameras (PC1, PC2, PC3, PC5 and PC6) had a north viewing aspect and one (PC4) had an east viewing aspect. PC3, PC5 and PC6 observed phenology of vegetation communities that are representative of the uplands of Qikiqtaruk with low vegetation and prostrate dwarf shrubs and minimal disturbance. PC1 and PC2 observed phenology of vegetation communities that are representative of upland vegetation with prostrate dwarf shrubs and with moderate disturbance. PC4 observed phenology of vegetation communities that are representative of areas with erect dwarf shrubs in lower lying valleys and stream morphology. The cameras were subject to disturbance by active layer thaw and weather resulting in data gaps of up to a week. The acquired images have a resolution of 3200 × 2400 pixels.

4.4.2 TIME-LAPSE IMAGE ANALYSIS

The time-lapse imagery was cleaned manually by removing images affected by clouds and sun glint resulting in a total of 1844 photographs from 2016 and 2017. Pixel values of the Red, Green, and Blue, channels (RGB, 0-255) were extracted from each image using a function written with the "rgdal" package (Bivand et al., 2014) in R version 3.4.3 (R Core Team, 2016). To estimate greenness of each image and to normalize variations in irradiance among images, the green ratio (rG) was calculated for every pixel and averaged over the entire image using the following equation:

$$rG = G/(R + G + B) \quad (1)$$

where G is the green channel value, R is the red channel value, and B is the blue channel value. A ratio was also calculated for the red (rR) and blue (rB) channels by rearranging eq. 1. A final index, the Greenness Excess Index (GEI), was calculated using the red, green, and blue ratios (Richardson et al., 2013):

$$GEI = 2\ x\ rG - (rR + rB) \quad (2)$$

The equation uses normalized RGB bands and accounts for variations in overall brightness and exposure (Nijland et al., 2013; Richardson et al., 2007). Although rG can be used to track phenological and productivity changes in vegetation, eq. 2 provides a more sensitive indicator of changes in plant pigment (Ide and Oguma, 2013). Greenness derived from digital photographs has been used extensively as a proxy for phenological development (Beamish et al., 2016; Ide and Oguma, 2013; Nijland et al., 2014; Richardson et al., 2007). This is desirable in tundra ecosystems as the changes can be subtle. The data were filtered to remove diurnal patterns by selecting the maximum greenness by day, resulting in 530 images in the two years.

4.4.3 SAR SATELLITE DATA

We used a multi-pass TSX time-series with dual cross-(VH/VV) and co-polarized (HH/VV) channels with acquisition dates between early June and late July from 2015 to 2017 (seeTable 4-2). TSX has an orbital revisit time of 11 days and operates using a right looking active phased array antenna at an X-Band centre frequency of 9.65 Ghz. The pixel spacing was 1.9 to 2.8 m in range and 6.6 m in azimuth and the incidence angles at the image scene centre of the orbits varied between 25° and 39°. Shadowing and layover can potentially affect the quality of TSX data, however, the relief of Qikiqtaruk is low and the influence is minimal. We only included areas of Qikiqtaruk within watersheds that were delineated by (Ramage et al., under review; Ramage, 2017)

Table 4-2: Overview on TSX orbits. RA = Range, AZ = Azimuth The incidence angle θ refers to the image scene centre.

	Acquisition time					
Orbit No.	**UTC**	**Local time**	**Orbit heading**	**Incidence angle θ**	**Pixel spacing**	**Polarization**
24	16:08	9:08	Descending	31°	2.3 / 6.6	HH / VV
61	2:26	19:26	Ascending	32°	2.2 / 6.6	VV / VH
115	15:59	8:59	Descending	39°	1.9 / 6.6	VV / VH
152	2:18	19:18	Ascending	25°	2.8 / 6.6	HH / VV

4.4.4 BACKSCATTER AND COHERENCE TIME SERIES

A time-series of the amplitude (backscatter intensity) and phase signal of the TSX images was created. For a given acquisition orbit all images were co-registered to sub-resolution

accuracy with respect to a pre-selected master image using the highly accurate orbital information from TSX and ellipsoidal heights. In order to avoid early season effects of snowmelt with resulting high variation in soil moisture and vegetation dynamics, we chose mid-summer acquisitions (July) as the master images when environmental conditions appeared stable. We applied a 3 × 9 multilooking to the intensity images in order to address the speckle effect inherent to SAR imagery and to obtain a roughly square pixel size of around 20 m (Table 4-2).

The coherence magnitude (herein simply referred to as 'coherence') of the SAR signal is a quality parameter between the complex signals of two image acquisitions. A loss of coherence can occur due to volumetric decorrelation, i.e. in case of changing surface scattering conditions between two acquisitions. We investigate if volumetric decorrelation occurs during the leaf out season in Arctic tundra. We used the shortest available temporal baseline of 11-days of TSX to calculate coherence. In both the backscatter and coherence time-series the data were subset to dates later than 6th June to ensure no acquisitions with frozen ground conditions were used.

We selected two sets of areas of interest (AOIs) representing a local and regional SAR signals. The first AOI was created using the entire Island excluding coastal regions and represented the regional backscatter and coherence signals. The island AOI was created by merging all catchments identified by (Ramage et al., under review). The second AOI consisted of 30 circular zones with 100 m diameter created based on the location of the in-situ vegetation plots plus three additional zones within the Orca ecological class of the delta. These 30 circular zones were used to represent local backscatter and coherence signals. For both the regional and local AOIs average backscatter and coherence signatures were extracted and examined by ecological classes adapted from (Obu et al., 2016).

4.4.5 IN-SITU VEGETATION AND CLIMATE DATA

To better understand observed patterns in backscatter and coherence time-series, *in-situ* vegetation parameters as well as climate data were collected. Vegetation composition was recorded at 27 sampling locations during the summer of 2014 between 31st July and 6th August within the Ice Creek watersheds (Eischeid, 2015). At each sampling location vegetation was recorded at three different plots within 10-15 m of the sampling location. Plant species, percent cover and canopy height were measured within a 50 × 50 cm frame. Two individual estimations of the percent plant cover and bare ground cover were

averaged. The depth of the active layer, moisture condition and the topographic position were also documented. Mean vegetation canopy height data were grouped into height classes of 0-10 cm, 10-15 cm, and <15 cm and the relationship to backscatter intensity by orbit and polarization was examined using box plots.

We used temperature and precipitation data from a weathers station operated by Environment Canada (WMO ID: 71501). Data were downloaded and compiled using the R package "rclimateca" (Dunnington, 2018). Due to a weather station malfunction, no precipitation data was recorded in 2015. Precipitation and temperature data were qualitatively compared to backscatter and coherence time-series data.

4.5 Results

4.5.1 Phenocams

Vegetation phenology inferred from the greenness excess index (GEI) extracted from the phenocams in 2016 and 2017 are presented in Figure 4-2. Green-up starts in early June after snowmelt and greenness values gradually increase until early July. During this time the structural changes such as leaf out, leaf expansion and stem elongation occur. Peak season starts in early July and vegetation activity and biomass peak towards the end of July. The first signs of plant senescence occur near the end of July, early August resulting in a degradation of cellular and canopy structure as well as colour changes.

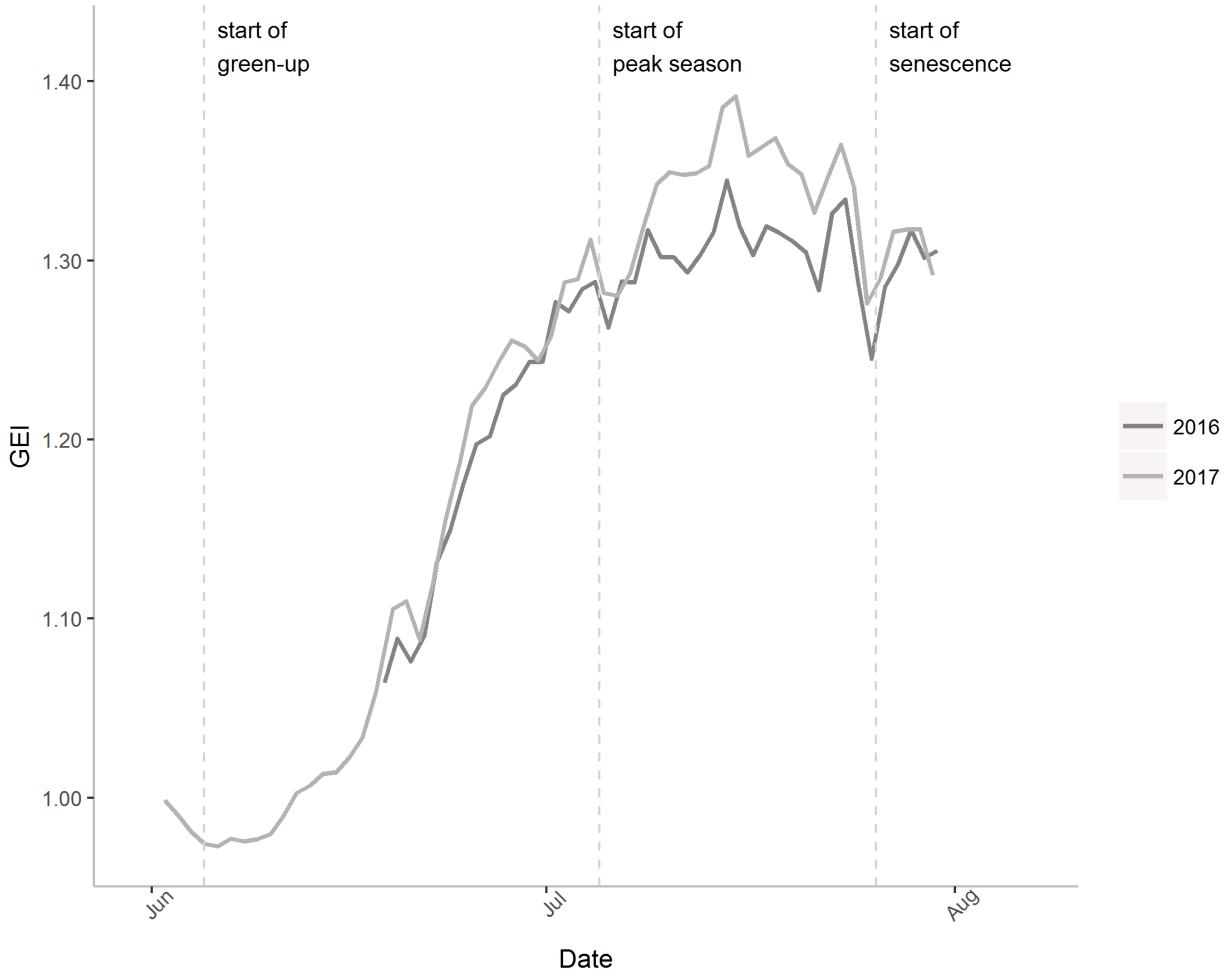

Figure 4-2: Greenness Excess Index (GEI) from the phenological cameras for the years 2016 and 2017. Vertical dashed lines indicate phenological phases from left to right: start of green-up, start of peak season, and start of senescence.

4.5.2 BACKSCATTER DYNAMICS

On the regional scale differences between orbits and years were large while polarization did not appear to greatly influence backscatter signatures (Figure 4-3). Orbit 61 had the lowest backscatter values followed by 152, and finally orbit 24. Only the cross polarized orbit 61 showed differences between the VH/VV polarizations. Backscatter intensity in 2016 was consistently higher than the other years but both 2016 and 2017 showed an increase in backscatter at the end of the growing season. The cross polarized VH/VV channel of orbit 61 had the most consistent backscatter signal between years showing a slight increase to peak season in 2015 and 2016 followed by a slight decrease to senescence. In 2017 a strong increase from the start of the peak season to the beginning of senescence was observed.

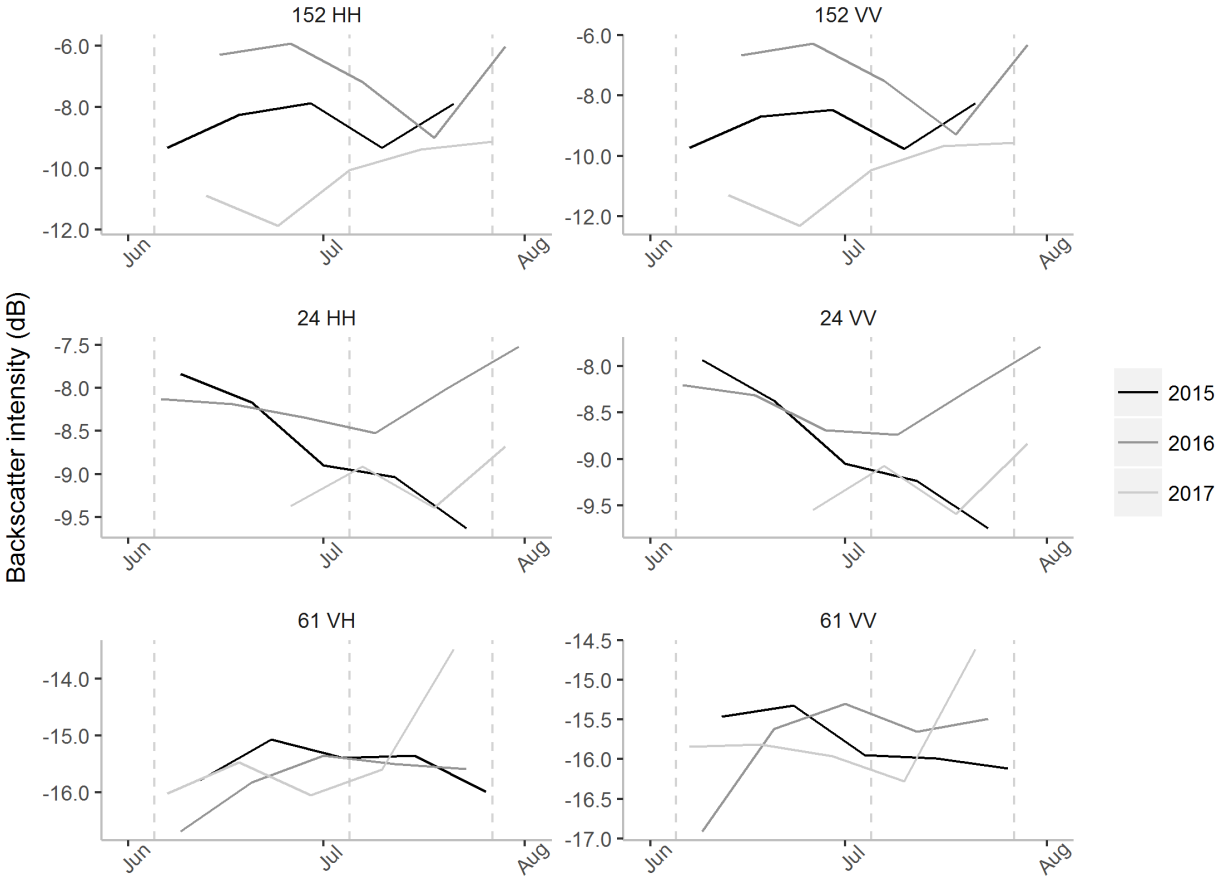

Figure 4-3: Backscatter intensity time-series at the regional scale by TerraSAR-X orbit and polarization. HH: Horizontal Horizontal, VV: Vertical Vertical, VH: Vertical Horizontal

On the local scale the backscatter signals between years were similar within the ecological classes but showed differing patterns between classes, orbits and polarizations (Figure 4-4, Figure 4-5, and Figure 4-6) Overall, the co-polarized (HH/VV) backscatter signals were more similar to one another across the growing season than the cross-polarized signals (VH/VV). The most consistent backscatter signals in the three years were observed in orbit 152 (HH/VV), particularly in the Thrasher (TH), Transitional Zone (TZ), and Shrub Zone (SZ) classes. High consistency was also observed in the TH class in orbit 61 (HH/VV). In most cases in the co-polarized channels the 2016 backscatter was highest.

In orbit 152 (HH/VV) there was a slight increase in backscatter from early to mid-June (Figure 4-4) corresponding to the end of snow melt and onset of green-up in all ecological classes. In the Komakuk (KO), Herschel (HE) and Plover-Jaeger (PJ) classes, this increasing pattern was more variable by year than the other classes. After this initial increase, KO, HE, PJ and Orca (OR) all showed a decreasing trend for the remainder of the time-series corresponding with an increase in greenness to peak biomass. In contrast, the

Thrasher (TH) and Transitional Zone (TZ) classes showed a continued increasing trend to early/mid-July followed by a plateauing or slight decrease during the greenness increase to peak biomass. PJ and KO showed a plateau during green-up and beginning peak season in 2016. The Shrub zone (SZ) showed a comparably flat backscatter signal throughout the time-series with the exception of 2017. PJ and TH had the highest backscatter and TZ had the lowest.

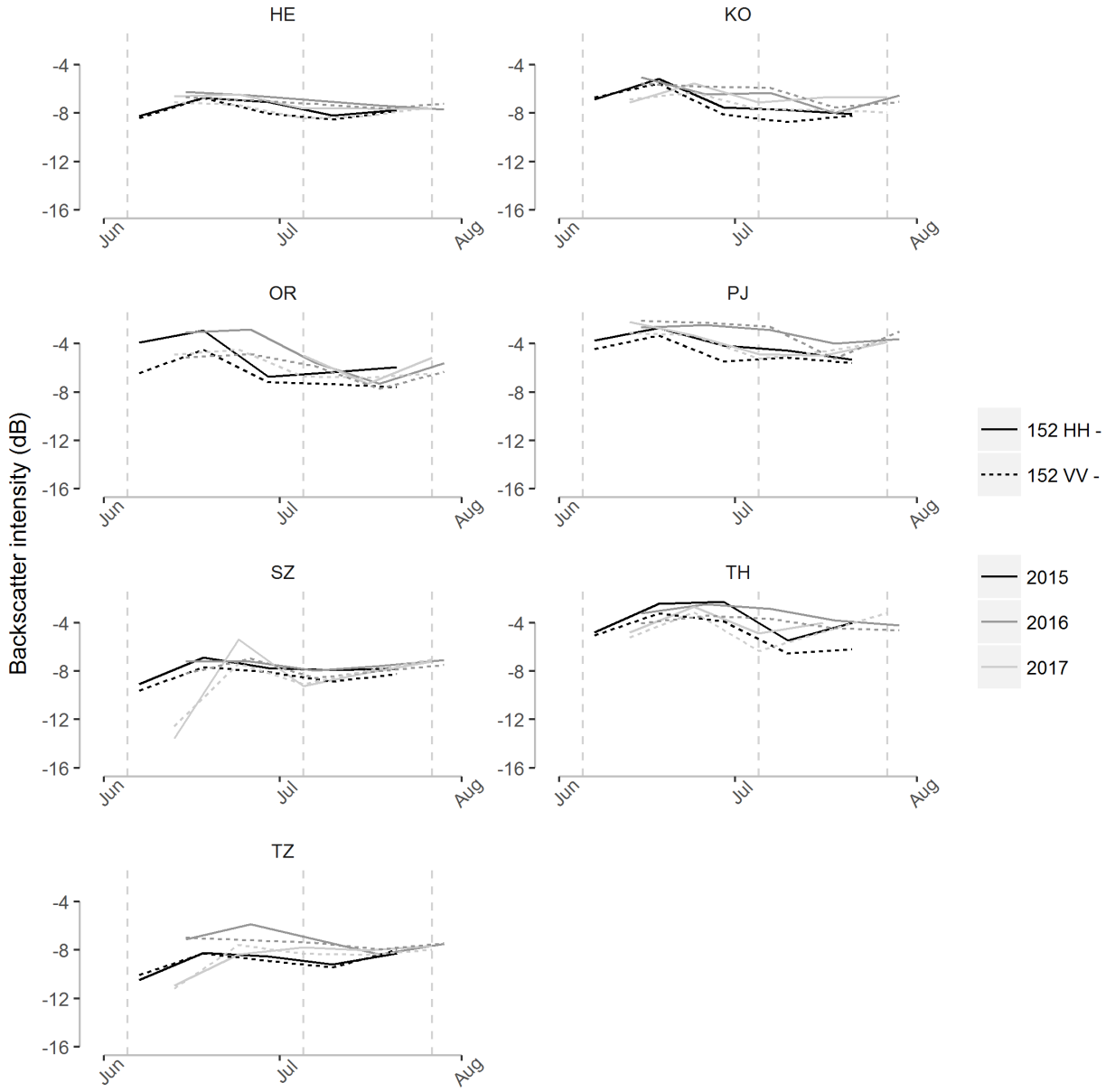

Figure 4-4: Backscatter intensity of ecological classes in the growing season of 2015 to 2017 as observed by TerraSAR-X orbit 152 (HH/VV) and the greenness excess index (GEI) for 2016 and 2017 extracted from the phenological cameras. The vertical dashed lines indicate phenological phases from left to right start of green-up, start of peak season, start of senescence. HH: Horizontal Horizontal, VV: Vertical Vertical, VH: Vertical Horizontal

The co-polarized channels in orbit 24 (HH/VV) had higher variability between years though the general trends were similar to orbit 152 (Figure 4-4). A decreasing backscatter trend in 2015 and 2017 was observed in HE, KO, OR, and PJ corresponding to green-up. OR had the most pronounced decrease in backscatter.

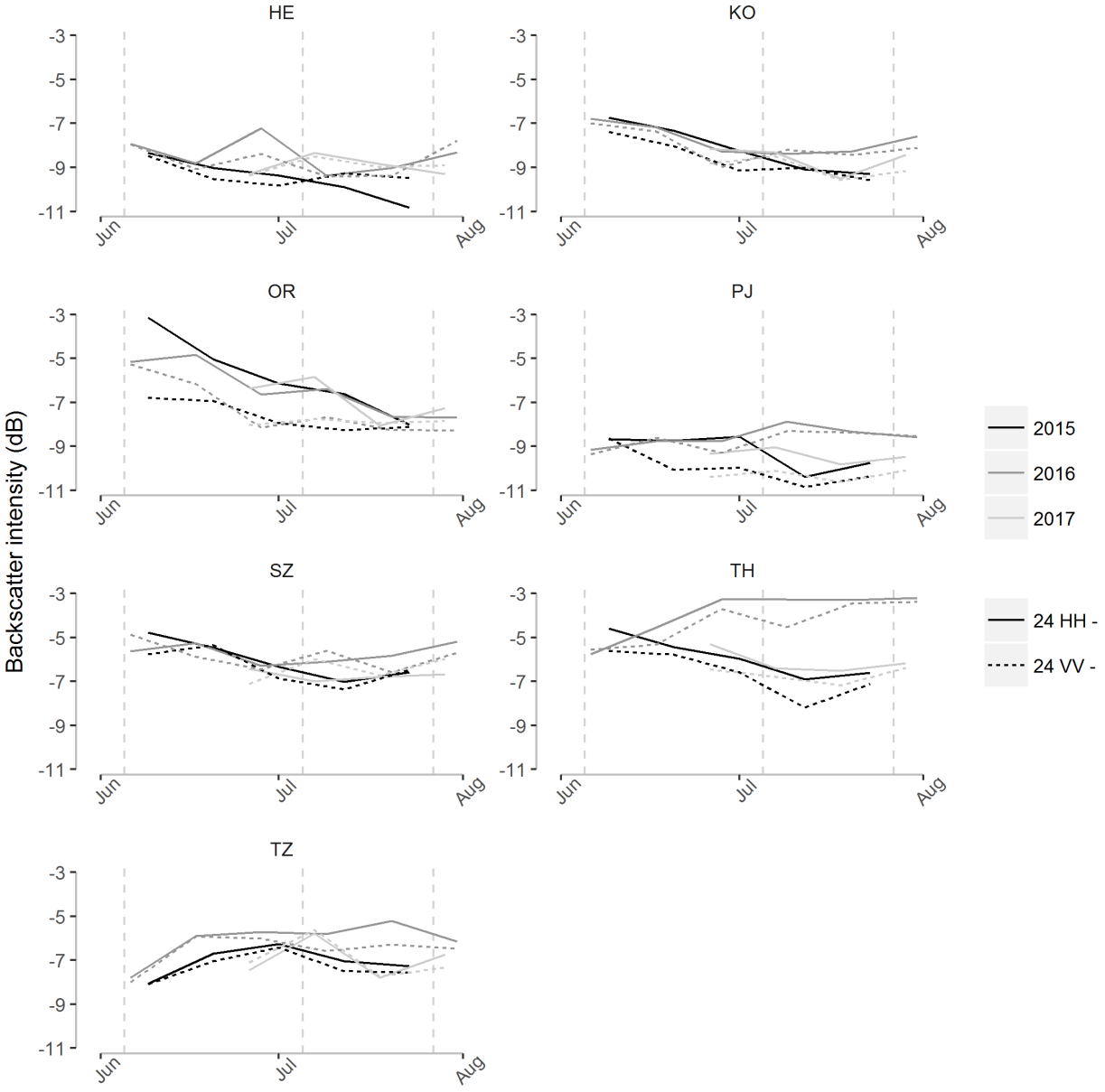

Figure 4-5: Backscatter intensity of ecological classes in the green-up season of 2015 to 2017 as observed by TerrSAR-X orbit 24 (HH/VV) and GEI for 2016 and 2017 as observed from the phenological cameras. The vertical dashed lines indicate phenological phases from left to right start of green-up, start of peak season, start of senescence. HH: Horizontal Horizontal, VV: Vertical Vertical, VH: Vertical Horizontal

TH showed an increasing trend during green-up and slightly decreased in peak season, although the signal was not consistent between the years. SZ and TZ showed the same flat and increasing to plateau trends, respectively, as orbit 152. PJ had the lowest backscatter across the season while SZ and TH had the highest. In the cross-polarized channels of orbit 61 (VV/VH) greater deviations were observed between the VV and VH polarizations, particularly in KO and OR in 2015 and 2017 (Figure 4-6).

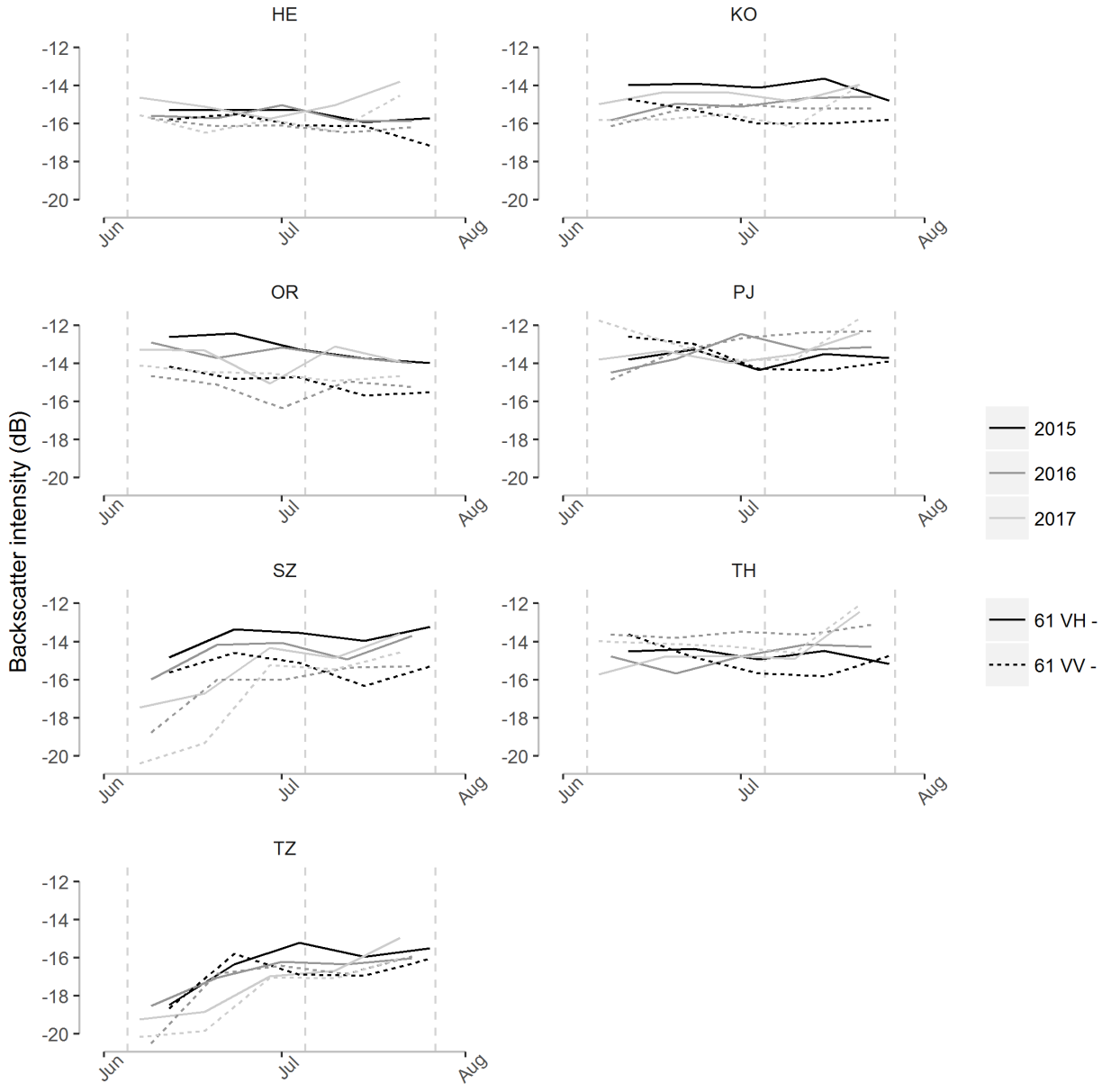

Figure 4-6: Backscatter intensity of ecological classes in the green-up season of 2015 to 2017 as observed by TerraSAR-X orbit 61 (VH/VV) and GEI for 2016 and 2017 as observed from the phenological cameras. The vertical dashed lines indicate phenological phases from left to right start of green-up, start of peak season, start of senescence. HH: Horizontal Horizontal, VV: Vertical Vertical, VH: Vertical Horizontal

PJ and TH had very similar seasonal patterns in 2015 but 2016 and 2017 were highly variable. The TZ and SZ class once again shows an increasing to plateau trend as well we high similarity between years as with orbits 152 and 61. SZ showed the most pronounced changes across the growing season.

4.5.3 COHERENCE DYNAMICS

The coherence signals on the regional scale did not differ between polarizations of the same orbit but did differ between orbits (Figure 4-7). In general, coherence variations were low ranging between 0.3 and 0.6. In 2015, all orbits showed increasing coherence from mid-June in the middle of the green-up phase to the start of the peak season after which values plateaued or decreased. In 2016, no clear trend of coherence was visible and in 2017 all orbits show a decreasing coherence across the growing season.

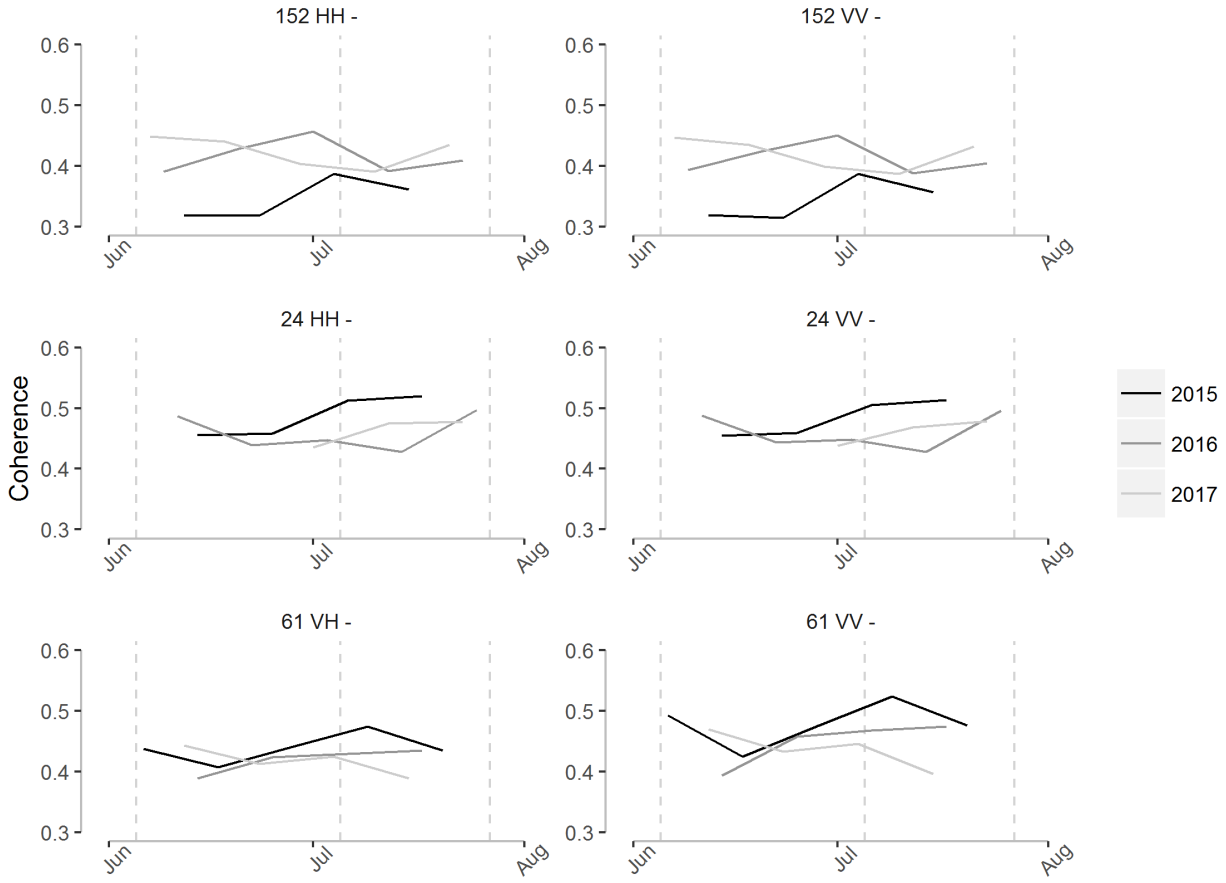

Figure 4-7: Coherence time-series at the regional scale by TeraaSAR-X orbit and polarization. HH: Horizontal Horizontal, VV: Vertical Vertical, VH: Vertical Horizontal

Overall, deviations in coherence were low across the growing season in all orbits and polarizations (Figure 4-8, Figure 4-9, and Figure 4-10). Differences between years within

ecological classes were more pronounced than with backscatter and cross-polarized channels showed greater differences than co-polarized channels. Orbit 152 had the greatest deviations in coherence while orbit 24 had the lowest. In orbit 152 most ecological classes show an increase of coherence around the beginning of July and the start of the peak season in most years. HE showed the opposite trend with a loss of coherence at the start of peak season. OR had the most consistent coherence trend between years and KO had the least.

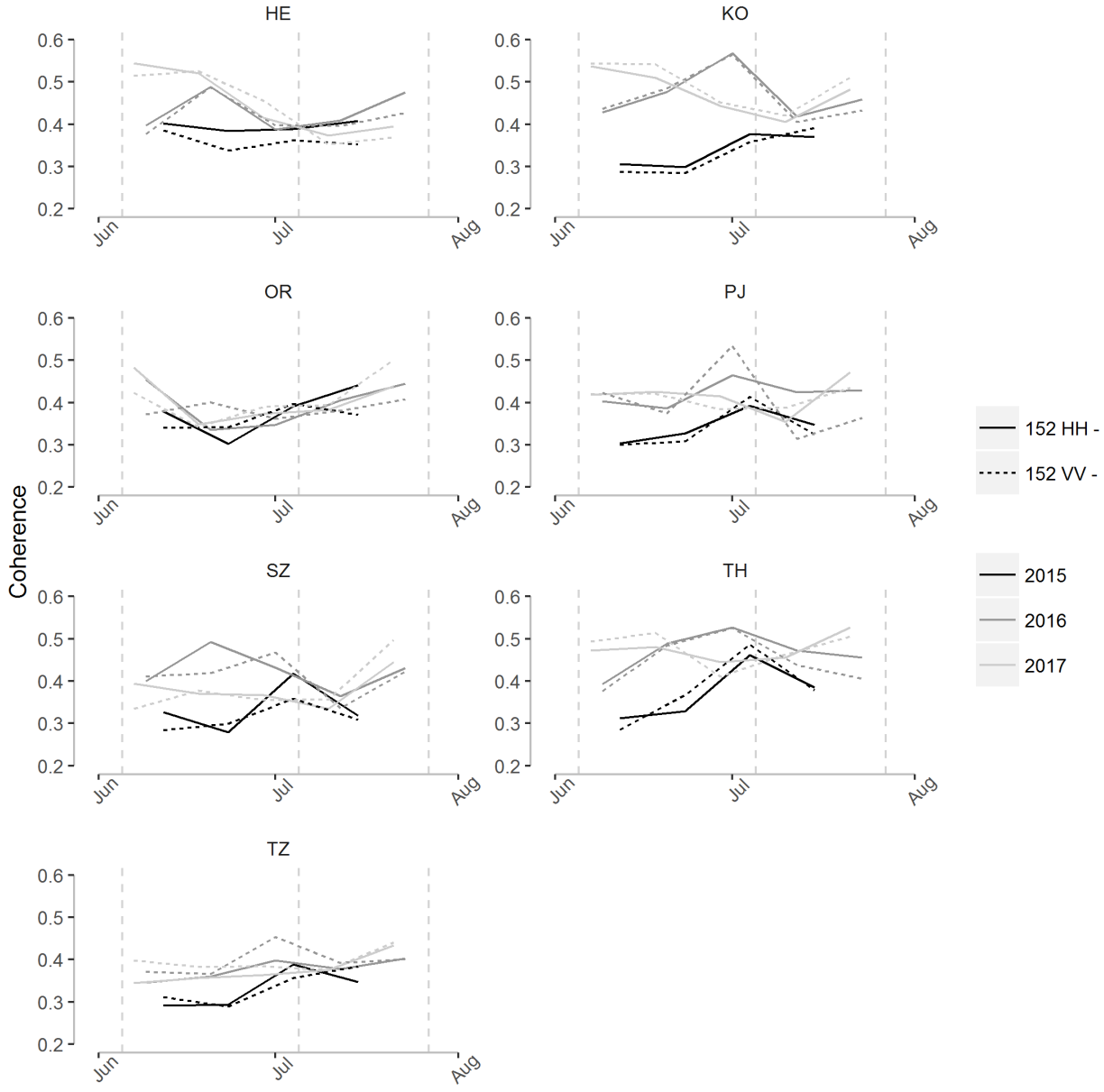

Figure 4-8: Coherence time-series of ecological classes in the green-up season of 2015 to 2017 as observed by TerraSAR-X orbit 152 (HH/VV). The vertical dashed lines indicate phenological phases from left to right start of green-up, start of peak season, start of senescence. HH: Horizontal Horizontal, VV: Vertical Vertical, VH: Vertical Horizontal

The coherence time-series of the co-polarized channels in orbit 24 showed slight increasing trends during green-up, except the upland HE class (Figure 4-9). In 2016, during peak season a drop in coherence was observed followed by an increase towards the end of peak season in all ecological classes.

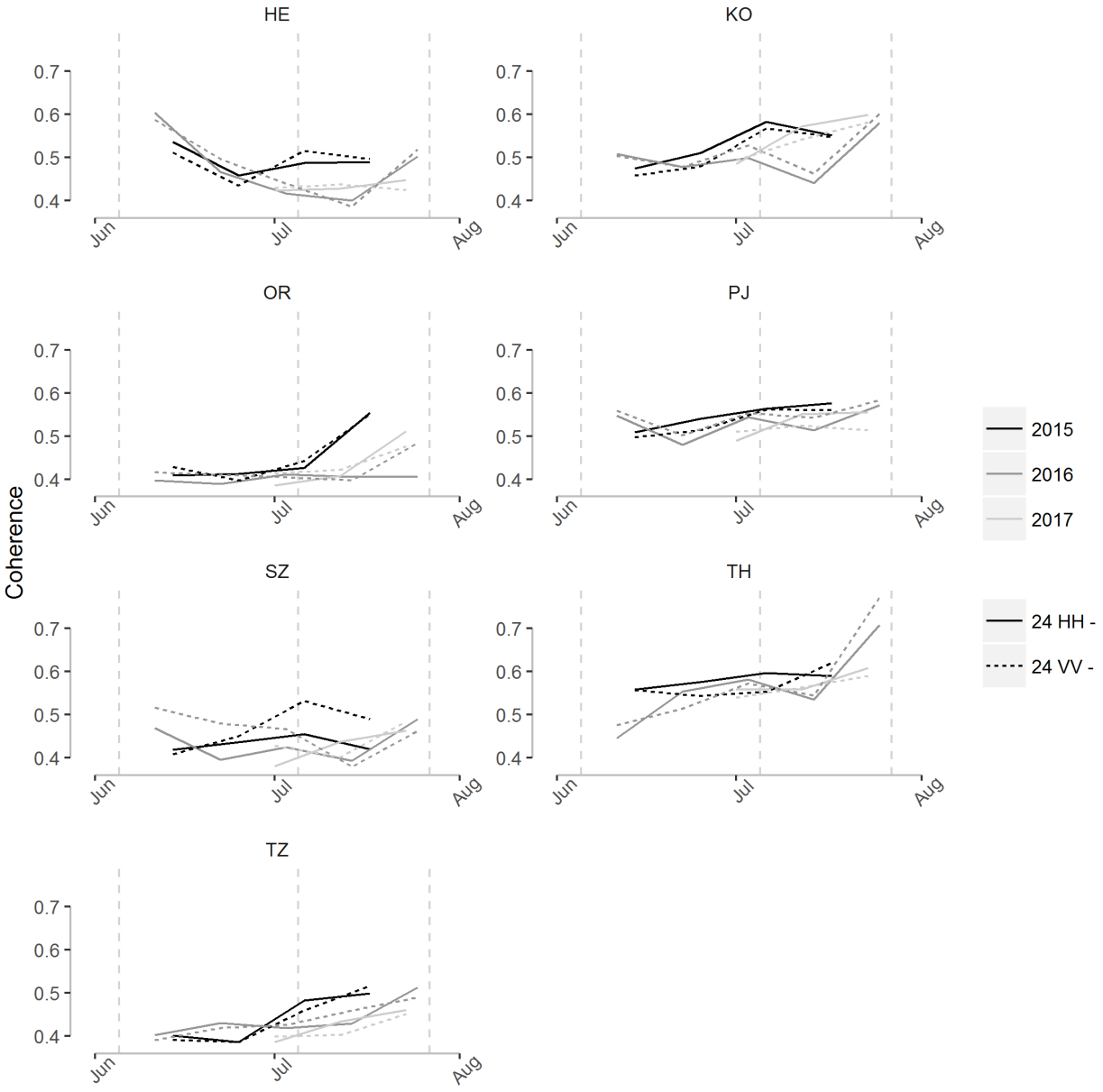

Figure 4-9: Coherence time-series of ecological classes in the green-up season of 2015 to 2017 as observed by TerraSAR-X orbit 24 (HH/VV). The vertical dashed lines indicate phenological phases from left to right start of green-up, start of peak season, start of senescence. HH: Horizontal Horizontal, VV: Vertical Vertical, VH: Vertical Horizontal

Orbit 61 showed strong variations in the range of coherence values between ecological classes though seasonal trends were similar to orbit 152 (Figure 4-8). Coherence initially decreased to mid-June then showed the same loss of coherence around early to mid-July as in orbit 152 corresponding to the start of the peak season. After early to mid-July coherence once again decreased corresponding to the greenness plateau (Figure 4-2) and peak biomass. SZ, OR, and TZ all had lower coherence values across the growing season compared to the remaining ecological classes.

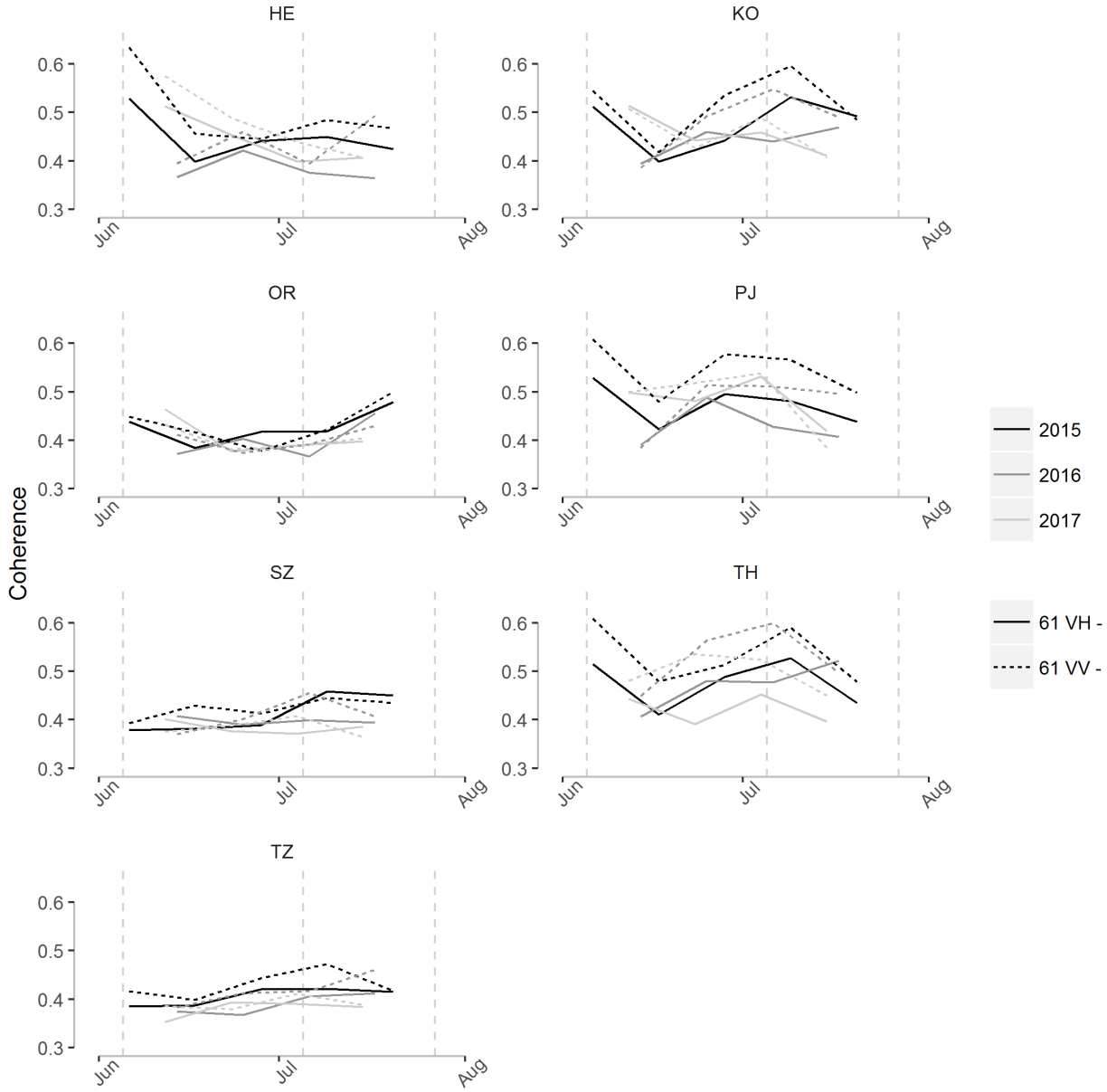

Figure 4-10: Coherence time-series of ecological classes in the green-up season of 2015 to 2017 as observed by TerraSAR-X orbit 61 (VH/VV).The vertical dashed lines indicate phenological phases from left to right start of green-up, start of peak season, start of senescence. HH: Horizontal Horizontal, VV: Vertical Vertical, VH: Vertical Horizontal.

4.6 CLIMATE DATA

The climate data for the observation period in 2015 to 2017 show different conditions between years (Figure 4-11). The 2015 growing season had the warmest spring temperatures concurrent with the green-up phase. The 2016 and 2017 growing seasons showed very similar temperature conditions in the late green-up and peak season, with a drop of air temperature in late July. In 2016, the temperatures increased earlier with two warm periods in mid-June during the green-up phase. The 2016 growing season was considerably wetter than 2017 with precipitation events throughout June and July, while 2017 only shows some events in mid to late July.

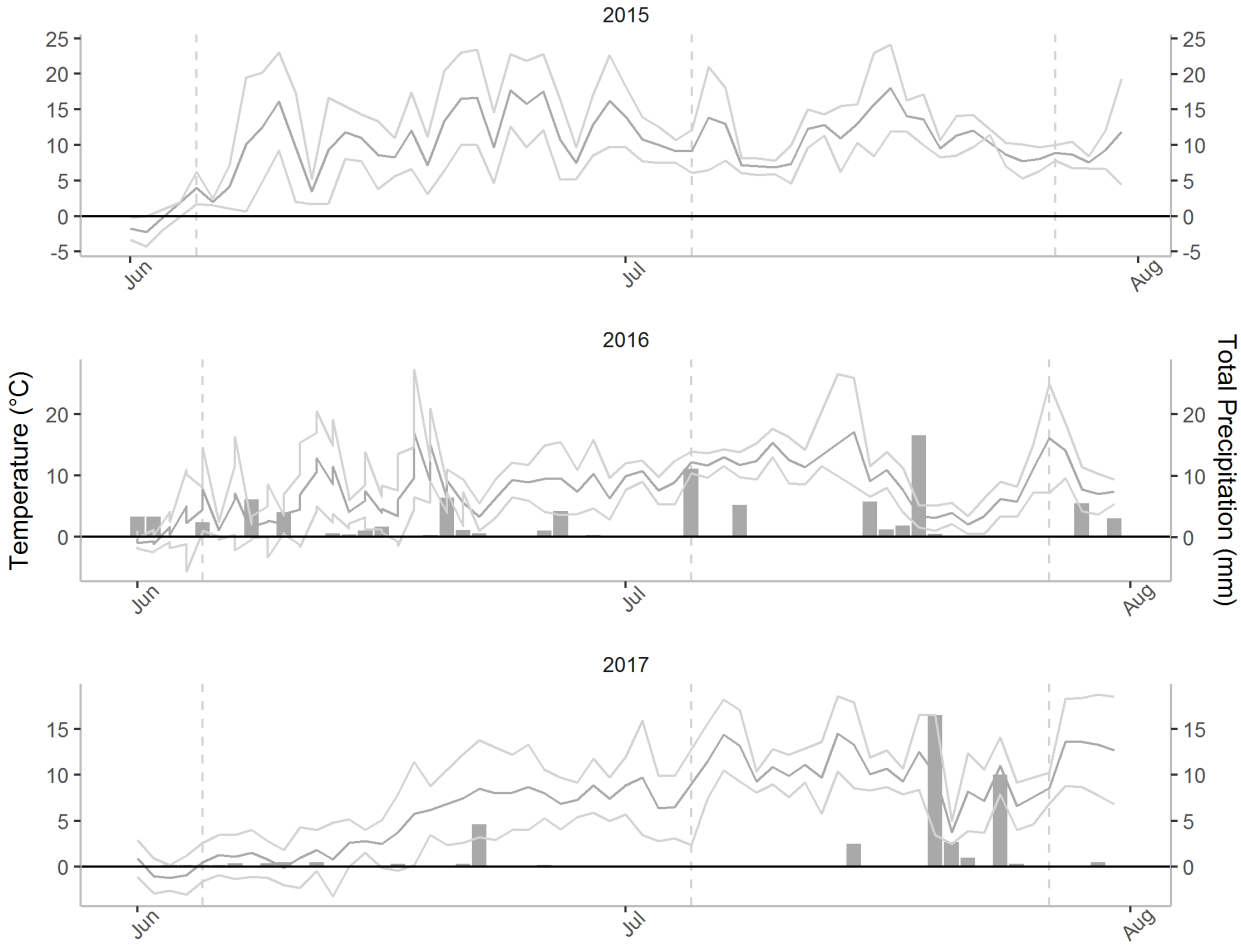

Figure 4-11: Mean daily temperature (Mean Temp ° C) in 2015, 2016 and 2017 and total daily precipitation (Total Precip. mm) in 2016 and 2017. Due to a station malfunction there was no precipitation data recorded in 2015. Vertical dashed lines indicate phenological phases from left to right: start of green-up, start of peak season, and start of senescence. Solid dark grey lines represent mean daily temperatures and light grey represent maximum and minimum daily temperatures. Dark grey bars represent total daily precipitation in mm.

Total precipitation was 87.9 and 41.5 mm between June 1st and August 1st for 2017 and 2016, respectively. Of this total precipitation there were 7 and 2 events over 5 cm in 2016 and 2017, respectively.

4.7 BACKSCATTER AND VEGETATION HEIGHT

The grouped mean canopy height data collected in 2014 at 27 locations showed variable relationships with mean backscatter intensity (2015-2017) from the same time period (July 31st – August 6th) (Figure 4-12). Orbit 152 and 24 showed increasing backscatter with height class but this was variable between polarizations. The cross-polarized orbit 61 showed no obvious relationships with backscatter.

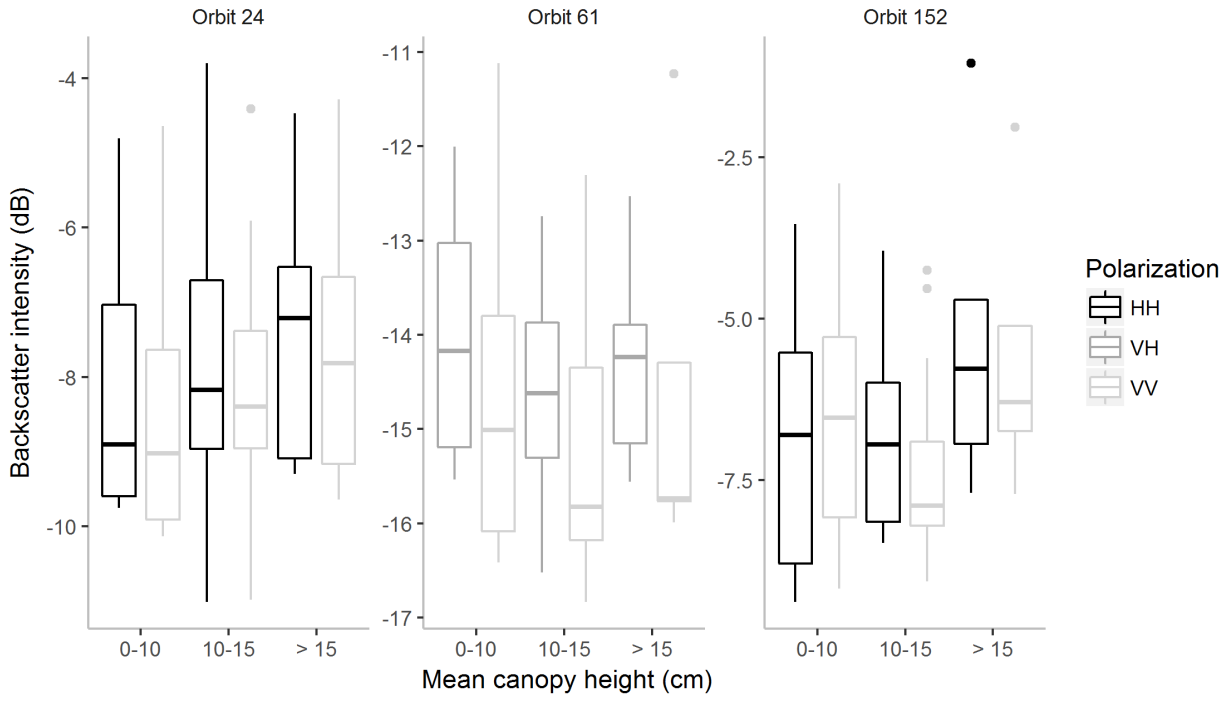

Figure 4-12: Backscatter intensity by mean canopy height class by TerraSAR-X orbit and polarization.

4.8 DISCUSSION

The relationships between TSX X-Band backscatter and coherence and vegetation greenness are complex and vary by incidence angle, polarization, spatial scale, and surface properties. The results of this study add to previous research on the relationship between Arctic vegetation and SAR by incorporating a phenological time-series aspect. The complexity of the observed backscatter and coherence time-series could be explained by the concurrent ecosystem phenomena occurring throughout phenological development of

vegetation, particularly green-up, which have varying degrees of importance depending on topographic position. One such phenomenon is the presence of late-lying snow patches, particularly in low-lying areas such as valley bottoms. The presence of late-laying snow in recently snow free areas are the main contributors to the backscatter intensity and corresponding coherence during green-up as areas transition from wet snow (saturation) to no snow (surface thawing and/or drying). Before areas are completely snow free and active layer thickness is low, the surface moisture is relatively high and diurnal freeze thaw cycles are occurring. Depending on acquisition time of the orbital pass, high surface moisture or a frozen layer may greatly affect the measured backscatter intensity in positive or negative direction, respectively and effect the corresponding magnitude of coherence (Floricioiu and Rott, 2001; Reber et al., 1987; Stettner et al., under review).

A second phenomenon associated with the end of snow melt and emergence of vegetation is a concurrent increase in volume scattering by expanding and elongating vegetation as well as surface drying due to a lower water table as the active layer deepens. These two phenomena have opposite effects on backscatter intensity, respectively decreasing and increasing the signal (Widhalm et al., 2017). Our results showed that the upland HE and upper slope KO ecological classes had decreasing trends of backscatter with increasing trends of greenness in the co-polarized orbits of 152 and 24. This was particular visible in orbit 24 which has a higher incidence angle than orbit 152. This decreasing trend suggests these ecological classes are dominated by surface drying rather than a volume scattering by vegetation. Co-polarization channels have been shown to penetrate the vegetation layer having greater sensitivity to ground surface conditions (Ullmann et al., 2016; White et al., 2015). Upland tundra sites were the first to melt out and therefore were likely to be the first to experience drying (Figure 4-4, Figure 4-5, and Figure 4-6). In addition, the volume scatter by vegetation was likely minimal as upland tundra sites are dominated by prostrate shrubs such as *Dryas integrifolia* and thinned stemmed graminoids such as *Arctagrostis latifolia, Alopecurus alpinus, and Eriophorum vaginatum* that are likely invisible to the 3 cm wavelength of the TSX X-Band (Ulaby et al., 1984). The decreasing backscatter trends were accompanied by relatively low (0.4-05) and stable coherence values in the co-polarized orbits with variations of approximately 0.2 across the entire growing season. An increase in coherence towards the end of peak season suggests a stabilization of near surface hydrology during the peak season, which is supported by a relative plateau in backscatter at this time.

Only the TZ and SZ showed expected increasing backscatter trends with advancing vegetation phenology in the cross-polarized orbit 61. The similarity in seasonal trends between these two ecological classes is likely driven by very different effects of the respective surface properties. The TZ is characterized by wet, low lying areas and late-lying snow patches. The decreasing backscatter in the TZ is likely the result of high soil moisture throughout the growing season. Saturated soils have been shown to decrease backscatter intensity by up to 4dB (Baghdadi et al., 2008) Volume scattering by vegetation may also contribute to the decreasing backscatter but given the insensitivity of the dry, graminoid dominated upland sites we speculate that this is also the case in wet, graminoid dominated TZ areas.

The SZ dominated by tall shrub species such as *Salix richardsonii* appears to be the only ecological class that shows an effect of volume scattering by emerging and expanding leaves. This is supported by the comparably low coherence signals across the green-up phase which suggests changing surface properties. Cross-polarized channels have been shown to be sensitive to both shrub vegetation height and density (Duguay et al., 2015; Ullmann et al., 2014). The dielectric properties, i.e. water content of vegetation have been shown to be influential on backscatter properties (Ulaby et al., 1984). The oblate leaves and multi-stemmed structure of tall Arctic shrub species provide more surface area for the diffuse scattering of microwaves (Duguay et al., 2015). TSX backscatter intensity has been shown to correlate to Landsat 8 greenness data that is dependent on land cover type which supports the inference of phenological development from the cross-polarized orbit 61 (Ullmann et al., 2014). The corresponding coherence of cross-polarized orbit 61 in SZ areas showed a general increase in coherence towards the beginning of peak season followed by a plateau or slightly decreasing coherence suggesting a maximum canopy was reached and maintained. Interestingly, the wet, low-lying shrub class of OR that occurs in flat delta terrain showed a decreasing seasonal trend in the co-polarized orbits despite tall shrub vegetation. This could be the result of complex volume scattering interactions between the vegetation and standing water resulting in lower returns to the SAR antenna.

The coherence signals at the regional scale were variable and minimal changes in coherence (>0.2) made attribution of changes to vegetation difficult. In contrast to our hypotheses that the coherence would decrease during green-up because of changes in plant structure, most orbits showed a slight increasing trend during the green-up and peak phenology phase. This could be explained by a homogenization of the surface and surface

conditions as the growing season progresses with vegetation expanding fully and a thickening of the active layer, reducing the variability of surface conditions. Another reason for the minimal changes in coherence could be variations in the spatial interferometric baselines and co-registration which affect the quality of coherence. Comparably higher backscatter signatures in 2016 could be related to a higher wetness in this year. The variability is likely the result of interactions between topography, vegetation and surface conditions across the island and well as technical limitations of the data and methods. Variations in the spatial baseline causing volume decoupling and co-registration errors, particularly for pairs of acquisitions towards the end of snowmelt, may impact the accuracy of the data.

4.9 Conclusion

Overall, our results suggest that TSX X-Band cross- polarized VH/VV backscatter data has potential as a proxy for regional vegetation phenology in dry, tall shrub communities of the low-Arctic site of Qikiqtaruk. Outside of the dry, tall shrub areas, backscatter signals appear to be dominated by changing surface moisture properties or a complex scattering between vegetation and standing water. The independence of the non-shrub areas from volume scattering by vegetation is either due to the prostrate and graminoid nature of the vegetation or a high contribution of bare ground. Coherence data showed variable trends across the growing season by year and orbit. The results of the time-series analysis support previous SAR research that cross-polarized channels (VH/VV) are more sensitive to and superior for monitoring vegetation and co-polarized channels (HH/VV) are more sensitive to sub-canopy ground surface conditions. Further, our results suggest a sensitivity of TSX X-Band data to seasonal moisture variations in low and sparsely vegetated areas. This study represents an initial attempt to relate backscatter and coherence to the phenological development of and provides valuable information on the temporal dynamics and mechanisms of TSX X-Band data in a low Arctic ecosystem.

4.10 Acknowledgments

The authors want to thank the German Helmholtz Alliance Earth System Dynamics (EDA) for funding of this project and access to the TSX datasets. Samuel Stettner and Hugues Lantuit were additionally supported through HGF COPER, Annett Bartsch through the European Space Agency project DUE GlobPermafrost (Contract Number 4000116196/15/I-NB) and Birgit Heim through the Helmholtz program for Regional Climate Change REKLIM. Isla Myers-Smith was funded through NERC through the ShrubTundra

(NE/M016323/1) standard grant. We thank the Team Shrub field research crews in 2016 and 2017 and Samuel and Edward McLeod for assistance with the installation and maintenance of the phenocam monitoring network. The authors want to the rangers of Herschel Island – Qikiqtaruk Territorial Park and the Aurora Research Institute as well as the AWI logistics department for making the field work in this remote area possible. We thank the Inuvialuit People for the opportunity to conduct research on their traditional lands.

Chapter 5

5 SYNTHESIS

The main objective of this thesis was to explore the applicability of time series data acquired by the German synthetic aperture radar (SAR) satellite Terra-SAR-X (TSX) to monitor rapid changes of Arctic permafrost environments associated with climate change. Unique three-year time series of TSX X-Band data in multiple polarizations and orbital passes were available for long-term study sites in the central Lena Delta, Russia and on Qikiqtaruk (Herschel Island), Canada. These time series were made available through efforts of the Polar Space Task Group (PSTG). The PSTG together with the permafrost research community identifies requirements as well as novel approaches to adequately monitor rapid changes of Arctic permafrost landscapes. The study of permafrost and snow by a complementary and concurrent use of SAR and optical satellite missions has been identified as strategic priorities of the PSTG (PSTG, 2017).

The three main research chapters of the thesis each focus on different components of terrestrial Arctic change and how the application of SAR remote sensing, optical remote sensing and in-situ data can be used in a complementary way to better understand seasonal trends. The findings of this thesis demonstrate that TSX X-Band data can be used in a versatile and effective way to monitor permafrost degradation (Chapter 2), snow cover (Chapter 3), and vegetation phenology (Chapter 4), the first two of which have been identified as essential climate variables of the terrestrial domain by the Global Climate Observing System (Sessa and Dolman, 2008).

Chapter 2 - Rapid permafrost disturbance: In this chapter the independence of TSX from cloud cover and solar illumination in combination with high temporal and spatial resolution facilitated a novel three year, inter- and intra-annual analysis of rapid permafrost disturbance at an ice-rich riverbank. The combined use of established optical remote sensing methods with very high temporal resolution observations from in-situ time-lapse cameras revealed consistent rates of erosion of ice-rich permafrost throughout the annual erosional period.

Chapter 3 - Snowmelt dynamics: A three year, 11-day time series of fractional snow cover in small catchments on Qikiqtaruk was generated using TSX X-Band data. The dense time series data were validated by in-situ snowmelt observations from time-lapse imagery and filled an observational gap present in optical time series data. Depending on catchment

topography, different snowmelt regimes were detected by TSX and confirmed with in-situ measurements.

Chapter 4 - Arctic tundra vegetation phenology: This initial exploration of the potential of TSX to detect vegetation phenology in different ecosystem units outlined the complex interactions between incidence angle, surface conditions and vegetation type. In general, the backscatter intensity corresponded to the mean vegetation height between ecosystem units. A pattern of increasing backscatter over the growing season was observed in areas with tall shrubs and dry surface conditions as well as low-lying areas with high surface moisture and graminoid vegetation. The results highlight the importance of in-situ and a priori knowledge and suggest the utility of TSX to monitor vegetation phenology is limited to dry, tall shrub areas.

5.1 RAPID PERMAFROST DISTURBANCE

Degradation of permafrost has both social and environmental implications ranging from hazards to local infrastructure to the release of ancient carbon and methane (Grosse et al., 2011; Kääb, 2008). At the local scale, monitoring tools with adequate spatial resolution are needed to support northern communities in adaption planning (AMAP, 2012). At the regional scale, monitoring of rapid permafrost degradation at an intra-annual scale is needed in order to understand seasonal erosion dynamics. Annual rates of erosion from eroding riverbanks and coastal cliffs derived from optical satellite data exist for selected Arctic regions (Günther et al., 2013; Kanevskiy et al., 2016; Lantuit and Pollard, 2008). However, data on an intra-annual scale are scarce due to persistent cloud cover limiting our understanding of the seasonality of permafrost degradation. The high spatial and temporal resolution of TSX offered a unique opportunity to study rapid permafrost degradation at an intra-annual scale and could be used to help northern communities monitor the changes they are facing in the context of rapid Arctic change. Projects that combine remote sensing data with field observations from northern communities in order to support decision making already exist for sea ice applications in northern Canada (https://arcticeider.com/, https://www.smartice.org/)

This thesis provides novel insights into the erosion of an ice-rich riverbank in the central Lena Delta, Siberia. The results show that erosion occurs at a consistent rate throughout the erosional season (T > 0°C). Landscape topography and resulting illumination effects in SAR data known as foreshortening were exploited to delineate cliff top lines of a rapidly retreating ice-rich permafrost cliff at 22 day intervals. The foreshortening effect of the HH

polarized X-Band backscatter data caused by the tilted cliff surface towards the sensor clearly delineated the transition between low backscatter of the upland tundra surface and high backscatter of the bare ground cliff areas. Cliff-top retreat within and between three years was tracked throughout the erosion season at a temporal resolution rarely achieved by optical sensors. The TSX-derived erosion rates and net annual erosion were very similar to corresponding time-lapse imagery and optical very high spatial resolution satellite imagery, respectively, as well as annual erosion rates from similar locations in the Artic (Kanevskiy et al., 2016; Payne et al., 2018; Walker et al., 1987).

Additionally, intra-annual patterns of erosion did not appear to be influenced by seasonal changes in temperature or hydrology (Chapter 1, Stettner et al. (2017)). The high temporal resolution of permafrost disturbance data provided the opportunity to apply a linear mixed model approach to explore the impact of climatic parameters (thawing degree days, air temperature and precipitation) on the observed erosional patterns. The well-established relationship between erosion and temperature was confirmed, however at an annual, not intra-annual scale suggesting a thermal lag or insulation to seasonal changes in temperature. Increased annual erosion was also observed when precipitation occurred concurrently with above average annual precipitation (Stettner et al., 2017).

Abrupt changes of permafrost landscapes such as cliff erosion are one of the greatest hazards in a warming Arctic. The unique dataset of ice-rich riverbank erosion derived from TSX X-Band backscatter time series data provided an opportunity to examine the intra-annual patterns of rapid disturbance at an ice-rich Arctic site. High temporal and spatial monitoring of these processes provides crucial baseline data to identify erosion dynamics and forcing mechanisms. In this thesis I present an effective way of using HH polarized X-Band backscatter data to complement existing optical and field data methods for the monitoring of rapid permafrost degradation.

5.2 SNOWMELT DYNAMICS

Many ecological processes in Arctic ecosystems are influenced by snowmelt including hydrological discharge, vegetation phenology, and soil microbial activity (Bjorkman et al., 2015a; Schimel et al., 2004; Woo et al., 2000). Snow also acts as an important thermal regulator, insulating permafrost soils from cold winter and warm spring temperatures (Zhang, 2005). On the pan-arctic scale a decrease in spring snow cover and earlier snowmelt has been recorded in the last decades though current and future changes are characterized by high spatial heterogeneity highlighting the need for detailed, catchment

level analyses (Brown and Robinson, 2011). Monitoring changes in the extent, and duration of snow cover as well as the timing of snowmelt provides important information on the thermal ground regime, shifts in hydrological regimes, heterotrophic respiration, and vegetation phenology and composition. During snowmelt, available water within the snowpack strongly attenuates the backscattered microwave signal across all wavelengths resulting in dark areas in SAR intensity images (Stiles and Ulaby, 1980). This effect has been used to map wet snow cover with SAR data acquired in different wavelength(Nagler and Rott, 2000; Schellenberger et al., 2012).

In this thesis, I used TSX backscatter data from multiple orbits and with multiple polarizations to generate maps of snow cover extent (SCE) and to extract fractional snow cover (FSC) time series in the snowmelt period of three years in a low-Arctic ecosystem in the Western Canadian Arctic. The results clearly showed that VH polarized X-Band data performed best in deriving SCE maps. The TSX derived FSC time series significantly increased the temporal resolution of FSC data during the snowmelt season and provided valuable insights into snowmelt dynamics on Qikiqtaruk previously not available. The TSX observations revealed rapid melt in catchments with a greater contribution of upland terrain compared to catchments with a high contribution of stream valleys with long-lasting snow patches in protected areas. Interestingly, TSX was able to detect these long-lasting snow patches longer than Landsat 8 which, due to a combination of spatial scale and lower reflectance of old snow in the visible electromagnetic spectrum, could not detect snow patches later in the snowmelt season.

TSX captured the onset and evolution of snowmelt as well as long lasting snow patches that are ecologically important landscape features and represent the end of seasonal snow cover. The results also showed that due to the sensitivity to wet snow, TSX is able to detect short duration snow events when they occur concurrently with acquisitions.

5.3 Arctic tundra vegetation phenology

The phenology of Arctic vegetation is a sensitive indicator of Arctic change as the onset is dictated by snowmelt (Richardson et al., 2013). Traditionally, vegetation phenology has been monitored by field-based methods involving visits to individual plants at two to three day intervals such as sampling protocols outlined by the International Tundra Experiment (ITEX) (Henry and Molau, 1997). More recently, networks of time-lapse digital cameras have been established to monitor vegetation phenology from extracted greenness values including Arctic locations (PHENOCAM, https://phenocam.sr.unh.edu/webcam/).

Though pan-Arctic scale monitoring using data from the Moderate Resolution Imaging Spectroradiometer (MODIS) is available (Bhatt et al., 2010), dense time series that resolve seasonal dynamics on the landscape scale are scarce because phenological monitoring with spaceborne optical remote sensing faces the same challenges as previously outlined (e.g. cloud cover, solar illumination).

The sensitivity of TSX X-Band to the vegetation layer due to its short wavelength was the basis of the novel approach to assess the capabilities of TSX backscatter and coherence to track phenological changes of Arctic vegetation from early to peak season. TSX data were compared to greenness data from in-situ time-lapse digital cameras. With increasing greenness, used as a proxy for increasing vegetation volume, backscatter concurrently increased in ecological classes that were dominated by tall shrub vegetation and dry surface conditions. The observed increase of backscatter in classes with shrub vegetation was likely related to changes in the structure of the surface as leaf area increased. In ecological classes with lower vegetation and higher bare ground contribution decreasing backscatter trends were observed over the time of vegetation green-up and peak phenology, likely influenced by a decreasing surface wetness signal instead of a vegetation structure signal. The decreasing trend indicates a drying of the prostrate tundra vegetation surfaces throughout green-up and peak season. The applicability of TSX for direct estimation of phenology in a diversity of ecological classes on Qikiqtaruk was limited but the results in tall shrub areas warrants further investigation. In the context of Arctic shrub expansion the techniques used in this thesis could be promising for future applications of X-Band SAR for shrub phenology.

5.4 Seasonality and complementarity of TSX

In this thesis I developed applications of TSX time series complementary to optical, and field based data to extract seasonal dynamics of ecosystem components in Arctic permafrost environments. Seasonality is a sensitive indicator of environmental change (Denton et al., 2005). Shifts in seasonal patterns of ecosystem processes can be an indicator of climatic changes but monitoring this seasonality at an adequate temporal frequency can be challenging due to its complexity and a scarcity of data sources. The analysis of TSX X-Band time series from multiple orbits and polarizations at the PSTG long-term-monitoring sites of the central Lena Delta and Qikiqtaruk revealed seasonality signals of multiple ecosystem components on the catchment scale (Figure 5-1).

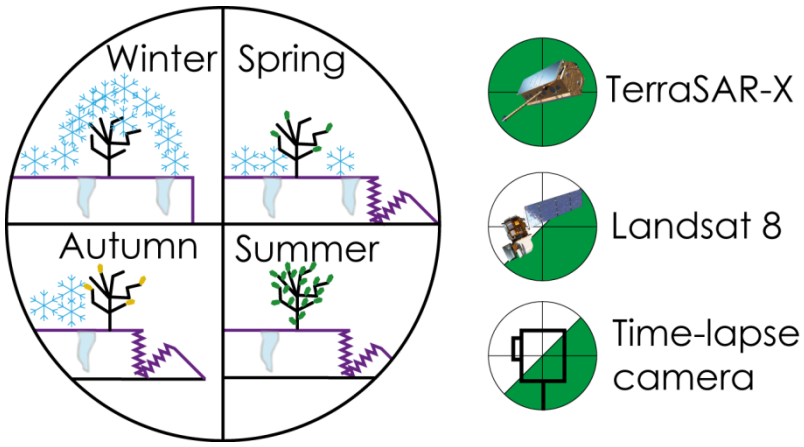

Figure 5-1: Schematic of Arctic seasonality illustrating selected ecosystem components and monitoring instruments. In winter the ground is snow covered, vegetation activity is low and no erosion occurs; in spring snow cover decreases, plant phenology begins, and permafrost degradation is possible. In summer vegetation phenology peaks and permafrost degradation is ongoing. In autum vegetations starts to senescence and snow cover starts to develop, permafrost degagradation still occurs. TSX is operational throughout all cycles (Full green cirlce) while optical Landsat 8 and time-lapse camera are limited to the time with adequate solar illumination (half green circle).

The concurrent use of established optical satellite data methods and cost effective in-situ time-lapse cameras increased the validity of the results and facilitated data interpretation. The in-situ time-lapse camera data were extremely useful in order to understand the small-scale processes of different locations. Noise was an inherent element in the SAR data and the ground reference data provided a better understanding of the observed SAR signals. In Chapter 2 I mapped erosion from high spatial resolution optical data to validate the annual cliff top retreat from TSX over the three-year time span while I used the time-lapse data to verify the intra-annual rates of erosion. In Chapter 3 the snow detection capabilities of TSX were limited to the time of snowmelt (wet snow), which made the Landsat 8 a valuable source for dry snow mapping in addition to being used as a validation of the TSX SCE results. The derived snow maps and fractional snow cover time series from the different data sources were fully complementary. The reference data from optical remote sensing and time-lapse cameras were not only used to validate monitoring of cliff-top erosion and wet snow mapping but also as a complementary data source resulting in a valuable final data product.

5.5 Limitations and technical considerations

The methods and workflows developed in this thesis are novel approaches to study seasonal aspects of rapid Arctic change and represent first attempts to assess the

applicability of TSX to high spatiotemporal resolution monitoring of rapid permafrost disturbance, snowmelt and vegetation phenology. Although these processes were successfully monitored using TSX, some limitations have to be considered by users of the presented methods and applications.

The interpretation of SAR backscatter and coherence presents challenges because of the inherent speckle effect and sensitivity of the signal to surface roughness, vegetation, moisture and the thermal state of the ground. Filtering of SAR data is necessary in most cases to smooth the effect of speckle. This is done by applying a combination of multilooking and image filters, depending on the application. Multilooking and SAR image speckle filters result in a loss of spatial resolution. In order to preserve the needed high spatial resolution of TSX for the application in Chapter 2, I did not apply filtering techniques. Tests of existing edge preserving speckle filters that reduce speckle and maintain the spatial resolution were computationally intensive and introduced errors to the delineated cliff-top lines. The application of advanced filtering techniques as well as a dynamic approach of adaptive thresholding could improve the delineation of cliff top lines in the future and help to overcome current limitations at complex cliff geometries.

The sensitivity of TSX to the frozen state of the ground was a source of variability when monitoring permafrost disturbance and snowmelt. A reduction of backscatter due to frozen ground reduced the contrast between the tundra surface and cliff surface and resulted in less successful cliff top delineation. Precipitation events also impacted successful delineations of the cliff top particularly at locations with complex cliff geometry where water was channelized and bare ground was saturated. The early season was challenging for cliff top retrieval because remaining wet snow in protected areas along the cliff top lowered the backscatter intensity and reduced the contrast between tundra and cliff surface.

The timing of acquisition was an additional source of error. Early morning acquisitions introduced errors in the snow cover retrieval due to refreezing snow layers resulting in no snow detection, drastically lowering estimated snow cover. This emphasizes the importance of the time of day for the acquisition planning for wet snow mapping applications. Acquisitions with precipitation on the same or following day showed increases in backscatter over single tundra patches and influenced the interpretation of cliff top delineation in the Lena Delta study site.

5.6 KEY FINDINGS AND OUTLOOK

In this thesis I demonstrate that dense time series of TSX are a useful and complementary remote sensing tool to understand rapid and seasonal changes in Arctic environments. I successfully applied TSX X-Band data to monitor permafrost degradation, snow cover, and vegetation phenology at high spatial and temporal resolution.

The key findings of the thesis are the following:

- TSX is capable of monitoring rapid permafrost degradation at intra-seasonal scales providing new insights into the seasonality of the process at a landscape scale.
- TSX fills a gap in monitoring the rapid and highly dynamic phenomenon of snowmelt at the small catchment scale and provides new opportunities for many applications such as hydrological modelling, local system erosion modelling and vegetation studies.
- Backscatter and coherence time series of TSX are capable of tracking phenological emergence and expansion of vegetation of tall shrub vegetation in dry areas.

The potential of the complementarity of SAR to optical remote sensing, and cost effective in-situ time-lapse camera has been clearly demonstrated in this thesis and provides a framework to improve existing and future data products. In cooperation with northern communities and existing time-lapse camera networks in the Arctic, the presented workflows of all chapters could be expanded to a regional level. In particular, the demonstrated capability of TSX to detect late lying snow patches should be further investigated as it improves SCE maps of late snowmelt. In addition, the Starring Spotlight mode of TSX with a spatial resolution up to 40 cm has high potential for studies of Arctic vegetation. It would be interesting to investigate if single vegetation communities can be differentiated. More detailed stages of phenology could be extracted for selected vegetation communities and validated with ground measurements. Also the use of SAR polarimetry could allow the derivation of vegetation phenology parameters.

REFERENCES

AMAP, 2018. Arctic Monitoring and Assessment Programme (AMAP) [WWW Document]. URL https://www.amap.no/ (accessed 5.25.18).

AMAP, 2012. Arctic Climate Issues 2011: Changes in Arctic Snow, Water, Ice and Permafrost. SWIPA 2011 Overview Report. Arctic Monitoring and Assessment Programme (AMAP). Oslo, Norway.

Andresen, C.G., Tweedie, C.E., Lougheed, V.L., 2018. Climate and nutrient effects on Arctic wetland plant phenology observed from phenocams. Remote Sens. Environ. 205, 46–55. https://doi.org/10.1016/J.RSE.2017.11.013

Antonova, S., Duguay, C., Kääb, A., Heim, B., Langer, M., Westermann, S., Boike, J., 2016a. Monitoring Bedfast Ice and Ice Phenology in Lakes of the Lena River Delta Using TerraSAR-X Backscatter and Coherence Time Series. Remote Sens. 8, 903. https://doi.org/10.3390/rs8110903

Antonova, S., Kääb, A., Heim, B., Langer, M., Boike, J., 2016b. Spatio-temporal variability of X-band radar backscatter and coherence over the Lena River Delta, Siberia. Remote Sens. Environ. 182, 169–191. https://doi.org/10.1016/j.rse.2016.05.003

Antonova, S., Sudhaus, H., Strozzi, T., Zwieback, S., Kääb, A., Heim, B., Langer, M., Bornemann, N., Boike, J., 2018. Thaw Subsidence of a Yedoma Landscape in Northern Siberia, Measured In Situ and Estimated from TerraSAR-X Interferometry. Remote Sens. https://doi.org/10.3390/rs10040494

Aré, F.E., 1988. Thermal abrasion of sea coasts (part I). Polar Geogr. Geol. 12, 1–1. https://doi.org/10.1080/10889378809377343

Baghdadi, N., Zribi, M., Loumagne, C., Ansart, P., Anguela, T.P., 2008. Analysis of TerraSAR-X data and their sensitivity to soil surface parameters over bare agricultural fields. Remote Sens. Environ. 112, 4370–4379. https://doi.org/10.1016/j.rse.2008.08.004

Ballantyne, C.K., 1978. The Hydrologic Significance of Nivation Features in Permafrost Areas. Geogr. Ann. Ser. A, Phys. Geogr. 60, 51–54. https://doi.org/10.1080/04353676.1978.11879963

Banks, S., Ullmann, T., Roth, A., Schmitt, A., Dech, S., King, D., 2013. Classification of Arctic coastal land covers with Polarimetric SAR data, in: Radar Conference (RADAR), 2013 IEEE. IEEE, pp. 1–6. https://doi.org/10.1109/RADAR.2013.6586059

Barker, T., 2007. Climate Change 2007: An Assessment of the Intergovernmental Panel on Climate Change. Change, Synthesis Report 446, 12–17. https://doi.org/10.1256/004316502320517344

Bartsch, A., 2014. Requirements for Monitoring of Permafrost in Polar Regions [White paper], WMO-Polar Space task group meeting.

Bartsch, A., Allard, M., Biskaborn, B.K., Burba, G., Christiansen, H.H., Duguay, C.R., Grosse, G., Günther, F., Heim, B., Högström, E., Kääb, A., Keuper, F., Lanckman, J.-P., Lantuit, H., Lauknes, T.R., Leibman, M.O., Liu, L., Morgenstern, A., Necsoiu, M.,

Overduin, P.P., Pope, A., Sachs, T., Séjourné, A., Streletskiy, D.A., Strozzi, T., Ullmann, T., Ullrich, M.S., Vieira, G., Widhalm, B., 2014. Permafrost longterm monitoring sites (Arctic and Antarctic). Suppl. to Bartsch, A al. Requir. Monit. Permafr. polar Reg. - A community white Pap. response to WMO Polar Sp. Task Gr. (PSTG), Version 4, 2014-10-09. Austrian Polar Res. Institute, Vienna, Austria,. https://doi.org/10.1594/PANGAEA.847003

Bartsch, A., Annett, 2010. Ten Years of SeaWinds on QuikSCAT for Snow Applications. Remote Sens. 2, 1142–1156. https://doi.org/10.3390/rs2041142

Bartsch, A., Höfler, A., Kroisleitner, C., Trofaier, A., 2016. Land Cover Mapping in Northern High Latitude Permafrost Regions with Satellite Data: Achievements and Remaining Challenges. Remote Sens. 8, 979. https://doi.org/10.3390/rs8120979

Bartsch, A., Kidd, R.A., Wagner, W., Bartalis, Z., 2007. Temporal and spatial variability of the beginning and end of daily spring freeze/thaw cycles derived from scatterometer data. Remote Sens. Environ. 106, 360–374. https://doi.org/http://dx.doi.org/10.1016/j.rse.2006.09.004

Bates, D., Mächler, M., Bolker, B., Walker, S., 2014. Fitting linear mixed-effects models using lme4. arXiv Prepr. arXiv1406.5823.

Beamish, A.L., Coops, N.C., Hermosilla, T., Chabrillat, S., Heim, B., 2018. Monitoring pigment-driven vegetation changes in a low-Arctic tundra ecosystem using digital cameras. Ecosphere 9, e02123. https://doi.org/10.1002/ecs2.2123

Beamish, A.L., Nijland, W., Edwards, M., Coops, N.C., Henry, G.H.R., 2016. Phenology and vegetation change measurements from true colour digital photography in high Arctic tundra. Arct. Sci. 2, 33–49. https://doi.org/10.1139/as-2014-0003

Bhatt, U., Walker, D., Raynolds, M., Bieniek, P., Epstein, H., Comiso, J., Pinzon, J., Tucker, C., Polyakov, I., 2013. Recent Declines in Warming and Vegetation Greening Trends over Pan-Arctic Tundra. Remote Sens. 5, 4229–4254. https://doi.org/10.3390/rs5094229

Bhatt, U.S., Walker, D.A., Raynolds, M.K., Comiso, J.C., Epstein, H.E., Jia, G., Gens, R., Pinzon, J.E., Tucker, C.J., Tweedie, C.E., 2010. Circumpolar Arctic tundra vegetation change is linked to sea ice decline. Earth Interact. 14, 1–20. https://doi.org/10.1175/2010EI315.1

Billings, W.D., Bliss, L.C., 1959. An alpine snowbank environment and its effects on vegetation, plant development, and productivity. Ecology 40, 388–397. https://doi.org/10.2307/1929755

Billings, W.D., Mooney, H.A., 1968. The ecology of Arctic plants, Biological Reviews. Wiley/Blackwell (10.1111). https://doi.org/10.1111/j.1469-185X.1968.tb00968.x

Bivand, R., Keitt, T., Rowlingson, B., 2014. rgdal: Bindings for the geospatial data abstraction library. R Packag. version 0.8-16.

Bjorkman, A.D., Elmendorf, S.C., Beamish, A.L., Vellend, M., Henry, G.H.R., 2015a. Contrasting effects of warming and increased snowfall on Arctic tundra plant phenology over the past two decades. Glob. Chang. Biol. 21, 4651–4661.

Bjorkman, A.D., Elmendorf, S.C., Beamish, A.L., Vellend, M., Henry, G.H.R., 2015b.

Contrasting effects of warming and increased snowfall on Arctic tundra plant phenology over the past two decades. Glob. Chang. Biol. 21, 4651–4661. https://doi.org/10.1111/gcb.13051

Blasco, S.M., Fortin, G., Hill, P.R., O'Connor, M.J., Brigham-Grette, J., 1990. The late Neogene and Quaternary stratigraphy of the Canadian Beaufort continental shelf, in: The Arctic Ocean Region. Geological Society of America, United Sates, pp. 491–502. https://doi.org/10.1130/DNAG-GNA-L.491

Boike, J., Kattenstroth, B., Abramova, K., Bornemann, N., Chetverova, A., Fedorova, I., Frob, K., Grigoriev, M., Gruber, M., Kutzbach, L., Langer, M., Minke, M., Muster, S., Piel, K., Pfeiffer, E.M., Stoof, G., Westermann, S., Wischnewski, K., Wille, C., Hubberten, H.W., 2013. Baseline characteristics of climate, permafrost and land cover from a new permafrost observatory in the Lena River Delta, Siberia (1998-2011). Biogeosciences 10, 2105–2128. https://doi.org/DOI 10.5194/bg-10-2105-2013

Brooks, P.D., Grogan, P., Templer, P.H., Groffman, P., Öquist, M.G., Schimel, J., 2011. Carbon and Nitrogen Cycling in Snow-Covered Environments. Geogr. Compass 5, 682–699. https://doi.org/10.1111/j.1749-8198.2011.00420.x

Brown, R.D., Robinson, D.A., 2011. Northern Hemisphere spring snow cover variability and change over 1922–2010 including an assessment of uncertainty. Cryosph. 5, 219–229. https://doi.org/10.5194/tc-5-219-2011

Brown, T.B., Hultine, K.R., Steltzer, H., Denny, E.G., Denslow, M.W., Granados, J., Henderson, S., Moore, D., Nagai, S., SanClements, M., Sánchez-Azofeifa, A., Sonnentag, O., Tazik, D., Richardson, A.D., 2016. Using phenocams to monitor our changing Earth: toward a global phenocam network. Front. Ecol. Environ. 14, 84–93. https://doi.org/10.1002/fee.1222

Burn, C.R., 2012. Herschel Island Qikiqtaryuk-a Natural and Cultural History of Yukon's Arctic Island. Calgary, Alberta.

Burn, C.R., 2012. Herschel Island Qikiqtaryuk - a Natural and Cultural History of Yukon's Arctic Island, in: Herschel Island Qikiqtaryuk - a Natural and Cultural History of Yukon's Arctic Island. Calgary, Alberta, pp. 48–53.

Burn, C.R., Zhang, Y., 2009. Permafrost and climate change at Herschel Island (Qikiqtaruq), Yukon Territory, Canada. J. Geophys. Res. 114, F02001. https://doi.org/10.1029/2008JF001087

Clark, M.P., Hendrikx, J., Slater, A.G., Kavetski, D., Anderson, B., Cullen, N.J., Kerr, T., Örn Hreinsson, E., Woods, R.A., 2011. Representing spatial variability of snow water equivalent in hydrologic and land-surface models: A review. Water Resour. Res. 47. https://doi.org/10.1029/2011WR010745

Cleland, E.E., Chuine, I., Menzel, A., Mooney, H.A., Schwartz, M.D., 2007. Shifting plant phenology in response to global change. Trends Ecol. Evol. 22, 357–365. https://doi.org/10.1016/j.tree.2007.04.003

Cook, B.I., Wolkovich, E.M., Davies, T.J., Ault, T.R., Betancourt, J.L., Allen, J.M., Bolmgren, K., Cleland, E.E., Crimmins, T.M., Kraft, N.J.B., 2012. Sensitivity of spring phenology to warming across temporal and spatial climate gradients in two independent databases. Ecosystems 15, 1283–1294.

References

Costard, F., Gautier, E., Brunstein, D., Hammadi, J., Fedorov, A., Yang, D., Dupeyrat, L., 2007. Impact of the global warming on the fluvial thermal erosion over the Lena river in Central Siberia. Geophys. Res. Lett. 34. https://doi.org/doi:10.1029/2007GL030212

Costard, F., Gautier, E., Fedorov, a, Konstantinov, P., Dupeyrat, L., 2014. An Assessment of the Erosion Potential of the Fluvial Thermal Process during Ice Breakups of the Lena River (Siberia). Permafr. Periglac. Process. 25, 162–171. https://doi.org/10.1002/ppp.1812

Couture, N.J., Pollard, W.H., 2017. A Model for Quantifying Ground-Ice Volume , Yukon Coast , Western Arctic Canada. https://doi.org/10.1002/ppp.1952

Crawford, C.J., Manson, S.M., Bauer, M.E., Hall, D.K., 2013. Multitemporal snow cover mapping in mountainous terrain for Landsat climate data record development. Remote Sens. Environ. 135, 224–233. https://doi.org/10.1016/J.RSE.2013.04.004

De Krom, V., 1990. Retrogressive thaw slumps and active layer slides on Herschel Island, Yukon. Unpubl. M. Sc. Thesis, McGill Univ. Montréal, Quebec.

Denton, G.H., Alley, R.B., Comer, G.C., Broecker, W.S., 2005. The role of seasonality in abrupt climate change. Quat. Sci. Rev. 24, 1159–1182. https://doi.org/10.1016/j.quascirev.2004.12.002

Dietz, A.J., Kuenzer, C., Gessner, U., Dech, S., Juergen, A., Kuenzer, C., Gessner, U., Dech, S., Dietz, A.J., Kuenzer, C., Gessner, U., 2012. Remote sensing of snow – a review of available methods 33, 4094–4134. https://doi.org/10.1080/01431161.2011.640964

DLR, 2007. TerraSAR-X Ground Segment Level 1b Product Format Specification. TX-GS-DD-3307. V. 1.3. Dtsch. Zent. für Luft- und Raumfahrt. Clust. Appl. Remote Sensing. TerraSAR-X Gr. Segm. 257.

Douglas, D.H., Peucker, T.K., 1973. Algorithms for the reduction of the number of points required to represent a digitized line or its caricature. Cartogr. Int. J. Geogr. Inf. Geovisualization 10, 112–122.

Duguay, Y., Bernier, M., Lévesque, E., Tremblay, B., 2015. Potential of C and X Band SAR for Shrub Growth Monitoring in Sub-Arctic Environments. Remote Sens. 7, 9410–9430. https://doi.org/10.3390/rs70709410

Dunnington, D., 2018. rclimateca: Fetch Climate Data from Environment Canada. R package version 1.0.2.

Dupeyrat, L., Costard, F., Randriamazaoro, R., Gailhardis, E., Gautier, E., Fedorov, A., 2011. Effects of Ice Content on the Thermal Erosion of Permafrost: Implications for Coastal and Fluvial Erosion. Permafr. Periglac. Process. 22, 179–187. https://doi.org/Doi 10.1002/Ppp.722

Eineder, M., Fritz, T., Mittermayer, J., Roth, A., Börner, E., Breit, H., Bräutigam, B., Kraus, T., 2008. TerraSAR-X Basic Product Specification Document.

Eischeid, I., 2015. Mapping of soil organic carbon and nitrogen in two small adjacent Arctic watersheds on Herschel Island, Yukon Territory. University of Hohenheim.

Elmendorf, S.C., Henry, G.H.R., Hollister, R.D., Björk, R.G., Bjorkman, A.D., Callaghan, T. V, Collier, L.S., Cooper, E.J., Cornelissen, J.H.C., Day, T.A., 2012. Global assessment of experimental climate warming on tundra vegetation: heterogeneity over space and

time. Ecol. Lett. 15, 164–175. https://doi.org/10.1111/j.1461-0248.2011.01716.x

Englhart, S., Keuck, V., Siegert, F., 2011. Aboveground biomass retrieval in tropical forests — The potential of combined X- and L-band SAR data use. Remote Sens. Environ. 115, 1260–1271. https://doi.org/10.1016/J.RSE.2011.01.008

Eriksen, H.Ø., Lauknes, T.R., Larsen, Y., Corner, G.D., Bergh, S.G., Dehls, J., Kierulf, H.P., 2017. Visualizing and interpreting surface displacement patterns on unstable slopes using multi-geometry satellite SAR interferometry (2D InSAR). Remote Sens. Environ. 191, 297–312. https://doi.org/10.1016/j.rse.2016.12.024

ESA, 2017. SNAP - ESA Sentinel Application Platform v.3.0 [WWW Document]. URL http://step.esa.int (accessed 11.20.17).

Fedorova, I., Chetverova, a, Bolshiyanov, D., Makarov, a, Boike, J., Heim, B., Morgenstern, a, Overduin, P.P., Wegner, C., Kashina, V., Eulenburg, a, Dobrotina, E., Sidorina, I., 2015. Lena Delta hydrology and geochemistry: long-term hydrological data and recent field observations. Biogeosciences 12, 345–363. https://doi.org/10.5194/bg-12-345-2015

Floricioiu, D., Rott, H., 2001. Seasonal and short-term variability of multifrequency, polarimetric radar backscatter of Alpine terrain from SIR-C/X-SAR and AIRSAR data. IEEE Trans. Geosci. Remote Sens. 39, 2634–2648. https://doi.org/10.1109/36.974998

Floricioiu, D., Rott, H., 2001. Seasonal and short-term variability of multifrequency, polarimetric radar backscatter of alpine terrain from SIR-C/X-SAR and AIRSAR data. IEEE Trans. Geosci. Remote Sens. 39, 2634–2648. https://doi.org/10.1109/36.974998

Fontanelli, G., Paloscia, S., Zribi, M., Chahbi, A., 2013. Sensitivity analysis of X-band SAR to wheat and barley leaf area index in the Merguellil Basin. Remote Sens. Lett. 4, 1107–1116. https://doi.org/10.1080/2150704X.2013.842285

Foody, G.M., 2002. Status of land cover classification accuracy assessment. Remote Sens. Environ. 80, 185–201. https://doi.org/10.1016/S0034-4257(01)00295-4

Fraser, C.S., Ravanbakhsh, M., 2009. Georeferencing performance of Geoeye-1, in: Photogrammetric Engineering and Remote Sensing. pp. 634–638.

French, H.M., 2007. The Periglacial Environment, Third Edition, Third Edit. ed. John Wiley & Sons Ltd, Hoboken, NJ.

Fritz, M., Opel, T., Tanski, G., Herzschuh, U., Meyer, H., Eulenburg, A., Lantuit, H., 2015. Dissolved organic carbon (DOC) in Arctic ground ice. Cryosph. Discuss. 9, 77–114. https://doi.org/10.5194/tcd-9-77-2015

Fritz, M., Wetterich, S., Schirrmeister, L., Meyer, H., Lantuit, H., Preusser, F., Pollard, W.H., 2012. Eastern Beringia and beyond: Late Wisconsinan and Holocene landscape dynamics along the Yukon Coastal Plain, Canada. Palaeogeogr. Palaeoclimatol. Palaeoecol. 319–320, 28–45. https://doi.org/10.1016/J.PALAEO.2011.12.015

Frost, V.S., Stiles, J.A., Shanmugan, K.S., Holtzman, J.C., 1982. A model for radar images and its application to adaptive digital filtering of multiplicative noise. IEEE Trans. Pattern Anal. Mach. Intell. 157–166. https://doi.org/10.1109/TPAMI.1982.4767223

GISTEMP Team, 2018. GISS surface temperature analysis (GISTEMP) [WWW Document]. NASA Goddard Inst. Sp. Stud. URL https://data.giss.nasa.gov/gistemp/ (accessed

6.16.18).

Godin, E., Fortier, D., Coulombe, S., 2014. Effects of thermo-erosion gullying on hydrologic flow networks, discharge and soil loss. Environ. Res. Lett. 9, 105010. https://doi.org/10.1088/1748-9326/9/10/105010

Gorrab, A., Zribi, M., Baghdadi, N., Mougenot, B., Fanise, P., Chabaane, Z., 2015. Retrieval of Both Soil Moisture and Texture Using TerraSAR-X Images. Remote Sens. 7, 10098–10116. https://doi.org/10.3390/rs70810098

Green, K., Pickering, C.M., 2009. The decline of snowpatches in the Snowy Mountains of Australia: importance of climate warming, variable snow, and wind. Arctic, Antarct. Alp. Res. 41, 212–218. https://doi.org/10.1657/1938-4246-41.2.212

Grosse, G., Harden, J., Turetsky, M., Mcguire, A.D., Camill, P., Tarnocai, C., Frolking, S., Schuur, E.A.G., Jorgenson, T., Marchenko, S., Romanovsky, V., Wickland, K.P., French, N., Waldrop, M., Chavez, L.B., Striegl, R.G., 2011. Vulnerability of high - latitude soil organic carbon in North America to disturbance 116, 1–23. https://doi.org/10.1029/2010JG001507

Grosse, G., Robinson, J.E., Bryant, R., Taylor, M.D., Harper, W., DeMasi, A., Kyker-Snowman, E., Veremeeva, A., Schirrmeister, L., Harden, J., 2013. Distribution of late Pleistocene ice-rich syngenetic permafrost of the Yedoma Suite in east and central Siberia, Russia. US Geol. Surv. Open File Rep. 2013, 1–37.

Grosse, G., Schirrmeister, L., Malthus, T.J., 2006. Application of Landsat-7 satellite data and a DEM for the quanti fi cation of thermokarst-affected terrain types in the periglacial Lena – Anabar coastal lowland 51–68.

Günther, F., Overduin, P.P., Sandakov, A. V, Grosse, G., Grigoriev, M.N., 2013. Short- and long-term thermo-erosion of ice-rich permafrost coasts in the Laptev Sea region. Biogeosciences 10, 4297–4318. https://doi.org/DOI 10.5194/bg-10-4297-2013

Günther, F., Overduin, P.P., Sandakov, A. V, Grosse, G., Grigoriev, M.N., 2012. Thermo-erosion along the Yedoma Coast of the Buor Khaya Peninsula, Laptev Sea, East Siberia. Proc. 10th Int. Conf. Permafr. 2, 137–142.

Hall, D.K., Riggs, G.A., Salomonson, V. V, 1995. Development of methods for mapping global snow cover using moderate resolution imaging spectroradiometer data. Remote Sens. Environ. 54, 127–140. https://doi.org/10.1016/0034-4257(95)00137-P

Hall, D.K., Riggs, G.A., Salomonson, V. V, DiGirolamo, N.E., Bayr, K.J., 2002. MODIS snow-cover products. Remote Sens. Environ. 83, 181–194.

Hansen, J., Ruedy, R., Sato, M., Lo, K., 2010. Global surface temperature change. Rev. Geophys. 48. https://doi.org/10.1029/2010RG000345

Henry, G.H.R., Molau, U., 1997. Tundra plants and climate change: the International Tundra Experiment (ITEX). Glob. Chang. Biol. 3, 1–9. https://doi.org/10.1111/j.1365-2486.1997.gcb132.x

Hinzman, L.D., Kane, D.L., Benson, C.S., Everett, K.R., 1996. Energy Balance and Hydrological Processes in an Arctic Watershed. Springer, Berlin, Heidelberg, pp. 131–154. https://doi.org/10.1007/978-3-662-01145-4_6

References

Hobbie, S.E., Chapin, F.S., 1996. Winter regulation of tundra litter carbon and nitrogen dynamics. Biogeochemistry 35, 327–338. https://doi.org/10.1007/BF02179958

Högström, E., Trofaier, A., Gouttevin, I., Bartsch, A., 2014. Assessing Seasonal Backscatter Variations with Respect to Uncertainties in Soil Moisture Retrieval in Siberian Tundra Regions. Remote Sens. 6, 8718–8738. https://doi.org/10.3390/rs6098718

Høye, T.T., Post, E., Schmidt, N.M., Trøjelsgaard, K., Forchhammer, M.C., 2013. Shorter flowering seasons and declining abundance of flower visitors in a warmer Arctic. Nat. Clim. Chang. 3, 759–763. https://doi.org/10.1038/nclimate1909

Ide, R., Oguma, H., 2013. A cost-effective monitoring method using digital time-lapse cameras for detecting temporal and spatial variations of snowmelt and vegetation phenology in alpine ecosystems. Ecol. Inform. 16, 25–34. https://doi.org/10.1016/j.ecoinf.2013.04.003

Iler, A.M., Inouye, D.W., Høye, T.T., Miller-Rushing, A.J., Burkle, L.A., Johnston, E.B., 2013. Maintenance of temporal synchrony between syrphid flies and floral resources despite differential phenological responses to climate. Glob. Chang. Biol. 19, 2348–2359. https://doi.org/10.1111/gcb.12246

Inouye, D.W., 2008. Effects of climate change on phenology, frost damage, and floral abundance of montane wildflowers. Ecology 89, 353–362. https://doi.org/10.1890/06-2128.1

Inouye, D.W., McGuire, A.D., 1991. Effects of snowpack on timing and abundance of flowering in Delphinium nelsonii (Ranunculaceae): implications for climate change. Am. J. Bot. 997–1001. https://doi.org/10.2307/2445179

IPCC, 2014b. Climate change 2014: synthesis report. Contribution of Working Groups I, II and III to the fifth assessment report of the Intergovernmental Panel on Climate Change. IPCC, Geneva, Switzerland.

IPCC, 2014a. Climate Change 2014–Impacts, Adaptation and Vulnerability: Regional Aspects. Cambridge University Press.

Irons, J.R., Dwyer, J.L., Barsi, J.A., 2012. The next Landsat satellite: The Landsat Data Continuity Mission. Remote Sens. Environ. 122, 11–21. https://doi.org/10.1016/J.RSE.2011.08.026

Johansson, M., Callaghan, T. V, Bosiö, J., Akerman, H.J., Jackowicz-Korczynski, M., Christensen, T.R., 2013. Rapid responses of permafrost and vegetation to experimentally increased snow cover in sub-arctic Sweden. Environ. Res. Lett. 8, 035025. https://doi.org/10.1088/1748-9326/8/3/035025

Jones, B.M., Grosse, G., Arp, C.D., Jones, M.C., Anthony, K.M.W., Romanovsky, V.E., 2011. Modern thermokarst lake dynamics in the continuous permafrost zone, northern Seward Peninsula, Alaska. J. Geophys. Res. 116. https://doi.org/Artn Goo103 Doi 10.1029/2011jg001666

Jones, B.M., Gusmeroli, A., Arp, C.D., Strozzi, T., 2013. Classification of freshwater ice conditions on the Alaskan Arctic Coastal Plain using ground penetrating radar and TerraSAR-X. Int. J. Remote Sens. 34, 8253–8265. https://doi.org/10.1080/2150704X.2013.834392

References

Kääb, A., 2008. Remote sensing of permafrost-related problems and hazards. Permafr. Periglac. Process. 19, 107–136. https://doi.org/doi.org/10.1002/ppp.619

Kanevskiy, M., Shur, Y., Strauss, J., Jorgenson, T., Fortier, D., Stephani, E., Vasiliev, A., 2016. Patterns and rates of riverbank erosion involving ice-rich permafrost (yedoma) in northern Alaska. Geomorphology 253, 370–384. https://doi.org/10.1016/j.geomorph.2015.10.023

Kennedy, C.E., Smith, C.A.S., Cooley, D.A., 2001. Observations of change in the cover of polargrass, Arctagrostis latifolia, and arctic lupine, Lupinus arcticus. Upl. Tundra Herschel Island, Yukon Territ. Canad. Field-Nat 115, 323–328.

Kępski, D., Luks, B., Migała, K., Wawrzyniak, T., Westermann, S., Wojtuń, B., 2017. Terrestrial Remote Sensing of Snowmelt in a Diverse High-Arctic Tundra Environment Using Time-Lapse Imagery. Remote Sens. 9, 733. https://doi.org/10.3390/rs9070733

Kokelj, S. V, Burn, C.R., 2005. Near-surface ground ice in sediments of the Mackenzie Delta, Northwest Territories, Canada. Permafr. Periglac. Process. 16, 291–303. https://doi.org/10.1002/ppp.537

Kokelj, S. V, Smith, C.A.S., Burn, C.R., 2002. Physical and chemical characteristics of the active layer and permafrost, Herschel Island, western Arctic Coast, Canada. Permafr. Periglac. Process. 13, 171–185. https://doi.org/10.1002/ppp.417

Kokelj, S. V, Tunnicliffe, J., Lacelle, D., Lantz, T.C., Chin, K.S., Fraser, R., 2015. Increased precipitation drives mega slump development and destabilization of ice-rich permafrost terrain, northwestern Canada (vol 129, pg 56, pg 2015). Glob. Planet. Change 135, 207. https://doi.org/10.1016/j.gloplacha.2015.10.014

Krab, E.J., Roennefarth, J., Becher, M., Blume-Werry, G., Keuper, F., Klaminder, J., Kreyling, J., Makoto, K., Milbau, A., Dorrepaal, E., 2017. Winter warming effects on tundra shrub performance are species-specific and dependent on spring conditions. J. Ecol. https://doi.org/10.1111/1365-2745.12872

Krieger, G., Moreira, A., Fiedler, H., Hajnsek, I., Werner, M., Younis, M., Zink, M., 2007. TanDEM-X: A satellite formation for high-resolution SAR interferometry. IEEE Trans. Geosci. Remote Sens. 45, 3317–3341.

Lafleur, P.M., Humphreys, E.R., 2018. Tundra shrub effects on growing season energy and carbon dioxide exchange. Environ. Res. Lett. 13, 055001. https://doi.org/10.1088/1748-9326/aab863

Lantuit, H., Atkinson, D., Overduin, P.P., Grigoriev, M., Rachold, V., Grosse, G., Hubberten, H.W., 2011. Coastal erosion dynamics on the permafrost-dominated Bykovsky Peninsula, north Siberia, 1951-2006. Polar Res. 30. https://doi.org/Artn 7341Doi 10.3402/Polar.V30i0.7341

Lantuit, H., Overduin, P.P., Couture, N., Wetterich, S., Aré, F., Atkinson, D., Brown, J., Cherkashov, G., Drozdov, D., Forbes, D.L., 2012a. The Arctic coastal dynamics database: a new classification scheme and statistics on Arctic permafrost coastlines. Estuaries and Coasts 35, 383–400. https://doi.org/10.1007/s12237-010-9362-6

Lantuit, H., Pollard, W.H., 2008. Fifty years of coastal erosion and retrogressive thaw slump activity on Herschel Island, southern Beaufort Sea, Yukon Territory, Canada.

Geomorphology 95, 84–102. https://doi.org/10.1016/j.geomorph.2006.07.040

Lantuit, H., Pollard, W.H., Couture, N., Fritz, M., Schirrmeister, L., Meyer, H., Hubberten, H., 2012. Modern and Late Holocene Retrogressive Thaw Slump Activity on the Yukon Coastal Plain and Herschel Island , Yukon Territory , Canada 51, 39–51. https://doi.org/10.1002/ppp.1731

Lantuit, H., Pollard, W.H., Couture, N., Fritz, M., Schirrmeister, L., Meyer, H., Hubberten, H.W., 2012b. Modern and Late Holocene Retrogressive Thaw Slump Activity on the Yukon Coastal Plain and Herschel Island, Yukon Territory, Canada. Permafr. Periglac. Process. 23, 39–51. https://doi.org/10.1002/ppp.1731

Lara, M.J., Nitze, I., Grosse, G., Martin, P., McGuire, A.D., 2018. Reduced arctic tundra productivity linked with landform and climate change interactions. Sci. Rep. 8, 2345. https://doi.org/10.1038/s41598-018-20692-8

Lawrence, D.M., Slater, A.G., Tomas, R.A., Holland, M.M., Deser, C., 2008. Accelerated Arctic land warming and permafrost degradation during rapid sea ice loss. Geophys. Res. Lett. 35. https://doi.org/10.1029/2008gl033985

Lee, J.-S., 1983. A simple speckle smoothing algorithm for synthetic aperture radar images. IEEE Trans. Syst. Man. Cybern. 85–89. https://doi.org/10.1109/TSMC.1983.6313036

Leinss, S., Parrella, G., Hajnsek, I., 2014. Snow height determination by polarimetric phase differences in X-Band SAR Data. IEEE J. Sel. Top. Appl. Earth Obs. Remote Sens. 7, 3794–3810. https://doi.org/10.1109/JSTARS.2014.2323199

Liljedahl, A.K., Boike, J., Daanen, R.P., Fedorov, A.N., Frost, G. V., Grosse, G., Hinzman, L.D., Iijma, Y., Jorgenson, J.C., Matveyeva, N., Necsoiu, M., Raynolds, M.K., Romanovsky, V.E., Schulla, J., Tape, K.D., Walker, D.A., Wilson, C.J., Yabuki, H., Zona, D., 2016. Pan-Arctic ice-wedge degradation in warming permafrost and its influence on tundra hydrology. Nat. Geosci. 9, 312–318. https://doi.org/10.1038/nge02674

Ling, F., Zhang, T., 2003. Impact of the timing and duration of seasonal snow cover on the active layer and permafrost in the Alaskan Arctic. Permafr. Periglac. Process. 14, 141–150. https://doi.org/10.1002/ppp.445

Liston, G.E., Liston, G.E., 2004. Representing Subgrid Snow Cover Heterogeneities in Regional and Global Models. J. Clim. 17, 1381–1397. https://doi.org/10.1175/1520-0442(2004)017<1381:RSSCHI>2.0.CO;2

Liu, L., Schaefer, K.M., Chen, A.C., Gusmeroli, A., Zebker, H.A., Zhang, T., 2015. Remote sensing measurements of thermokarst subsidence using InSAR. J. Geophys. Res. F Earth Surf. 120, 1935–1948. https://doi.org/10.1002/2015JF003599

Mätzler, C., 1994. Passive microwave signatures of landscapes in winter. Meteorol. Atmos. Phys. 54, 241–260.

Mätzler, C., Wegmüller, U., 1987. Dielectric properties of freshwater ice at microwave frequencies. J. Phys. D. Appl. Phys. 20, 1623–1630. https://doi.org/10.1088/0022-3727/20/12/013

Mekonnen, Z.A., Riley, W.J., Grant, R.F., 2018. Accelerated Nutrient Cycling and Increased Light Competition Will Lead to 21st Century Shrub Expansion in North American

Arctic Tundra. J. Geophys. Res. Biogeosciences 123, 1683–1701. https://doi.org/10.1029/2017JG004319

Mora, C., Jiménez, J.J., Pina, P., Catalão, J., Vieira, G., 2017. Evaluation of single-band snow-patch mapping using high-resolution microwave remote sensing: an application in the maritime Antarctic. Cryosph. 11, 139–155. https://doi.org/10.5194/tc-11-139-2017

Moreira, A., Prats-iraola, P., Younis, M., Krieger, G., Hajnsek, I., Papathanassiou, K.P., 2013. A Tutorial on Synthetic Aperture Radar. IEEE Geosci. Remote Sens. Mag. 6–43. https://doi.org/10.1109/MGRS.2013.2248301

Morgenstern, A., 2012. Thermokarst and thermal erosion: Degradation of Siberian ice-rich permafrost. Institutional Repository of the University of Potsdam.

Morgenstern, A., Grosse, G., Arcos, D.R., Günther, F., Overduin, P.P., Schirrmeister, L., 2014. The role of thermal erosion on the degradation of Siberian ice-rich permafrost. J. Geophys. Res.

Morgenstern, A., Grosse, G., Günther, F., Fedorova, I., Schirrmeister, L., 2011a. Spatial analyses of thermokarst lakes and basins in Yedoma landscapes of the Lena Delta. Cryosphere 5, 849–867. https://doi.org/10.5194/tc-5-849-2011

Morgenstern, A., Röhr, C., Grosse, G., Grigoriev, M.N., 2011b. The Lena River Delta - inventory of lakes and geomorphological terraces. https://doi.org/10.1594/PANGAEA.758728

Morgenstern, A., Ulrich, M., Günther, F., Roessler, S., Fedorova, I. V., Rudaya, N.A., Wetterich, S., Boike, J., Schirrmeister, L., 2013. Evolution of thermokarst in East Siberian ice-rich permafrost: A case study. Geomorphology 201, 363–379. https://doi.org/10.1016/j.geomorph.2013.07.011

Morgenstern, A., Ulrich, M., Günther, F., Roessler, S., Fedorova, I. V, Rudaya, N.A., Wetterich, S., Boike, J., Schirrmeister, L., 2013. Evolution of thermokarst in East Siberian ice-rich permafrost: A case study. Geomorphology 201, 363–379. https://doi.org/DOI 10.1016/j.geomorph.2013.07.011

Myers-Smith, I., n.d. Eighteen years of ecological monitoring reveals multiple lines of evidence for tundra vegetation change. Ecol. Monogr. ECM18-0017.

Myers-Smith, I.H., Forbes, B.C., Wilmking, M., Hallinger, M., Lantz, T., Blok, D., Tape, K.D., Macias-Fauria, M., Sass-Klaassen, U., Lévesque, E., Boudreau, S., Ropars, P., Hermanutz, L., Trant, A., Collier, L.S., Weijers, S., Rozema, J., Rayback, S.A., Schmidt, N.M., Schaepman-Strub, G., Wipf, S., Rixen, C., Ménard, C.B., Venn, S., Goetz, S., Andreu-Hayles, L., Elmendorf, S., Ravolainen, V., Welker, J., Grogan, P., Epstein, H.E., Hik, D.S., 2011. Shrub expansion in tundra ecosystems: dynamics, impacts and research priorities. Environ. Res. Lett. 6, 045509. https://doi.org/10.1088/1748-9326/6/4/045509

Myers-smith, I.H., Hik, D.S., Kennedy, C., Cooley, D., Johnstone, J.F., Kenney, A.J., Krebs, C.J., 2011. Expansion of Canopy-Forming Willows Over the Twentieth Century on Herschel Island , Yukon Territory , Canada. AMBIO A J. Hum. Environ. 40, 610–623. https://doi.org/10.1007/s13280-011-0168-y

Nagler, T., 1996. Methods and analysis of synthetic aperture radar data for ERS-1 and X-SAR for snow and glacier applications. University of Innsbruck.

References

Nagler, T., Rott, H., 2000. Retrieval of wet snow by means of multitemporal SAR data. IEEE Trans. Geosci. Remote Sens. 38, 754–765. https://doi.org/10.1109/36.842004

Nagler, T., Rott, H., Ripper, E., Bippus, G., Hetzenecker, M., 2016. Advancements for Snowmelt Monitoring by Means of Sentinel-1 SAR. Remote Sens. 8, 348. https://doi.org/10.3390/rs8040348

Nijland, W., Coops, N.C., Coogan, S.C.P., Bater, C.W., Wulder, M.A., Nielsen, S.E., McDermid, G., Stenhouse, G.B., 2013. Vegetation phenology can be captured with digital repeat photography and linked to variability of root nutrition in Hedysarum alpinum. Appl. Veg. Sci. 16, 317–324. https://doi.org/10.1111/avsc.12000

Nijland, W., De Jong, R., De Jong, S.M., Wulder, M.A., Bater, C.W., Coops, N.C., 2014. Monitoring plant condition and phenology using infrared sensitive consumer grade digital cameras. Agric. For. Meteorol. 184, 98–106. https://doi.org/10.1016/j.agrformet.2013.09.007

Nitze, I., Grosse, G., 2016. Detection of landscape dynamics in the Arctic Lena Delta with temporally dense Landsat time-series stacks. Remote Sens. Environ. 181, 27–41. https://doi.org/10.1016/j.rse.2016.03.038

Notti, D., Davalillo, J.C., Herrera, G., Mora, O., Ferrata, V., 2010. Assessment of the performance of X-band satellite radar data for landslide mapping and monitoring: Upper Tena Valley case study. Nat. Hazards Earth Syst. Sci. 10, 1865–1875. https://doi.org/10.5194/nhess-10-1865-2010

Obu, J., Lantuit, H., Grosse, G., Günther, F., Sachs, T., Helm, V., Fritz, M., 2017. Coastal erosion and mass wasting along the Canadian Beaufort Sea based on annual airborne LiDAR elevation data. Geomorphology 293, 331–346. https://doi.org/10.1016/J.GEOMORPH.2016.02.014

Obu, J., Lantuit, H., Myers-Smith, I., Heim, B., Wolter, J., Fritz, M., 2015. Effect of Terrain Characteristics on Soil Organic Carbon and Total Nitrogen Stocks in Soils of Herschel Island, Western Canadian Arctic. Permafr. Periglac. Process. n/a-n/a. https://doi.org/10.1002/ppp.1881

Obu, J., Lantuit, H., Myers-Smith, I.H., Heim, B., Wolter, J., Fritz, M., 2016. Ecological classification of Herschel Island based on supervised classification of multispectral satellite imagery. Suppl. to Obu, J al. Eff. Terrain Charact. Soil Org. Carbon Total Nitrogen Stock. Soils Herschel Island, West. Can. Arctic. Permafr. Periglac. Process. 28(1), 92-107, https//doi.org/10.1002/ppp. https://doi.org/10.1594/PANGAEA.858786

Ostendorf, B., Quinn, P., Beven, K., Tenhunen, J.D., 1996. Hydrological Controls on Ecosystem Gas Exchange in an Arctic Landscape. Springer, Berlin, Heidelberg, pp. 369–386. https://doi.org/10.1007/978-3-662-01145-4_17

Paradis, M., Lévesque, E., Boudreau, S., 2016. Greater effect of increasing shrub height on winter versus summer soil temperature. Environ. Res. Lett. 11, 085005. https://doi.org/10.1088/1748-9326/11/8/085005

Park, H., Kim, Y., Kimball, J.S., 2016. Remote Sensing of Environment Widespread permafrost vulnerability and soil active layer increases over the high northern latitudes inferred from satellite remote sensing and process model assessments. Remote Sens. Environ. 175, 349–358. https://doi.org/10.1016/j.rse.2015.12.046

References

Payne, C., Panda, S., Prakash, A., 2018. Remote Sensing of River Erosion on the Colville River, North Slope Alaska. Remote Sens. 10, 397. https://doi.org/10.3390/rs10030397

Perko, R., Raggam, H., Deutscher, J., Gutjahr, K., Schardt, M., 2011. Forest Assessment Using High Resolution SAR Data in X-Band. Remote Sens. 3, 792–815. https://doi.org/10.3390/rs3040792

Peterson, B.J., Holmes, R.M., McClelland, J.W., Vörösmarty, C.J., Lammers, R.B., Shiklomanov, A.I., Shiklomanov, I. a, Rahmstorf, S., 2002. Increasing river discharge to the Arctic Ocean. Science 298, 2171–2173. https://doi.org/10.1126/science.1077445

Pohl, S., Marsh, P., 2006. Modelling the spatial-temporary variability of spring snowmelt in an arctic catchment. Hydrol. Process. 20, 1773–1792. https://doi.org/10.1002/hyp.5955

PSTG, 2017. Polar Space Task Group (PSTG) Seventh Session. Final Report. Innsbruck, Austria.

R Core Team, 2016. R: A language and environment for statistical computing.

Radosavljevic, B., Lantuit, H., Pollard, W., Overduin, P., Couture, N., Sachs, T., Helm, V., Fritz, M., 2015. Erosion and Flooding - Threats to Coastal Infrastructure in the Arctic: A Case Study from Herschel Island, Yukon Territory, Canada. Estuaries and Coasts. https://doi.org/10.1007/s12237-015-0046-0

Ramage, J., L., Fortier, D., Hugelius, G., Lantuit, H., Morgenstern, A., n.d. Dissecting valleys: Snapshot of carbon and nitrogen distribution in Arctic valleys. Catena.

Ramage, J.L., 2017. Valleys of Herschel Island, Yukon, Canada. https://doi.org/10.1594/PANGAEA.883524

Ramage, J.L., Irrgang, A.M., Herzschuh, U., Morgenstern, A., Couture, N., Lantuit, H., 2017. Terrain controls on the occurrence of coastal retrogressive thaw slumps along the Yukon Coast, Canada. J. Geophys. Res. Earth Surf. 1619–1634. https://doi.org/10.1002/2017JF004231

Rampton, V.N., 1982. Quaternary geology of the Yukon Coastal Plain. Geol. Surv. Canada, Bull. 49. https://doi.org/10.4095/111347

Reber, B., Mätzler, C., Schanda, E., 1987. Microwave signatures of snow crusts modelling and measurements. Int. J. Remote Sens. 8, 1649–1665. https://doi.org/10.1080/01431168708954805

Richardson, A.D., Jenkins, J.P., Braswell, B.H., Hollinger, D.Y., Ollinger, S. V, Smith, M.-L., 2007. Use of digital webcam images to track spring green-up in a deciduous broadleaf forest. Oecologia 152, 323–334. https://doi.org/10.1007/s00442-006-0657-z

Richardson, A.D., Keenan, T.F., Migliavacca, M., Ryu, Y., Sonnentag, O., Toomey, M., 2013. Climate change, phenology, and phenological control of vegetation feedbacks to the climate system. Agric. For. Meteorol. 169, 156–173. https://doi.org/10.1016/J.AGRFORMET.2012.09.012

Rignot, E.J.M., Zyl, J.J. Van, 1993. Change Detection Techniques for ERS-1 SAR Data. IEEE Trans. Geosci. Remote Sens. 31, 896–906. https://doi.org/10.1109/36.239913

Rizzoli, P., Martone, M., Rott, H., Moreira, A., 2017. Characterization of Snow Facies on the

Greenland Ice Sheet Observed by TanDEM-X Interferometric SAR Data 1–24. https://doi.org/10.3390/rs9040315

Romanov, P., Gutman, G., Csiszar, I., Romanov, P., Gutman, G., Csiszar, I., 2000. Automated Monitoring of Snow Cover over North America with Multispectral Satellite Data. J. Appl. Meteorol. 39, 1866–1880. https://doi.org/10.1175/1520-0450(2000)039<1866:AMOSCO>2.0.CO;2

Romanovskii, N.N., Hubberten, H.W., Gavrilov, A. V, Tumskoy, V.E., Kholodov, A.L., 2004. Permafrost of the east Siberian Arctic shelf and coastal lowlands. Quat. Sci. Rev. 11, 1359–1369. https://doi.org/10.1016/j.quascirev.2003.12.014

Romanovsky, V.E., Smith, S.L., Christiansen, H.H., 2010. Permafrost Thermal State in the Polar Northern Hemisphere during the International Polar Year 2007-2009: a Synthesis. Permafr. Periglac. Process. 21, 106–116. https://doi.org/10.1002/ppp.689

Roth, A., Eineder, M., Schättler, B., Remote, G., Data, S., Achimrothdlrde, G., Sensing, R., Eineder, G.M., De, B.S., Vi, C., Vi, W.G., 2002. TerraSAR-X: A new persepctive for applications requiring high resolution spaceborne SAR data, in: Proceedings of the Joint ISPRS 6. pp. 1–4.

Rott, H., Heidinger, M., Nagler, T., Cline, D., Yueh, S., 2009. Retrieval of snow parameters from Ku-band and X-band radar backscatter measurements, in: IEEE International Geoscience and Remote Sensing Symposium. IEEE, p. II-144-II-147. https://doi.org/10.1109/IGARSS.2009.5418024

Rott, H., Nagler, T., 1993. Snow and glacier investigations by ERS-1 SAR: First results, in: Proceedings of the 1st ERS-1 Symposium: Space at the Service of Our Environment. pp. 577–582.

Salomonson, V.., Appel, I., 2004. Estimating fractional snow cover from MODIS using the normalized difference snow index. Remote Sens. Environ. 89, 351–360. https://doi.org/10.1016/J.RSE.2003.10.016

Schellenberger, T., Ventura, B., Notarnicola, C., Zebisch, M., Nagler, T., Rott, H., 2011. Exploitation of Cosmo-Skymed image time series for snow monitoring in alpine regions. Int. Geosci. Remote Sens. Symp. 3641–3644. https://doi.org/10.1109/IGARSS.2011.6050013

Schellenberger, T., Ventura, B., Zebisch, M., Notarnicola, C., 2012. Wet Snow Cover Mapping Algorithm Based on Multitemporal COSMO-SkyMed X-Band SAR Images. IEEE J. Sel. Top. Appl. Earth Obs. Remote Sens. 5, 1045–1053. https://doi.org/10.1109/JSTARS.2012.2190720

Schimel, J.P., Bilbrough, C., Welker, J.A., Schimel, J.P., Bilbrough, C., Welker, J.M., 2004. Increased snow depth affects microbial activity and nitrogen mineralization in two Arctic tundra communities. Schimel, Joshua P., Carol Bilbrough, Jeffery M. Welker. “Increased snow depth Affect. Microb. Act. nitrogen Miner. two Arct. tundra communities.” Soil Biol. Biochem. 36, 217–227.

Schimel, J.P., Kielland, K., Chapin, F.S., 1996. Nutrient Availability and Uptake by Tundra Plants. Springer, Berlin, Heidelberg, pp. 203–221. https://doi.org/10.1007/978-3-662-01145-4_10

Schirrmeister, L., Grigoriev, M.N., 2004. Russian-German Cooperation System Laptev Sea:

The Expedition Lena Anabar 2003, Periglacial Studies around Cape Mamontov Klyk, in: Schirrmeister, L. (Ed.), Expeditions in Siberia 2003. Alfred Wegener Institute for Polar and Marine Research, pp. 61–209.

Schirrmeister, L., Grosse, G., Schwamborn, G., Andreev, a a, Meyer, H., Kunitsky, V. V, Kuznetsova, T. V, Dorozhkina, M. V, Pavlova, E.Y., Bobrov, a a, Oezen, D., 2003. Late Quaternary History of the Accumulation Plain North of the Chekanovsky Ridge (Lena Delta, Russia): A Multidisciplinary Approach. Polar Geogr. 27, 277–319. https://doi.org/10.1080/789610225

Schirrmeister, L., Kunitsky, V., Grosse, G., Wetterich, S., Meyer, H., Schwamborn, G., Babiy, O., Derevyagin, A., Siegert, C., 2011. Sedimentary characteristics and origin of the Late Pleistocene Ice Complex on north-east Siberian Arctic coastal lowlands and islands – A review. Quat. Int. 241, 3–25. https://doi.org/http://dx.doi.org/10.1016/j.quaint.2010.04.004

Schneider, J., Grosse, G., Wagner, D., 2009. Land cover classification of tundra environments in the Arctic Lena Delta based on Landsat 7 ETM+ data and its application for upscaling of methane emissions. Remote Sens. Environ. 113, 380–391. https://doi.org/DOI 10.1016/j.rse.2008.10.013

Schuur, E.A.G., McGuire, A.D., Schadel, C., Grosse, G., Harden, J.W., Hayes, D.J., Hugelius, G., Koven, C.D., Kuhry, P., Lawrence, D.M., Natali, S.M., Olefeldt, D., Romanovsky, V.E., Schaefer, K., Turetsky, M.R., Treat, C.C., Vonk, J.E., 2015. Climate change and the permafrost carbon feedback. Nature 520, 171–179. https://doi.org/10.1038/nature14338

Schwartz, M.D., Ahas, R., Aasa, A., 2006. Onset of spring starting earlier across the Northern Hemisphere. Glob. Chang. Biol. 12, 343–351. https://doi.org/10.1111/j.1365-2486.2005.01097.x

Scott, K.M., 1978. Effects of permafrost on stream channel behavior in Arctic Alaska. U.S. Geol. Surv. Prof. Pap. 1068 1–19.

Semenchuk, P.R., Elberling, B., Cecilie, @bullet, @bullet, A., Winkler, J., Rumpf, S., Michelsen, A., Cooper, E.J., Semenchuk, P.R., Rumpf, Á.S., Cooper, Á.E.J., Amtorp, Á.C., Winkler, Á.J., Elberling, Á.B., Michelsen, Á.A., Rumpf, S., Michelsen, A., 2015. Deeper snow alters soil nutrient availability and leaf nutrient status in high Arctic tundra. Biogeochemistry 124, 81–94. https://doi.org/10.1007/s10533-015-0082-7

Sessa, R., Dolman, H., 2008. Terrestrial essential climate variables for climate change assessment, mitigation and adaptation (GTOS 52). FAO, Rome, Italy.

Shi, X., Zhang, L., Tang, M., Li, M., Liao, M., 2017. Investigating a reservoir bank slope displacement history with multi-frequency satellite SAR data. Landslides 14, 1961–1973. https://doi.org/10.1007/s10346-017-0846-3

Short, N., Brisco, B., Couture, N., Pollard, W., Murnaghan, K., Budkewitsch, P., 2011. A comparison of TerraSAR-X, RADARSAT-2 and ALOS-PALSAR interferometry for monitoring permafrost environments, case study from Herschel Island, Canada. Remote Sens. Environ. 115, 3491–3506. https://doi.org/10.1016/j.rse.2011.08.012

Shur, Y., Vasiliev, A., Kanevsky, M., Maximov, V., Pokrovsky, S., Zaikanov, V., 2002. Shore Erosion in Russian Arctic. Cold Reg. Eng. Cold Reg. Impacts Transp. Infrastruct.

https://doi.org/doi:10.1061/40621(254)63

Shur, Y.L., 1988. The Upper Horizon of Permafrost and Thermokarst, in: Proceedings of Fifth International Conference on Permafrost. TAPIR Publishers, Trodenheim, pp. 876–871.

Smith, C.A.S., Kennedy, C.E., Hargrave, A.E., McKenna, K.M., 1989. Soil and vegetation of Herschel Island, Yukon territory. Yukon Soil Surv. Rep. 1.

Solomon, S.M., 2005. Spatial and temporal variability of shoreline change in the Beaufort-Mackenzie region, northwest territories, Canada. Geo-Marine Lett. 25, 127–137. https://doi.org/10.1007/s00367-004-0194-x

Stettner, S., 2014. Characterizing thermo-erosional landforms in Siberian ice-rich permafrost. Morphometric investigations in the Lena Delta using high-resolution satellite imagery and digital elevation models. Inst. Geogr. Sci. Freie Universität Berlin, Berlin.

Stettner, S., Beamish, A.L., Bartsch, A., Heim, B., Grosse, G., Roth, A., Lantuit, H., 2017. Monitoring inter- and intra-seasonal dynamics of rapidly degrading ice-rich permafrost riverbanks in the Lena Delta with TerraSAR-X time series. Remote Sens. 10. https://doi.org/10.3390/rs10010051

Stettner, S., Lantuit, H., Heim, B., Eppler, J., Roth, A., Bartsch, A., Rabus, B., n.d. TerraSAR-X time series fill a gap in spaceborne snowmelt monitoring of small Arctic catchments. Remote Sens.

Stiles, W.H., Ulaby, F.T., 1980. The active and passive microwave response to snow parameters: 1. Wetness. J. Geophys. Res. 85, 1037. https://doi.org/10.1029/JC085iC02p01037

Stow, D.A., Hope, A., McGuire, D., Verbyla, D., Gamon, J., Huemmrich, F., Houston, S., Racine, C., Sturm, M., Tape, K., Hinzman, L., Yoshikawa, K., Tweedie, C., Noyle, B., Silapaswan, C., Douglas, D., Griffith, B., Jia, G., Epstein, H., Walker, D., Daeschner, S., Petersen, A., Zhou, L., Myneni, R., 2004. Remote sensing of vegetation and land-cover change in Arctic Tundra Ecosystems. Remote Sens. Environ. 89, 281–308. https://doi.org/10.1016/J.RSE.2003.10.018

Strauss, J., Schirrmeister, L., Grosse, G., Fortier, D., Hugelius, G., Knoblauch, C., Romanovsky, V., Schädel, C., von Deimling, T.S., Schuur, E.A.G., 2017. Deep Yedoma permafrost: A synthesis of depositional characteristics and carbon vulnerability. Earth-Science Rev. 172, 75–86. https://doi.org/10.1016/j.earscirev.2017.07.007

Strozzi, T., Delaloye, R., Kääb, A., Ambrosi, C., Perruchoud, E., 2010. Combined observations of rock mass movements using satellite SAR interferometry , differential GPS , airborne digital photogrammetry , and airborne photography interpretation 115, 1–11. https://doi.org/10.1029/2009JF001311

Strozzi, T., Wegmuller, U., Matzler, C., 1999. Mapping wet snowcovers with SAR interferometry. Int. J. Remote Sens. 20, 2395–2403. https://doi.org/10.1080/014311699212083

Sturm, M., Holmgren, J., McFadden, J.P., Liston, G.E., Chapin, F.S., Racine, C.H., Sturm, M., Holmgren, J., McFadden, J.P., Liston, G.E., III, F.S.C., Racine, C.H., 2001. Snow–Shrub Interactions in Arctic Tundra: A Hypothesis with Climatic Implications. J.

Clim. 14, 336–344. https://doi.org/10.1175/1520-0442(2001)014<0336:SSIIAT>2.0.CO;2

Tananaev, N.I., 2016. Geomorphology Hydrological and sedimentary controls over fl uvial thermal erosion , the Lena River , central Yakutia. Geomorphology 253, 524–533. https://doi.org/10.1016/j.geomorph.2015.11.009

Thieler, E.R., Himmelstoss, E.A., Zichichi, J.L., Ergul, A., 2009. Digital Shoreline Analysis System (DSAS) version 4.0— An ArcGIS extension for calculating shoreline change: U.S. Geological Survey Open-File Report 2008-1278.

Ulaby, F.T., Allen, C.T., Eger, G., Kanemasu, E., 1984. Relating the microwave backscattering coefficient to leaf area index. Remote Sens. Environ. 14, 113–133. https://doi.org/10.1016/0034-4257(84)90010-5

Ulaby, F.T., Aslam, A., Dobson, M.C., 1982. Effects of vegetation cover on the radar sensitivity to soil moisture. IEEE Trans. Geosci. Remote Sens. 20, 476–481. https://doi.org/10.1109/TGRS.1982.350413

Ulaby, F.T., Long, D.G., Blackwell, W.J., Elachi, C., Fung, A.K., Ruf, C., Sarabandi, K., Zebker, H.A., Van Zyl, J., 2014. Microwave radar and radiometric remote sensing. University of Michigan Press Ann Arbor.

Ulaby, F.T., Moore, R.K., Fung, A.K., 1986. Microwave Remote Sensing: Active and Passive. Volume Scattering and Emission Theory, Advanced Systems and Applications. Dedham, MA Artech House.

Ulaby, F.T., Stiles, W.H., 1980. The active and passive microwave response to snow parameters: 2. Water equivalent of dry snow. J. Geophys. Res. 85, 1045. https://doi.org/10.1029/JC085iC02p01045

Ullmann, T., Banks, S.N., Schmitt, A., Jagdhuber, T., 2017. Scattering characteristics of X-, C-and L-Band polsar data examined for the tundra environment of the Tuktoyaktuk Peninsula, Canada. Appl. Sci. 7, 595. https://doi.org/10.3390/app7060595

Ullmann, T., Schmitt, A., Jagdhuber, T., 2016. Two Component Decomposition of Dual Polarimetric HH / VV SAR Data: Case Study for the Tundra Environment of the Mackenzie Delta Region , Canada 1–24. https://doi.org/10.3390/rs8121027

Ullmann, T., Schmitt, A., Roth, A., Duffe, J., Dech, S., Hubberten, H.-W., Baumhauer, R., 2014. Land Cover Characterization and Classification of Arctic Tundra Environments by means of polarized Synthetic Aperture X- and C-Band Radar (PolSAR) and Landsat 8 Multispectral Imagery - Richards Island, Canada. Remote Sens. 6, 1–26. https://doi.org/10.3390/rs60x000x

van Everdingen, R., 2005. Multi-language glossary of permafrost and related ground-ice terms. National Snow and Ice Data Center/World Data Center for Glaciology, Boulder, CO.

Vaughan, D.G., Comiso, J.C., Allison, I., Carrasco, J., Kaser, G., Kwok, R., Mote, P., Murray, T., Paul, F., Ren, J., 2013. Observations of the cryosphere, in: Climate Change 2013: The Physical Bases. pp. 317–382.

Vonk, J.E., Mann, P.J., Davydov, S., Davydova, A., Spencer, R.G.M., Schade, J., Sobczak, W. V, Zimov, N., Zimov, S., Bulygina, E., Eglinton, T.I., Holmes, R.M., 2013. High biolability of ancient permafrost carbon upon thaw. Geophys. Res. Lett. 40, 2689–

2693. https://doi.org/10.1002/grl.50348

Walker, H.J., 1998. Arctic Deltas. J. Coast. Res. 14, 718–738.

Walker, J., Lennart, A., Peippo, J., 1987. Riverbank erosion in the Colville delta, Alaska. Geogr. Ann. 69 A, 61–70. https://doi.org/10.1080/04353676.1987.11880197

Washburn, A.L., 1979. Geocryology: A Survey of Periglacial Processes and Environments. E. Arnold.

Wegmuller, U., Werner, C., 1997. Retrieval of vegetation parameters with SAR interferometry. IEEE Trans. Geosci. Remote Sens. 35, 18–24. https://doi.org/10.1109/36.551930

Weller, G., Symon, C., Arris, L., Hill, B., 2005. Summary and synthesis of the ACIA, in: Arctic Climate Impact Assessment. Campbridge University Press, New York, NY, pp. 990–1020.

Wendleder, A., Heilig, A., Schmitt, A., Mayer, C., 2015. Monitoring of Wet Snow and Accumulations At High Alpine Glaciers Using Radar Technologies. ISPRS - Int. Arch. Photogramm. Remote Sens. Spat. Inf. Sci. XL-7/W3, 1063–1068. https://doi.org/10.5194/isprsarchives-XL-7-W3-1063-2015

Wetterich, S., Kuzmina, S., Andreev, A.A., Kienast, F., Meyer, H., Schirrmeister, L., Kuznetsova, T., Sierralta, M., 2008. Palaeoenvironmental dynamics inferred from late Quaternary permafrost deposits on Kurungnakh Island, Lena Delta, Northeast Siberia, Russia. Quat. Sci. Rev. 27, 1523–1540. https://doi.org/DOI 10.1016/j.quascirev.2008.04.007

Wheeler, H.C., Høye, T.T., Schmidt, N.M., Svenning, J.-C., Forchhammer, M.C., 2015. Phenological mismatch with abiotic conditions—implications for flowering in Arctic plants. Ecology 96, 775–787.

White, L., Brisco, B., Dabboor, M., Schmitt, A., Pratt, A., 2015. A Collection of SAR Methodologies for Monitoring Wetlands. https://doi.org/10.3390/rs70607615

Widhalm, B., Bartsch, A., Heim, B., 2015. A novel approach for the characterization of tundra wetland regions with C-band SAR satellite data. Int. J. Remote Sens. 36, 5537–5556. https://doi.org/10.1080/01431161.2015.1101505

Widhalm, B., Bartsch, A., Leibman, M., Khomutov, A., 2017. Active-layer thickness estimation from X-band SAR backscatter intensity 483–496. https://doi.org/10.5194/tc-11-483-2017

Wipf, S., Stoeckli, V., Bebi, P., 2009. Winter climate change in alpine tundra: plant responses to changes in snow depth and snowmelt timing. Clim. Change 94, 105–121. https://doi.org/10.1007/s10584-009-9546-x

Woo, M., 1976. Hydrology of a small Canadian High Arctic basin during the snowmelt period. CATENA 3, 155–168. https://doi.org/10.1016/0341-8162(76)90007-2

Woo, M.K., Marsh, P., 2005. Snow, frozen soils and permafrost hydrology in Canada, 1999-2002. Hydrol. Process. 19, 215–229. https://doi.org/10.1002/hyp.5772

Woo, M.K., Marsh, P., Pomeroy, J.W., 2000. Snow, frozen soils and permafrost hydrology

in Canada, 1995-1998. Hydrol. Process. 14, 1591–1611. https://doi.org/Doi 10.1002/1099-1085(20000630)14:9<1591::Aid-Hyp78>3.0.Co;2-W

Yu, Z., Loisel, J., Brosseau, D.P., Beilman, D.W., Hunt, S.J., 2010. Global peatland dynamics since the Last Glacial Maximum. Geophys. Res. Lett. 37. https://doi.org/10.1029/2010GL043584

Zebker, H.A., Villasenor, J., 1992. Decorrelation in interferometric radar echoes. IEEE Trans. Geosci. Remote Sens. 30, 950–959. https://doi.org/10.1109/36.175330

Zeng, H., Jia, G., Epstein, H., 2011. Recent changes in phenology over the northern high latitudes detected from multi-satellite data. Environ. Res. Lett. 6, 45508. https://doi.org/10.1088/1748-9326/6/4/045508

Zhang, T., 2005. Influence of the seasonal snow cover on the ground thermal regime: An overview. Rev. Geophys. 43, n/a-n/a. https://doi.org/10.1029/2004RG000157

Zhang, T., Osterkamp, T.E., Stamnes, K., 1996. Influence of the depth hoar layer of the seasonal snow cover on the ground thermal regime. WATER Resour. Res. 32, 2075–2086. https://doi.org/10.1029/96WR00996

Zhang, T., Stamnes, K., 1998. Impact of climatic factors on the active layer and permafrost at Barrow, Alaska. Permafr. Periglac. Process. 9, 229–246. https://doi.org/10.1002/(SICI)1099-1530(199807/09)9:3<229::AID-PPP286>3.0.CO;2-T

Zink, M., Bartusch, M., Ulrich, D., 2012. TanDEM-X mission status, in: Synthetic Aperture Radar, 2012. EUSAR. 9th European Conference On. VDE, pp. 85–88.

Zwieback, S., Bartsch, A., Boike, J., Grosse, G., Günther, F., Heim, B., Morgenstern, A., Hajnsek, I., 2016. Monitoring permafrost and thermokarst processes with TanDEM-X DEM time series: Opportunities and limitations, in: Geoscience and Remote Sensing Symposium (IGARSS), 2016 IEEE International. IEEE, pp. 332–335.

Zwieback, S., Kokelj, S. V, Günther, F., Boike, J., Grosse, G., Hajnsek, I., 2017. Sub-seasonal thaw slump mass wasting is not consistently energy limited at the landscape scale 1–24. https://doi.org/10.5194/tc-2017-141

ACKNOWLEDGEMENTS

An Erster Stelle möchte ich mich bei dem Betreuerteam dieser Arbeit bedanken ohne die diese Arbeit nicht möglich gewesen wäre. Danke an Erstbetreuer Hugues Lantuit für die großartige Unterstützung in allen Bereichen in den vergangenen Jahren. Ich bedanke mich ebenso besonders bei Annett Bartsch, Zweitbetreuerin dieser Arbeit, welche immer mit schnellem und wertvollem Rat zur Seite stand. Bei meiner langjährigen Mentorin Birgit Heim möchte ich mich insbesondere sehr bedanken für ihren großen Einsatz und dass Sie mir die Möglichkeiten gegeben hat diese Arbeit zu schreiben und alle Erfahrungen die damit verbunden sind! Danke auch an Guido Grosse für seine Unterstützung und Ideen in meinem PhD Komitee. Ich möchte auch ganz besonders den Gutachtern dieser Arbeit danken, dass sie diese Aufgabe übernommen haben!

Ich danke sehr herzlich Annett Bartsch, Barbara Widhalm und Elin Högström für Ihre Unterstützung bei meinem Aufenthalt an der TU Wien im Februar 2015. Ich danke ebenso herzlich Achim Roth, Andreas Schmitt und Anna Wendleder vom DLR, Bereich Landoberflächen für Ihre Unterstützung bei meinem Gastaufenthalt am DLR im Februar 2015. Ich danke sehr herzlich Irena Hajinsek und im Speziellen Simon Zwieback, von der ETH Zürich für Ihre Unterstützung bei meinem dreiwöchigen Aufenthalt im April 2016. Achim Roth möchte ich gesondert einen großen Dank aussprechen für die einzigartige Unterstützung bei der TSX Missions Planung ohne die diese Arbeit so nicht möglich gewesen wäre!

Ich möchte all meinen Kollegen am AWI danken die ich kennen gelernt und von denen ich viel gelernt habe. Allen voran danke ich der „Familie Bornemann“, bestehend aus Anne Morgenstern, Sonya Antonova, Niko Bornemann, Antje Eulenburg, Sascha Niemann für unsere konspirativen Treffen und dass wir immer noch von unserem gemeinsamen Sommer in Sibirien zehren. Ich danke allen Kollegen in der ehemaligen COPER Arbeitsgruppe für eine so angenehme Arbeitsumgebung, insbesondere Boris Radosavljevic, Hugues Lantuit, George Tanski, Anna Irrgang, Justine Ramage, Michael Fritz, Steffi Wegener, Konstantin Klein, Justus Gimsa, Isabell Eischeid, Jaroslav Obu, Caroline Coch, Julian Schneider, Juliane Wolter und viele mehr.

Acknowledgements

I want to thank all the people I met during my 5-month research stay at the SARlab and the IRSS in Vancouver, Canada, in particular my mentors Bernhard Rabus and Nicholas Coops, thank you for the support and having me in your amazing working groups!

Ich möchte POGS, POLMAR und GEO.X für die finanzielle Unterstützung danken, die mir ermöglicht hat an den Konferenzen ArcticChange 2015 und 2017 teilzunehmen. Bei Guido Grosse und POLMAR möchte ich mich besonders bedanken für die Unterstützung für mein Vorhaben 5 Monate an der Simon Fraser University in Vancouver zu sein.

I want to thank all the great people I had the chance to meet during the three expeditions during my PhD to the Siberian and Canadian Arctic. In particular I want to thank the Rangers of Qikiqtaruk, in particular Edward McLeod, Samuel McLeod, Ricky Joe and Paydon Lennie as well as Chief Ranger Richard Gordon for their great support during the field work on Herschel Island! I also want to thank all staff of the Samoylov research station for their logistical support. Thank you Team Shrub for all the fun time on Herschel and the ArcticNet Conferences.

Ich danke allen meinen Freunden und neuen Freunden in Vancouver und Squamish für so viele gute Momente und die nötige Ablenkung und Unterstützung. Ich danke meiner Familie von tiefem Herzen für ihre bedingungslose Unterstützung zu jeder Zeit.

Von tiefstem Herzen bedanke ich mich bei den Bewohnern des „Schloss Skali“, George Tanski und Alison Beamish, unsere gemeinsamen Radtouren, exzessiven Schwimm Exkursionen und gemeinsamen Reisen bedeuten mir sehr viel und haben mir immer die nötige Ablenkung gegeben damit ich fast immer frisch erholt wieder den Telegrafenberg erklimmen konnte!

Ali, für deine grenzenlose Unterstützung bin ich dir zutiefst dankbar! Das wir noch nicht zusammengewachsen ist mir ein Rätsel. Ich freue mich so sehr auf alles was noch kommt!!

EIDESSTATTLICHE ERKLÄRUNG

Hiermit versichere ich, dass ich die vorliegende Arbeit selbstständig verfasst und keine anderen als die angegebenen Quellen und Hilfsmittel verwendet habe.

Ich habe diese kumulative Dissertation am Alfred-Wegener-Institut Helmholtz Zentrum für Polar und Meeresforschung in Potsdam erarbeitet und in englischer Sprache angefertigt. Diese Dissertation wird erstmalig und ausschließlich an der Universität Potsdam eingereicht.

Die dem Promotionsverfahren zugrundeliegende Promotionsordnung vom 01.04.2015 ist mir bekannt.

Potsdam, den 25.06.2018, Samuel Stettner